UNIVERSITÉ DE MONTRÉAL

STUDY OF THE HEMODYNAMIC RESPONSE TO INTERICTAL EPILEPTIFORM DISCHARGES IN HUMAN EPILEPSY USING FUNCTIONAL NEAR INFRARED SPECTROSCOPY

KE PENG

INSTITUT DE GÉNIE BIOMÉDICAL

ÉCOLE POLYTECHNIQUE DE MONTRÉAL

THÈSE PRÉSENTÉE EN VUE DE L'OBTENTION

DU DIPLÔME DE PHILOSOPHIAE DOCTOR

(GÉNIE BIOMÉDICAL)

JUIN 2016

UNIVERSITÉ DE MONTRÉAL

ÉCOLE POLYTECHNIQUE DE MONTRÉAL

Cette thèse intitulée:

STUDY OF THE HEMODYNAMIC RESPONSE TO INTERICTAL EPILEPTIFORM DISCHARGES IN HUMAN EPILEPSY USING FUNCTIONAL NEAR INFRARED SPECTROSCOPY

présentée par : PENG Ke

en vue de l'obtention du diplôme de : Philosophiae Doctor

a été dûment acceptée par le jury d'examen constitué de :

M. DEHAES Mathieu, Ph. D., président

M. LESAGE Frédéric, Ph. D., membre et directeur de recherche

M. POULIOT Philippe, Ph. D., membre et codirecteur de recherche

M. PELLEGRINO Giovanni, M. D., membre

M. GOTMAN Jean, Ph. D., membre externe

DEDICATION

To my unborn daughter, Isabelle,
who has already brought lots of happiness and love to me and to my family.

ACKNOWLEDGMENTS

First and foremost I would like to express my gratitude and appreciation to my research supervisors, Prof. Frédéric Lesage and Dr. Philippe Pouliot, for giving me this wonderful opportunity as a Ph. D. student in their group, and for providing continued support throughout my entire Ph. D. study. A talk with Prof. Lesage is always enjoyable and inspiring, thanks to his profound knowledge in optical brain imaging, as well as his great patience at all times. It was his constant guidance that led me to this fascinating neuroimaging field and made me fall in love with it. I also greatly appreciate the help from Dr. Pouliot, who imparted his extensive experience to me, e.g. in signal processing, mathematical modelling, statistical analysis, coding, etc. His meticulous scholarship influenced me gradually but deeply on my attitude towards scientific research. To me, Prof. Lesage and Dr. Pouliot are not just research supervisors, but are also life mentors providing me with all kinds of opportunities and suggestions to help me design and develop my subsequent academic career.

I also would like to sincerely thank Dr. Dang Khoa Nguyen, who instructed me from time to time as if I were his own student. From the talks with him, I gained much knowledge, e.g. on human brain anatomy, brain functioning, epilepsy, all of which greatly helped me understand the clinical aspect of my project.

I must specially acknowledge my colleague, Ali Kassab, who spent quite a lot of his time in helping me design my experiment protocol, in testing our hardware setup and in acquiring data with me at the Notre-Dame hospital. His assistance truly facilitated my data acquisition work and was invaluable to me. I would like to thank Samuel Bélanger for his suggestions to improve the quality of the French text in this thesis, for useful discussions on my research, and for all the other help especially when I was still new to this lab.

I thank all the other past and current members of the laboratory of molecular and optical imaging at the Polytechnique Montreal: Clément Bonnéry, Michèle Desjardins, Baoqiang Li, Edgar Guevara, Mahnoush Amiri, Maxime Abran, Mohammad Moeini, Cong Zhang, Alexandre Castonguay, Hanieh Mohammadi, Joël Lefebvre, Parikshat Sirpal, Yuankang Lv, Ghada Jerbi, Xuecong Lv, Maryam Tabatabaei, Pier-Luc Tardif, Luis Akakpo, Azadeh Naderian, Sayed Mehran Sharafi, Nathan Yapi, and Patrick Delafontaine-Martel; all the past memebers of the Imaginc group at the Polytechnique Montreal, especially Prof. Mohamad Sawan; our other current

and former collaborators at the Notre-Dame Hospital: Manon Robert, Younes Zerouali and Tania Tayah; our collaborators at the Saint-Justine Hospital: Phetsamone Vannasing, Julie Tremblay, Prof. Anne Gallagher and Prof. Maryse Lassonde; and our collaborators at the University of Montreal and at the University Institute of Geriatrics of Montreal: Héloïse Auger, Prof. Mathieu Dehaes and Francis Comte.

Finally, I want to express my endless thanks to my family: to my parents who were always there to support me, encourage me, and prompt me throughout my study; and to my beloved wife who made me never feel lonely during this long journey in a city that is far from home.

RÉSUMÉ

L'imagerie spectroscopique proche infrarouge fonctionnelle (ISPIf) s'est imposée comme technique d'imagerie neuronale prometteuse. Cette dernière permet une surveillance non invasive de l'évolution chronique de l'activité hémodynamique corticale. Durant la dernière décennie, ISPIf combiné avec l'électroencéphalographie (EEG) a été appliqué dans le contexte de l'épilepsie humaine, et a permi d'explorer le lien entre l'activité neurale et hémodynamique. Cependant, la plupart des travaux antérieurs sont uniquement axés sur l'étude des crises d'épilepsie qui sont aléatoires et se produisent rarement pendant un test de l'EEG-ISPIf. Cette thèse cherche à évaluer la capacité de l'EEG-ISPIf à observer les changements hémodynamiques associés aux décharges épileptiformes intercritiques (DEIs), et à déterminer si ces DEIs peuvent également être utilisés pour extraire de l'information additionnelle servant à la localisation du site d'un foyer épileptique.

En se basant sur des données multimodales EEG-ISPIf recueillies sur un grand échantillon de patients (40), combiné à l'utilisation d'un modèle linéaire généralisé (MLG), une première étude a permis la quantification préliminaire de la sensibilité et la spécificité de la technique en utilisant la détection des zones cérébrales activées par des DEIs pour la localisation de la région du foyer épileptique. Dans un sous-groupe de 29 patients atteints au niveau de la région néocorticale, lorsque mesuré durant des évènements de DEIs, des diminutions de la concentration d'hémoglobine désoxygénée (HbR) (chez 62% des sujets) et des augmentations de la concentration de l'hémoglobine oxygénée (HbO) (chez 38% des sujets) ont été observées. De plus, cette variation en HbR et HbO était significativement plus forte dans la région du foyer épileptique (qui donc pourrait conduire à une localisation du foyer épileptique) dans 28% / 21% des patients. Ces estimations modestes de la sensibilité et de la spécificité suggèrent que l'utilisation d'une fonction de réponse hémodynamique (FRH) canonique n'est pas optimale dans l'analyse des DEIs par MLG classique. Par conséquent, une seconde approche a été explorée dans le cadre d'une deuxième étude par modélisation des variations spécifiques à chaque patient dans la construction de la réponse hémodynamique associée aux DEIs. Un terme quadratique a également été ajouté au modèle pour tenir compte de la non-linéarité de la réponse associée à une fréquence plus élevée d'évènements lors de l'enregistrement. Ces nouveaux modèles ont d'abord été validés numériquement par simulations, avant d'être appliqués à l'analyse de données de cinq patients sélectionnés. Lorsque comparée à la FRH canonique, l'utilisation de la FRH spécifique au patient dans l'analyse MLG a non seulement amélioré considérablement les scores statistiques et les étendues spatiales des

activations existantes, mais a aussi permis la détection de nouvelles régions du cerveau activées par des DEIs, et ce, sur l'ensemble des cinq patients. Ces améliorations dans la détection d'activations ont également permis d'obtenir des résultats plus précis dans la localisation du site de foyer épileptique dans certains cas.

Une fois de plus, les résultats présentés dans cette thèse ont confirmé le potentiel de l'EEG-fNIRS pour étudier les DEIs. Ils ont également démontré que la réalisation d'une analyse minutieuse et basée sur un modèle personnalisé serait nécessaire pour obtenir des résultats favorables. En travaillant sur ces limitations, l’EEG-ISPIf pourrait donc devenir un outil performant dans la surveillance chez les patients épileptiques, autant pour la mesure de l’évolution chronique de la condition que dans l'évaluation préopératoire.

ABSTRACT

Functional near-infrared spectroscopy (fNIRS) has emerged as a promising neuroimaging technique as it allows non-invasive and long-term monitoring of cortical hemodynamics. For the last decades, fNIRS combined with electroencephalography (EEG) has been applied in the context of human epilepsy, and has yielded good results. However, most previous work only focused on the study of epileptic seizures which are random and seldom occur during EEG-fNIRS testing. This thesis sought to evaluate the potential of EEG-fNIRS in observing the hemodynamic changes associated with interictal epileptiform discharges (IEDs), and to determine whether these IEDs can also be used to extract useful information in the localization of the epileptic focus site.

Based on the EEG-fNIRS data collected from a relatively large number of patients (40) and using a standard general linear model (GLM) approach, the first study of this thesis provided preliminary estimates of the sensitivity and the specificity of EEG-fNIRS in detecting brain areas activated by IEDs and in localizing the epileptic focus region. In the 29 patients with neocortical epilepsies, significant deoxygenated hemoglobin (HbR) concentration decreases and oxygenated hemoglobin (HbO) concentration increases corresponding to IEDs were observed in 62% and 38% of patients respectively. This HbR/HbO response was most significant in the epileptic focus region among all the activations, and thus could lead to successful identification of the epileptic focus site in 28%/21% of the patients. These modest estimates of the sensitivity and the specificity suggested that using a standard GLM with a canonical hemodynamic response function (HRF) might not be the optimal method in the analysis of IEDs. Therefore, the second study of this thesis made a first attempt to model the patient-specific variations in the shape of the hemodynamic response to IEDs. A quadratic term was also added to the model to account for the nonlinearity in the response when frequent IEDs were present in the recording. The new models were first validated through carefully designed simulations, and were then applied in the data analysis of five selected patients. Compared with the canonical HRF, including patient-specific HRFs in the GLM analysis not only significantly improved the statistical scores and the spatial extents of existing activations, but also was able to detect new brain regions activated by IEDs on all of the five patients. These improvements in activation detection also helped obtain more accurate focus localization results in some cases.

The results of this thesis again confirmed the potential of using EEG-fNIRS to study IEDs. They also demonstrated that conducting careful and model based analysis of patient data is required to yield favorable outcome. Should serval limitations be addressed in the future, combined EEG-fNIRS may be suitable to be used routinely in the epilepsy monitoring unit as a tool for long-term patient monitoring and presurgical evaluation.

TABLE OF CONTENTS

DEDICATION III

ACKNOWLEDGMENTS IV

RÉSUMÉ VI

ABSTRACT VIII

TABLE OF CONTENTS X

LIST OF TABLES XV

LIST OF FIGURES XVI

LIST OF SYMBOLS AND ABBREVIATIONS XXI

CHAPTER 1 INTRODUCTION 1

1.1 Epilepsy 1

1.2 Functional near infrared spectroscopy 2

1.3 Problem statement 3

1.4 Objectives, hypotheses and research work overview 4

CHAPTER 2 LITERATURE REVIEW 7

2.1 Neurovascular coupling and hemodynamic response function 7

2.2 Current functional neuroimaging techniques for human epilepsy 9

2.2.1 Electroencephalography 10

2.2.2 Magnetoencephalography 11

2.2.3 Combined EEG-fMRI 12

2.2.4 Ictal Single photon emission computed tomography 14

2.2.5 18F-fluorodeoxyglucose positron emission tomography 15

2.2.6 Combined EEG-fNIRS 15

CHAPTER 3 THEORY AND METHODOLOGY 23

3.1 Brief introduction of diffuse optical imaging basics 23
3.1.1 Forward modeling and inverse problem 23
3.1.2 The differential pathlength approach 25
3.2 Multichannel EEG-fNIRS recording methods 26
3.2.1 System setup and recording protocol 26
3.2.2 Data processing and statistical analysis 28
CHAPTER 4 ARTICLE #1: FNIRS-EEG STUDY OF FOCAL INTERICTAL EPILEPTIFORM DISCHARGES 36
4.1 Abstract 36
4.2 Introduction 37
4.3 Methods 38
4.3.1 Simultaneous EEG-fNIRS recording 38
4.3.2 Data Processing 40
4.3.3 Coregistration and contrasts 40
4.3.4 Sensitivity & specificity definition 41
4.4 Results 42
4.4.1 EEG-fNIRS response in neocortical epilepsies versus mesial temporal lobe epilepsies 44
4.4.1.1 Neocortical epilepsies 44
4.4.1.2 Mesial temporal lobe epilepsies 49
4.4.2 Overall concordance between EEG-fNIRS response and epileptic focus region 49
4.5 Discussion 49
4.5.1 Sensitivity and Specificity estimates 50
4.5.2 Remote hemodynamic responses 51
4.5.3 Limitations 51

4.6 Conclusion....52
4.7 Acknowledgments....53
4.8 Appendix....53
4.9 References....56
CHAPTER 5 ARTICLE #2: USING PATIENT-SPECIFIC HEMODYNAMIC RESPONSE FUNCTION IN EPILEPTIC SPIKE ANALYSIS OF HUMAN EPILEPSY: A STUDY BASED ON EEG-FNIRS....60
5.1 Abstract....60
5.2 Introduction....61
5.3 Method....63
5.3.1 Reconstruction of a specific HRF....63
5.3.1.1 The nonlinear deconvolution model....63
5.3.1.2 Presentation of confidence levels....64
5.3.2 Simulation methodology....64
5.3.2.1 Baseline signal used for the simulation....64
5.3.2.2 Stimulus sequence protocols and simulated signal pre-processing....65
5.3.2.3 Model validation with simulations....66
5.3.3 Epileptic patient data acquisition and analysis....67
5.3.3.1 Simultaneous EEG-fNIRS recording....68
5.3.3.2 Data Pre-processing and HRF reconstruction....68
5.3.3.3 Statistical parametric mapping with patient-specific sHRFs....69
5.4 Results....70
5.4.1 Simulation results....70
5.4.2 Patient results....74
5.4.2.1 Case study - Patient 2....77

5.4.2.2 Case study - Patient 4 77
5.4.3 Summary of patient results 78
5.5 Discussion 81
5.5.1 Criteria for sHRF comparison 81
5.5.2 HbO vs. HbR 82
5.5.3 Localization of the epileptic focus 82
5.5.4 Early response preceding IEDs 83
5.5.5 Limitations 83
5.6 Conclusion 84
5.7 Acknowledgments 85
5.8 Appendix 85
5.8.1 Specific HRF estimation 85
5.8.1.1 Nonlinear deconvolution model 85
5.8.1.2 Linear deconvolution model 86
5.8.2 Supplementary patient results 87
5.8.2.1 Patient 1 87
5.8.2.2 Patient 3 88
5.8.2.3 Patient 5 88
5.9 References 95
CHAPTER 6 GENERAL DISCUSSION 102
6.1 Objective 1 102
6.2 Objective 2 103
6.3 Limitations of fNIRS in current study of epilepsy 107
CHAPTER 7 CONCLUSION AND RECOMMANDATION 110

BIBLIOGRAPHY 111

LIST OF TABLES

Table 2.1 Summary of the literature on EEG-fNIRS in human epilepsy (Other groups) 17

Table 2.2 Summary of the results of our group using EEG-fNIRS in human epilepsy 20

Table 4.1 Types and total numbers of IEDs identified on EEG recordings 43

Table 4.2 Hemodynamic response regions of focal IEDs in neocortical epilepsy (HbR) 47

Table 4.3 Hemodynamic response regions of focal IEDs in neocortical epilepsy (HbO/HbT) 54

Table 4.4 Hemodynamic response regions of focal IEDs in mesial temporal lobe epilepsy (HbR/HbO/HbT) 55

Table 5.1 Types and numbers of IEDs observed on EEG for the five selected patients. 74

Table 5.2 Summary of patient results. Hemodynamic response congruent with focus: location and peak *t*-statistic value. An up arrow ↑ (down arrow ↓) indicates that an increase (resp. a decrease) in the hemoglobin concentration was observed in the corresponding locations, while a double arrow sign ↑ ↑ or ↓ ↓ indicates that the given activation was recognized as being the most significant among all the activations of the same hemoglobin type on the current set of contrast maps. The distribution of nonlinear coefficients ($\lambda/2$) and ratios of mean nonlinear to linear amplitudes (A_{nl}/A_l) is described using median value and median absolute deviation (MAD) to mitigate the influence of outlier channels. The negative sign of $\lambda/2$ and A_{nl}/A_l indicated an inhibitory effect of nonlinear components to linear components in the response. 80

Table 5.3 Summary of focus localization results of the five patients. 94

LIST OF FIGURES

Figure 1.1 (A) Schematic diagram of the near infrared light propagation through different layers of the head. (B) Light absorption spectra of major chromophores, reproduced from (Nguyen, 2010).....2

Figure 2.1: Hemodynamic response measured on 7 healthy subjects using fNIRS (for HbO, HbR and HbT) or diffuse correlation spectroscopy (for CBF) (Desjardins et al., 2009). 8

Figure 2.2: Depiction of the Gamma HRF, the Glover HRF and the SPM canonical HRF modelled for BOLD signals, reproduced from Lu et al., (2006).....9

Figure 3.1: (A) Example of helmet configuration in one simultaneous EEG-fNIRS recording on an epileptic patient (B) Co-registered optode distribution projected onto the scalp: sources/detectors are marked in blue/green respectively. 27

Figure 3.2 Flowchart of EEG-fNIRS data processing and statistical analysis pipeline using the nirs10 toolbox.....32

Figure 4.1 Patient #36. (A) MEG dipole localization of epileptic spikes revealing a cluster of sources in the L inferior frontal gyrus and L anterior insula. (B) Reconstructed NIRS channel map over grey matter layer (Left view). (C) EEG fragment with marking for L fronto-temporal and bi-frontal IEDs. (D) Hemodynamic response (HbR) to R fronto-temporal IEDs (Type I) at patient-level (2D-pFDR corrected, $p<0.05$). Solid green circle (30mm radius): focus region; dashed green circle: contralateral region corresponding to focus. (E) HbR response to bi-frontal IEDs (Type II). 45

Figure 4.2 Patient #7. (A) MEG dipole localization of epileptic spikes revealing a cluster of sources in the right inferior frontal gyrus. (B) Reconstructed NIRS channel map over grey matter layer (Right view). (C) EEG fragment with marking for right fronto-temporal IEDs. (D) Hemodynamic responses to right fronto-temporal IEDs, patient level (2D-pFDR corrected, $p<0.05$). Solid green circle (30mm radius): focus region; dotted green circle: contralateral region corresponding to focus. 46

Figure 5.1 (A) Depiction of one random pulse stimulus sequence generated using a Poisson process with incidence rate of 20 per minute (or with expectation of stimulus interval of 3s). (B)

Simulated hemodynamic responses of the stimulus sequence with different nonlinear coefficients. 65

Figure 5.2 Hemodynamic responses computed from Figure 5.1 after adding a same baseline chosen as one typical HbO channel (channel 5) recording from one patient. SNR = -2db. 66

Figure 5.3 Reconstructed linear sHRFs and nonlinear sHRFs in one simulation. HbO channel 5 was used as baseline. Stimulus sequence protocol and simulated signals were shown in Figure 5.1 and in Figure 5.2. The original SPM8 cHRF as well as the filtered SPM8 cHRF are also plotted for comparison. Nonlinear coefficient λ/2 = (A) 0; (B) -0.2; (C) -0.6. Confidence levels ($p<0.05$) for HPA were calculated using the surrogate series method. 70

Figure 5.4 Simulation results with constant SNR = -2dB and varying nonlinear coefficient λ/2 from 0 to -0.6: (A) Mean value and standard deviation of the Pearson's correlation coefficients between the true HRF and either the reconstructed linear or nonlinear sHRFs from channels without true response (NR) and (B) with responses at different nonlinear coefficients. (C) Mean value and standard deviation of HPAs of linear sHRFs and nonlinear sHRFs, also for channels without true response (NR) and with responses at different nonlinear coefficients. HPAs have been normalized as explained in the text. P-values from Wilcoxon signed-rank test were averaged over 16 channels and displayed for HPA comparison.....71

Figure 5.5 Results from similar simulations as in Fig. 4 but this time with constant nonlinear coefficient λ/2 = -0.2 and varying SNR from -15dB to -2dB. 72

Figure 5.6 Simulation results: detectability of nonlinearity using the nonlinear algorithm under the HPA criterion. (A) ROC curves for using the significance of HPA difference (p-value) of linear sHRFs and nonlinear sHRFs to detect nonlinear channels. SNR was fixed at -2dB. ROC curves at a λ/2 more negative than -0.2 (e.g. -0.4 or -0.6) maintained a same shape as that at λ/2 = -0.2. The arrows indicate a threshold of p = 0.05 on each ROC curve. (B) ROC curves of nonlinearity detection of channels at different SNRs with λ/2 = -0.2. 73

Figure 5.7 Patient 2. (A) MEG dipole localization of IEDs revealing a cluster of sources located in the left middle occipital gyrus; (B) EEG fragment with marking for left tempo-occipital IEDs; (C) Interpolated maps of nonlinear sHRFs, from 10s before an IED to 35s after the IED (left view); (D) The covered brain areas of the three selected ipsilateral channels with highest HPAs; (E) The reconstructed linear sHRF and nonlinear sHRF of channel 49 and 62. Compared with

linear sHRFs, the first peak of the nonlinear sHRFs was greatly enhanced. Confidence levels of each deconvolved sHRF were presented using the surrogate method; (F) T-statistical maps of HbO, HbR and HbT response to left tempo-occipital IEDs, generated from GLMs using respectively the SPM8 canonical HRF (the first row), linear sHRFs (the second row) and nonlinear sHRFs (the third row). T-maps were EC-corrected, $p<0.05$. Solid black circle (30mm radius) indicates the projected most plausible focus region; dotted black circle shows the contralateral region corresponding to focus. 75

Figure 5.8 Patient 4. (A) MEG dipole localization of IEDs revealing a cluster of sources located in the posterior portion of inferior temporal gyrus; (B) EEG fragment with marking for right temporal IEDs and right fronto-temporal IEDs; (C) Interpolated maps of nonlinear sHRFs, from 10s before an IED to 35s after the IED (right view); (D) The covered brain areas of the three selected ipsilateral channels with highest HPAs; (E) The reconstructed linear sHRF and nonlinear sHRF of channel 6 and 12. Nonlinear sHRFs clearly showed higher HPAs. Both the linear and the nonlinear sHRFs peaked later than the cHRF, at around 12s; (F) T-statistical maps of HbO, HbR and HbT response to IEDs combined from right temporal IEDs and right fronto-temporal IEDs, generated from GLMs using respectively the SPM8 canonical HRF (the first row), linear sHRFs (the second row) and nonlinear sHRFs (the third row). T-maps were EC-corrected, $p<0.05$. Solid black circle (30mm radius) indicates the projected most plausible focus region; dotted black circle shows the contralateral region corresponding to focus. 76

Figure 5.9 Ipsilateral hemisphere of the epileptic focus (circled in black) for the 5 patients: depiction of the first order Volterra component (the linear term, V1) and the second order Volterra component (the nonlinear term, V2) in the expected HbO response reconstructed using the nonlinear sHRFs. Only channels that presented significant nonlinear activations were chosen for interpolation (Bonferroni threshold). For each selected channel, the mean amplitudes of the V1 term and of the V2 term in the expected response were calculated. For illustration purposes, the mean V1 amplitudes and the mean V2 amplitudes of a patient were both normalized so that the highest mean V1 amplitude had a unit value. 79

Figure 5.10 Patient 1. (A) MEG dipole localization of IEDs revealing a cluster of sources located in the right inferior frontal gyrus; (B) EEG fragment with marking for right frontal IEDs; (C)

Interpolated maps of nonlinear sHRFs, from 10s before an IED to 35s after the IED (right view); (D) The covered brain areas of the three selected ipsilateral channels with highest HPAs; (E) The reconstructed linear sHRF and nonlinear sHRF of channels 18 and 11. The HPAs of nonlinear sHRFs were nearly twice as much as those of linear ones. Confidence levels of each deconvolved sHRF were presented using the surrogate series method; (F) T-statistical maps of HbO, HbR and HbT response to right frontal IEDs, generated from GLMs using respectively the SPM8 canonical HRF (first row), linear sHRFs (second row) and nonlinear sHRFs (third row). T-maps were EC-corrected, $p<0.05$. Solid black circle (30mm radius): projected most plausible focus region; dotted black circle: contralateral region to the focus. 90

Figure 5.11 Patient 3. (A) MEG dipole localization of IEDs revealing a cluster of sources located in the junction of right orbitofrontal areas and operculum-anterior insula; (B) EEG fragment with marking for right fronto-temporal IEDs; (C) Interpolated maps of nonlinear sHRFs, from 10s before an IED to 35s after the IED (right view); (D) The covered brain areas of the three selected ipsilateral channels with highest HPAs; (E) The reconstructed linear sHRF and nonlinear sHRF of channel 16 and 120. Nonlinearity was seen to be the most significant near channel 16. Confidence levels of each deconvolved sHRF were presented using the surrogate method; (F) T-statistical maps of HbO, HbR and HbT response to right fronto-temporal IEDs, generated from GLMs using respectively the SPM8 canonical HRF (the first row), linear sHRFs (the second row) and nonlinear sHRFs (the third row). T-maps were EC-corrected, $p<0.05$. Solid black circle (30mm radius) indicates the projected most plausible focus region; dotted black circle shows the contralateral region corresponding to focus.....91

Figure 5.12 Patient 5. (A) MEG dipole localization of IEDs revealing a cluster of sources located at occipito-temporal junction; (B) EEG fragment with marking for right parieto-occipito-temporal (POT) IEDs, bilateral POT IEDs and general spike and waves; (C) Interpolated maps of nonlinear sHRFs, from 10s before an IED to 35s after the IED (right view); (D) The covered brain areas of the three selected ipsilateral channels with highest HPAs; (E) The reconstructed linear sHRF and nonlinear sHRF of channel 19 and 14. Both types of sHRFs were quite different from the cHRF in characteristics such as peaking time and full width at half maximum of the main peak; (F) T-statistical maps of HbO, HbR and HbT response to IEDs combined from right POT IEDs, bilateral POT IEDs and general spike and waves, generated

from GLMs using respectively the SPM8 canonical HRF (the first row), linear sHRFs (the second row) and nonlinear sHRFs (the third row). T-maps were EC-corrected, $p<0.05$. Solid black circle (30mm radius) indicates the projected most plausible focus region; dotted black circle shows the contralateral region corresponding to focus. 92

Figure 5.13 Simulation results: detectability of nonlinearity under the criteria of HPA or AUC. (A) ROC curves for HPA or AUC to detect nonlinear signals at two different nonlinear coefficients. SNR was fixed at -2dB. The arrow indicates a threshold of $p = 0.05$ on each ROC curve. (B) ROC curves for HPA or AUC at different SNRs, with $\lambda = -0.2$. HPA was a better indicator than AUC at low SNRs. 93

Figure 6.1 Test result without PCA for (A) Patient 2, (B) Patient 4: T-statistical maps of HbO, HbR and HbT response to IEDs, generated from GLMs using respectively the SPM8 canonical HRF (the first row), linear sHRFs (the second row) and nonlinear sHRFs (the third row). T-maps were EC-corrected, $p<0.05$. Solid black circle (30mm radius) indicates the projected most plausible focus region; dotted black circle shows the contralateral region corresponding to focus. 105

Figure 6.2 Test result, T-statistical maps. Expected hemodynamic response was derived using only one channel with the highest HPA for (A) Patient 2, (B) Patient 4. 106

LIST OF SYMBOLS AND ABBREVIATIONS

2D	Two-dimensional
3D	Three-dimensional
AED	Antiepileptic drug
ATP	Adenosine 5'-triphosphate
BOLD	Blood-oxygenation-level-dependent
CBF	Cerebral blood flow
CBV	Cerebral blood volume
CSF	Cerebrospinal fluid
DE	Diffusion equation
DOF	Degree of freedom
DOT	Diffuse optical tomography
DPF	Differential pathlength factor
EC	Euler characteristics
ECoG	Electrocorticography
EEG	Electroencephalography
EDoF	Effective degree of freedom
EKG	Electrocardiogram
FDG-PET	18F-fluorodeoxyglucose positron emission tomography
FWER	Familywise error rate
FWHM	Full width at half maximum
GLM	General linear model
HRF	Hemodynamic response function
HbO	Oxygenated hemoglobin

HbR	Deoxygenated hemoglobin
HbT	Total hemoglobin
IED	Interictal epileptiform discharge
MBLL	Modified Beer-Lambert Law
MEG	Magnetoencephalography
MRI	Magnetic resonance imaging
MTLE	Mesial temporal lobe epilepsy
NIRS	Near infrared spectroscopy
OD	Optical density
PCA	Principal component analysis
pFDR	Peak false discovery rate
PPF	Partial pathlength factor
PVF	Partial volume factor
RTE	Radiative transport equation
SEEG	Stereoelectroencephalography
SNR	Signal-to-noise ratio
SPECT	Single photon emission computed tomography
SPM	Statistical parametric mapping
TRS	Time-resolved spectroscopy

CHAPTER 1 INTRODUCTION

1.1 Epilepsy

Epilepsy currently affects approximately 50 million people worldwide, making it one of the most common neurological diseases globally (World Health Organization, 2016). Epilepsy is a common and diverse set of chronic neurological disorders that can be characterized by spontaneous, recurrent epileptic seizures (Chang and Lowenstein, 2003; Engel and Pedley, 2008). A seizure, which can last from a few seconds to several minutes, is the result of abnormal, excessive neuronal discharges, and is therefore usually accompanied by clinical manifestations such as altered mental state, tonic/clonic movements, and other various experiential symptoms (Blume et al., 2001; Fisher et al., 2005; Gotman, 2011). Uncontrolled seizures are not only a major personal handicap but also represent a considerable public health burden due to high use of health care resources and high number of disability days or unemployment (Megiddo et al., 2016; Tellez-Zenteno et al., 2004; Wiebe et al., 1999).

About 60% of patients with epilepsy have syndromes of focal seizures (Panayiotopoulos, 2005). A seizure is called “focal” or “partial” if it is generated in one part of the brain and is initially associated with unilateral brain hemisphere involvement, as opposed to generalized seizures which originate from the whole or a large portion of the brain. In between the seizures (or “ictus”), brief paroxysmal discharges (normally from 20 to 200 ms) may occur, and are thus called “interictal epileptiform discharges” (IEDs, a.k.a. spikes). IEDs have been shown to be spatially correlated with seizures and are also considered to be fundamental components contributing to epileptogenesis (Gotman, 2008, 1991; Gotman et al., 2006; Palmini, 2006; Staley and Dudek, 2006).

The traditional treatment of a patient’s epilepsy normally starts with the prescription of antiepileptic drugs (AEDs). However, medication fails to control epileptic seizures in around 30% of the patients (Eadie, 2012), in which case alternative treatments such as epilepsy surgery (Duncan et al., 2016; Kwon et al., 2016), neurostimulation (Bergey, 2013), or dietary therapy (Felton and Cervenka, 2015) might be more suitable. Epilepsy surgery is an operation to control seizures by resecting or disconnecting the brain area that is indispensable for the generation of clinical seizures (known as the epileptogenic zone, or most equivalently, the epileptic focus region) (Lüders et al.,

2006; Nadler and Spencer, 2014; Rosenow and Lüders, 2001). Recent reports revealed that about half of the patients with drug-resistant focal epilepsy are potential candidates of an epileptic surgery (Duncan et al., 2016), and that epileptic surgery usually leads to good seizure freedom outcomes (34% to 74% of seizure freedom rate depending on different reports) (Jobst and Cascino, 2015). Research to evaluate the eligibility of a patient for an epilepsy surgery and to better predict the outcomes of the surgery relies on the application of contemporary neuroimaging techniques both in clinical diagnosis, especially in the precise identification of the epileptic focus region (De Ciantis and Lemieux, 2013; Ramli et al., 2015), and to understand the mechanism of epilepsy at a more fundamental level (Ryvlin and Rheims, 2016).

1.2 Functional near infrared spectroscopy

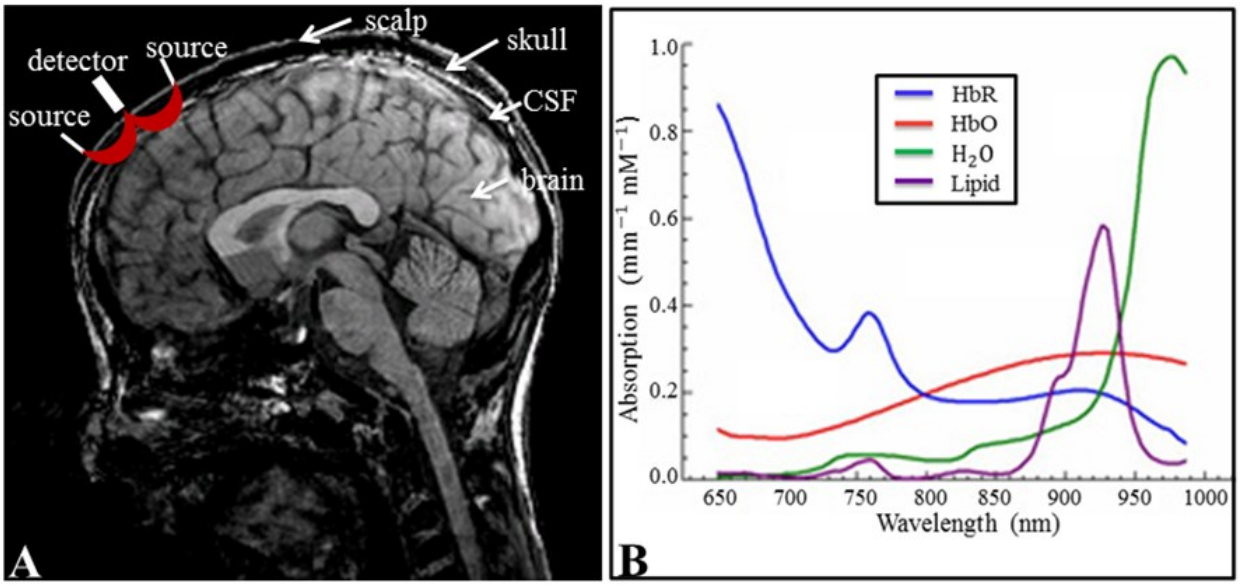

Figure 1.1 (A) Schematic diagram of the near infrared light propagation through different layers of the head. (B) Light absorption spectra of major chromophores, reproduced from (Nguyen, 2010).

Functional near-infrared spectroscopy (fNIRS) is a non-invasive neuroimaging technique that is capable of continuously monitoring tissue oxygenation and cortical hemodynamics in the brain (Jöbsis, 1977). When light within the near infrared wavelength range (650nm to 900nm) is projected onto the scalp by optical emitters, it is able to travel for a few centimeters before eventually being captured by light detectors. Photon transport theory (Delpy et al., 1988) suggests that the averaged path of photon propagation follows a roughly banana-shaped pattern (Haeussinger et al., 2011; Okada et al., 1997), see Figure 1.1A. Previous simulation studies showed

that keeping a distance of three to five centimeters between an emitter and a detector usually ensures a light penetration depth of one to two centimeters (Strangman et al., 2013), and thus a reasonable sensitivity within the top two to three millimeters of the brain cortex (Irani et al., 2007).

During its propagation in brain tissue, near infrared light attenuates as a result of reflectance, scattering, and absorption. A simplifying assumption is made that reflectance and scattering usually remain at a constant level for a certain wavelength of light if travelling along the same trajectory (Desjardins et al., 2012). Therefore, variations in light intensity detected by the detectors are considered to be due to the changes in absorption, which is dominated by its main light absorbers: HbO and HbR (Figure 1.1B). Continuous measurement of near infrared light attenuation enables the reconstruction of local HbO and HbR concentration changes, and thus allows long-term monitoring of cortical hemodynamics.

1.3 Problem statement

Recent work of our group and others has explored the potential of fNIRS, combined with electroencephalography (EEG), in the context of human epilepsy (Obrig, 2014). Hemodynamic brain responses attributed to epileptic events, mostly seizures, are routinely observed with a good degree of statistical significance and in concordance with clinical presentation. Especially, previous studies with a large fNIRS head coverage suggested the potential of using EEG-fNIRS as a focus localization tool for focal seizures (Nguyen et al., 2013, 2012; Watanabe et al., 2002). Unfortunately, as seizures are unpredictable, one may not always be able to record seizures even during a prolonged EEG-fNIRS recording. It is likely, however, that IEDs will be recorded as they are typically numerous in patients with drug-refractory focal epilepsy. A few recent studies have showed that the hemodynamic response to IEDs was also observable with fNIRS (Machado et al., 2011; Pellegrino et al., 2016; Pouliot et al., 2012). However, the overall sensitivity and specificity in detecting brain regions activated by IEDs and in localizing the epileptic focus were not estimated due to the limited number of patients involved in those studies.

Furthermore, current observations on the cortical hemodynamics in epilepsy are still confounded in many ways. For example, the relation between the fNIRS-measured hemodynamic change and the underlying epileptiform discharge is not fully understood. The neurovascular coupling mechanism during normal cortical processing may not apply to the epileptic conditions (Schwartz, 2007), as supported by many evidences including Masterton et al. (2010), showing that the

hemodynamic response to IEDs did not follow a canonical shape in their patients with benign rolandic epilepsy (please refer to chapter 2 for a detailed description of neurovascular coupling and hemodynamic response). Such variability in the hemodynamic response may complicate the interpretation of EEG-fNIRS data and decrease the localization accuracy using IEDs. Although many methods have been applied for fMRI to account for the patient-specific hemodynamic response shape in BOLD signals, similar work has never been done for fNIRS. Whether a simple but robust model can be proposed for fNIRS data processing remains to be investigated.

1.4 Objectives, hypotheses and research work overview

The general objective of this Ph.D. project is to (1) confirm the usefulness of EEG-fNIRS in detecting the hemodynamic response to IEDs and in localizing the epileptic focus in a relatively controlled setting, e.g. the epilepsy monitoring unit, with chronic drug-refractory epileptic patients; (2) support the understanding of the complex oxygenation process and network associated with IEDs in focal epilepsy.

Two individual objectives are stated below with corresponding hypotheses.

Objective 1: Based on the EEG-fNIRS data collected from a relatively large number of patients, provide a preliminary assessment of the sensitivity and the specificity in detecting the hemodynamic response (hemoglobin) to IEDs and in localizing the epileptic focus region.

Hypothesis 1-1: Both the local and the remote hemoglobin concentration changes associated with IEDs can be detected using multichannel EEG-fNIRS with a large head coverage.

Hypothesis 1-2: The local hemodynamic response to IEDs follows the neurovascular coupling mechanism during normal cortical processing, and thus has a similar shape to the canonical hemodynamic response function.

Article 1: **Peng, K.**, Nguyen, D.K., Tayah, T., Vannasing, P., Tremblay, J., Sawan, M., Lassonde, M., Lesage, F., and Pouliot, P., fNIRS-EEG study of focal interictal epileptiform discharges. *Epilepsy Research*, 108(3), 491–505, 2014.

Objective 2: Develop and implement new analysis methods to process EEG-fNIRS data that model the patient-specific variations in the shape of the hemodynamic response function to IEDs.

Hypothesis 2-1: The shape of the hemodynamic response function to IEDs varies across time, patients and brain regions. Besides, the relation between IEDs and the associated hemodynamic response is not linear if very frequent IEDs are present.

Hypothesis 2-2: Compared with a canonical hemodynamic response function, including a hemodynamic response function that is specific to a patient in data analysis improves the ability of EEG-fNIRS in detecting the brain regions activated by IEDs as well as in localizing the epileptic focus site.

Article 2: **Peng, K.**, Nguyen, D.K., Vannasing, P., Tremblay, J., Lesage F., and Pouliot P., Using patient-specific hemodynamic response function in epileptic spike analysis of human epilepsy: a study based on EEG-fNIRS, *NeuroImage*, 126, 239–255, 2016.

In parallel, auxiliary collaborative work during this thesis have led to other publications:

Review article on the literature of using multi-channel EEG-fNIRS to study focal seizures and IEDs in human epilepsy, co-written by four authors:

Peng, K., Pouliot, P., Lesage, F., and Nguyen, D.K., Multi-channel continuous EEG-fNIRS recording of focal seizures and interictal epileptiform discharges in human epilepsy: a review, *NeuroPhotonics*, 3(3), 031402, 2016.

Article on assessing the possibility of using combined continuous wave fNIRS and time resolved spectroscopy (TRS) to monitor cortical tissue oxygen saturation variations during language production on epileptic patients, for which I designed the experiment protocol, participated in the data acquisition as well as performed the data analysis and interpretation:

Peng, K., Kassab, A., Nguyen, D.K., Auger, H., Dehaes, M., Hoge, R., Lesage F., and Pouliot P., Observing cortical tissue oxygen saturation variations during language production on patients with epilepsy using combined functional near infrared spectroscopy and time resolved spectroscopy, *in preparation*.

Article on the study of cortical hemodynamic changes during status epilepticus, for which I analyzed the EEG-fNIRS data related to IEDs:

Kassab, A., **Peng, K.**, Tremblay, J., and Nguyen, D.K., Clinical application of functional near infrared spectroscopy in epileptic patients in the intensive care, *in preparation*.

This thesis is organized as follows. Chapter 2 gives a brief literature review on neurovascular coupling during normal cortical processing, as well as the application of current functional neuroimaging techniques in human epilepsy study. Chapter 3 briefly introduces the diffuse optical imaging basis, and describes the methodology of this study in details (including both the hardware setup and the data analysis). In chapter 4 and chapter 5, two published papers are fully included to address the first two individual objectives. General discussions and conclusions of the entire study are provided in chapter 6 and 7 respectively.

CHAPTER 2 LITERATURE REVIEW

2.1 Neurovascular coupling and hemodynamic response function

Neurovascular coupling describes the relationship between local neural activity and the subsequent changes in cerebral blood flow (Huneau et al., 2015). It is considered as the basis of many functional neuroimaging techniques, e.g. fNIRS, which rely on this coupling to infer underlying neural activity from observed hemodynamic changes (Liao et al., 2013). This section gives a brief review of the neurovascular coupling and hemodynamic response during normal cortical processing. However, as stated in section 1.3, it should be noted that the coupling is likely to be altered in many pathologies (Girouard and Iadecola, 2006), including epilepsy (Schwartz, 2007). Therefore, understanding the link between epileptic events and their hemodynamic response remains a vital area of research (Voges et al., 2012).

Various cellular processes of neurons consume energy, in terms of the adenosine 5'-triphosphate (ATP) (e.g. reestablishing resting membrane potential or recycling neurotransmitters). ATP is first synthesized by anaerobic glycolysis, but is mostly provided through mitochondrial oxidative phosphorylation in glucose metabolism, a process which requires a constant supply of both oxygen and glucose (Sperlágh and Vizi, 1996; Surin et al., 2012). Therefore, when a brain region is activated, e.g. by a stimulus, it poses extra demand on the need of oxygen and glucose, and thus triggers an increase in regional cerebral blood flow (rCBF) which is responsible to deliver those two energy substrates. However, as the increase in blood flow is more coupled with glucose consumption (Paulson et al., 2010), the loss in oxygen is actually overcompensated, leading to a net increase of regional oxygen concentration. This process can be explicitly described by the emerging model of the oxygen response (Heeger and Ress, 2002) with the following three phases: 1- increased neural activity triggers an increase in oxygen consumption, resulting in a temporary decrease in local oxygen concentration (HbO ↓, HbR ↑); 2- after a delay of one to two seconds, a large increase in rCBF triggered by the same neural activity overcompensates the consumption of oxygen, and significantly increases the ratio of local HbO concentration to HbR concentration (HbO ↑, HbR ↓); 3- the ending of the oxygenated blood oversupply gradually brings the concentration of both HbO and HbR to the baseline level. For example, figure 2.1A depicts the

hemodynamic response (hemoglobin and blood flow) measured on 7 healthy subjects (Desjardins et al., 2009).

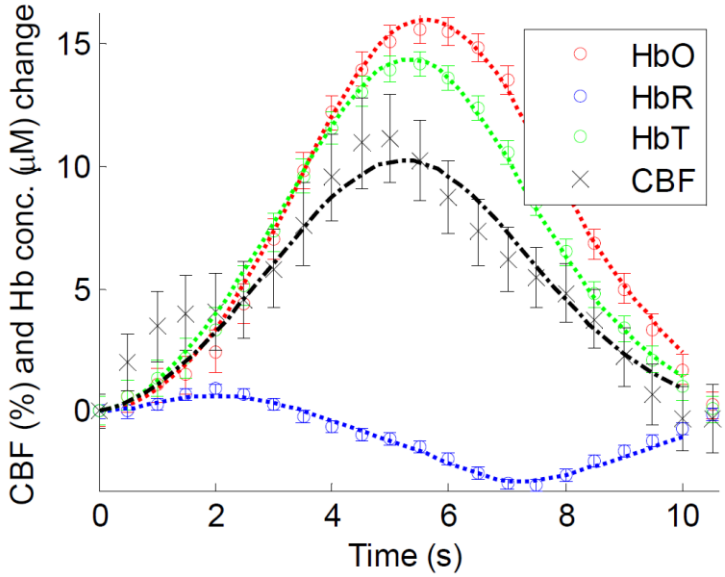

Figure 2.1: Hemodynamic response measured on 7 healthy subjects using fNIRS (for HbO, HbR and HbT) or diffuse correlation spectroscopy (for CBF) (Desjardins et al., 2009).

Considering the vascular bed within a small volume of tissue as an expandable compartment (e.g. the balloon model), the vasodilation of the venules and veins during the perfusion of extra blood flow also causes an increase in regional cerebral blood volume (rCBV) (Buxton et al., 2004, 1998) which can be reflected by the increase in the concentration of total hemoglobin (HbT) in Figure 2.1 under the widely accepted hypothesis of constant hematocrit (Boas et al., 2003; Hoge et al., 2005; Lloyd-Fox et al., 2010).

These changes in HbR concentration and in rCBV produce variations in the blood-oxygenation-level-dependent (BOLD) signals, the most common functional image signal that can be depicted with a BOLD-functional magnetic resonance imaging (BOLD-fMRI) system (Arthurs and Boniface, 2002; Buxton et al., 1998). Different methods have been applied to propose a function, namely the hemodynamic response function (HRF), that represents a typical shape of the BOLD response to the neural activity of an impulse stimulus, e.g. using Poisson function (Friston et al., 1994), Gaussian function (Rajapakse et al., 1998), or Gamma-variate function (Friston et al., 1998; Worsley et al., 2002). Figure 2.2 depicts the shapes of the Gamma HRF (Cohen, 1997), the Glover HRF (Glover, 1999) and the SPM canonical HRF (Friston et al., 2007) modelled for BOLD-fMRI.

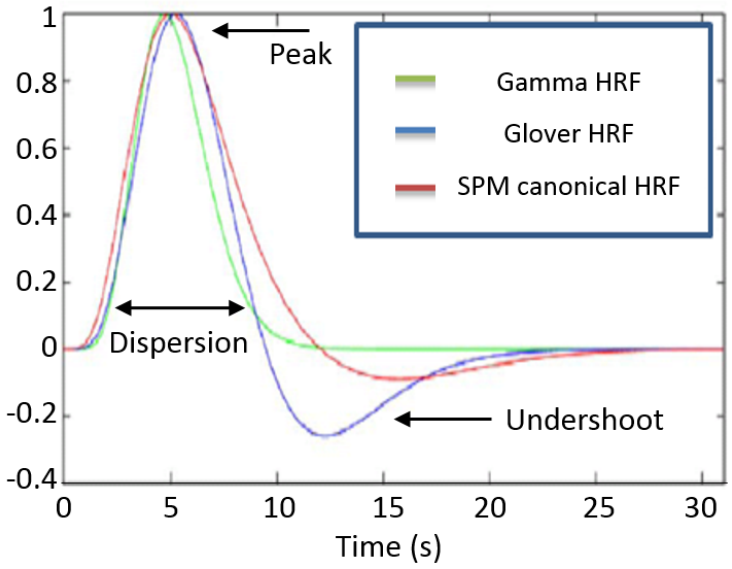

Figure 2.2: Depiction of the Gamma HRF, the Glover HRF and the SPM canonical HRF modelled for BOLD signals, reproduced from Lu et al., (2006).

As seen in Figure 2.2, an HRF for BOLD signals retains a shape that starts with a significant positive peak within 4 to 6 seconds after the stimulus, normally followed by a relatively smaller negative nadir (the "undershoot") that can persist for as long as 30 seconds (Friston et al., 2007). While the positive peak is a result mainly of the decrease in HbR in the second phase of the emerging model introduced above, the "undershoot" corresponds to a situation in the third phase that the blood volume returns to baseline more slowly than blood flow, leading to an increase in local HbR concentration (Buxton et al., 1998). Moreover, it should also be noted that some studies have also reported a decrease (1-2s) of the BOLD signal shortly after the stimulus onset but prior to the normal peak increase (Ernst and Hennig, 1994; Hu et al., 1997; Malonek and Grinvald, 1996; Menon et al., 1995; Yacoub and Hu, 2001), especially when operating at high static magnetic field strengths (e.g. > 3 Tesla) (Uludag, 2010; Uludağ et al., 2009). This decrease is denoted as the "initial dip", and is believed to reflect the transient mismatch between the increased metabolism and the CBF increase (i.e. the first phase in the emerging model) (Hu and Yacoub, 2012). However, the dip is small is not always presented in the observation (Buxton, 2001; Lindauer et al., 2001).

2.2 Current functional neuroimaging techniques for human epilepsy

The presurgical evaluation of a patient with epilepsy first includes the application of structural Magnetic Resonance Imaging (MRI), a preferred technique to determine the extent of an

epileptogenic lesion as well as the relation of the lesion to eloquent cortex (Duncan et al., 2016). However, recent reports estimated that more than 20% of patients with refractory focal epilepsy are “MRI-negative” (or “nonlesional”), meaning that no distinct lesion can be recognized on their MRI images (Bien CG et al., 2009; Oertzen et al., 2002; Téllez-Zenteno et al., 2010). On some other patients, the structural findings may also be discordant with their clinical semiology (Castro et al., 2008; Rysz et al., 1998). In this case, functional mapping of epileptic activities needs be considered.

2.2.1 Electroencephalography

The most utilized (and the earliest) functional neuroimaging technique to directly visualize abnormal neural activities is to perform a multichannel electroencephalography (EEG) recording (Swartz, 1998). During the scan, an array of electrodes are placed along the scalp to continuously record voltage fluctuations resulting from ionic current within the neurons (Sheehy, 1984) at a relatively high temporal resolution (from 250Hz up to 20,000Hz). Focal epileptiform abnormalities can be clearly distinguished from background on EEG (Grigg-Damberger and Foldvary-Schaefer, 2012), e.g. interictal discharges (IEDs) show brief (20-200ms) asymptomatic paroxysmal EEG transients while ‘ictal’ discharges (seizures) are sudden focal rhythmic activity with characteristic pattern of evolution (with respect to amplitude, frequency and spatial extent) lasting at least several seconds. A routine EEG of 20-30 minutes is able to capture IEDs in approximately 50% of epileptic patients (Salinsky et al., 1987). Performing repetitive routine EEG sessions or a sleep EEG session can further increase the possibility of observing IEDs to nearly 70% of the patients (Doppelbauer et al., 1993; Liporace et al., 1998). In circumstances when seizures need to be recorded, long-term video-EEG monitoring is conducted (Ghougassian et al., 2004).

EEG plays an important role in epilepsy management. First of all, EEG helps in epilepsy diagnosis and in determining seizure types, and thereby in choosing AED medication and predicting prognosis (Binnie and Stefan, 1999; Smith, 2005). Second, for focal epilepsy, EEG has been confirmed as a useful tool in the localization of the epileptic focus area (Plummer et al., 2008). For example, with a relatively dense array of electrodes (128 channels) mounted over the patient’s head, Michel et al. (2004) correctly localized the epileptogenic zone for more than 90% of their patients (44 in total) with interictal data. Especially, with intracranial EEG (icEEG), electrodes can be placed either on the exposed surface of the brain to record electrical activity from the cerebral

cortex (a technique called “electrocorticography” (ECoG)) (Kuruvilla and Flink, 2003; Lachaux et al., 2003; Miller et al., 2007; Yang et al., 2014), or within the desired brain areas (called stereoelectroencephalography (SEEG)) (Alomar et al., 2016; Bechtereva and Abdullaev, 2000; Gonzalez-Martinez and Lachhwani, 2014; Kratimenos et al., 1993; Thivard et al., 2006), to avoid signal attenuation from extracerebral layers and to improve spatial resolution. Thanks to its high sensitivity and specificity (Blount et al., 2008; Hill et al., 2012), icEEG is currently considered as the “gold standard” for delineating the epileptic focus region (Blount et al., 2008; Zhang et al., 2013; Zumsteg and Wieser, 2000). Furthermore, spatial analysis of EEG signals in the time and frequency domain enables studies into the functional connectivity network in epilepsy (Panzica et al., 2013; Rotondi et al., 2016; Sargolzaei et al., 2015; Wendling et al., 2009). Finally, research has been conducted to assess the possibility of using EEG signals for automatic seizure onset detection or prediction (Ahammad et al., 2014; Minasyan et al., 2010; Mporas et al., 2015; van Mierlo et al., 2014), see Ramgopal et al. (2014) for a recent review.

The limitations of EEG are obvious. Intracranial EEG is invasive, limited in both sampling time and area, and at risk for possible complications such as bleeding or infection (Blount et al., 2008; Zhang et al., 2013). For scalp EEG, its signal is attenuated (sometimes even cancelled) by soft tissues/bone and frequently degraded by muscle artifacts, which decreases its sensitivity in detecting epileptic events (Lieb et al., 1976), especially in identifying the earliest moments of a seizure (Devinsky et al., 1989; Spencer et al., 1985). To generate enough potentials to be detected by a scalp electrode, a large area of the cortex has to be activated synchronously, often of the order of a few square centimeters (Smith, 2005). Moreover, EEG monitoring does not provide information on blood volume and oxygenation which could help evaluate the metabolic impact of seizures or IEDs.

2.2.2 Magnetoencephalography

Magnetoencephalography (MEG) is a functional neuroimaging technique that is able to noninvasively measure the weak magnetic fields associated with intracellular current flow within neurons at a high spatiotemporal resolution (Cohen, 1968; Hämäläinen et al., 1993). Compared with scalp EEG, one of the major advantages of MEG is that its signal is less affected by distortion from the skull and intervening soft tissue (Ray and Bowyer, 2010). The main clinical use of MEG in epilepsy is to detect and localize the source of pathological activity in patients, usually the IEDs

(Albert et al., 2014; Englot et al., 2015; Ray and Bowyer, 2010; Tovar-Spinoza et al., 2008). However, MEG source localization was also reported to be successful for some patients with seizures (Eliashiv et al., 2002; Fujiwara et al., 2012; Tanaka et al., 2004) or on resting-state data (Krishnan et al., 2015). Previous studies involving a relatively large number of patients reported that the accuracy of epileptic focus localization with MEG might potentially be close to that of icEEG, the "gold standard", provided that sufficient IEDs are present in the recording (Lau et al., 2008; Papanicolaou et al., 2005; Stefan et al., 2003; Wu et al., 2006; Zhang et al., 2013). For example, Papanicolaou et al., (2005) performed focus localization on 41 patients (29 with temporal lobe epilepsy and 12 with extratemporal temporal lobe epilepsy) with both MEG and icEEG but did not see statistical difference between the percentages of patients correctly localized with MEG (56%) and icEEG (54%). Recent development of sophisticate algorithms that is able to perform colocalization based on combined MEG-scalp EEG data may further improve its accuracy (Aydin et al., 2015, 2014; Stefan, 2010).

However, MEG often has poor sensitivity in recording paroxysmal activity within the mesial structures of the brain, as magnetic fields associated with medial discharges are likely to decay rapidly (Shigeto et al., 2002). Furthermore, MEG is not suitable for long-term recording, making it challenging to record seizures (although not impossible) (Baumgartner et al., 2000; Knowlton, 2008).

2.2.3 Combined EEG-fMRI

Unlike EEG and MEG, BOLD-fMRI provides indirect measures of neural activity by detecting the hemodynamic changes associated with them (Faro and Mohamed, 2006). BOLD-fMRI works based on the different magnetic properties of the HbR and HbO molecules (i.e. HbR is paramagnetic while HbO is diamagnetic) (Goebel, 2007). According to the neurovascular coupling, increased neural activity triggers a subsequent increase in rCBF (please refer to section 2.1). The increase in rCBF overcompensates the consumption of oxygen and reduces local HbR concentration, leading to an increase of the BOLD signal (activation) (Berman et al., 2006; Cohen and Bookheimer, 1994). Conversely, a decrease in CBF increases local HbR concentration and produces a decreasing BOLD response (deactivation) (Gold and Lauritzen, 2002; Tomasi et al., 2006).

Combined EEG-fMRI enables the observation of BOLD signal changes related to epileptic events at a high spatial resolution (Cunningham et al., 2008; Moeller et al., 2013; van Graan et al., 2015). With a general linear model (GLM) that assumed a canonical HRF, it was shown that EEG-fMRI was able to locate brain regions that correlated with IEDs on 70% to 80% of the patients (Grouiller et al., 2011; Salek-Haddadi et al., 2006). Regarding focus localization, several studies have confirmed the potential of EEG-fMRI (Gotman et al., 2006; Lemieux et al., 2001; Moeller et al., 2009; Pittau et al., 2012a). For example, on some patients, fMRI was able to locate significant BOLD response related to IEDs that was close to the icEEG-defined epileptogenic zone (Vulliemoz et al., 2011). Recently, a localization accuracy of 64% was reported by Pittau et al. (2012a) based on their observations on 33 patients who had IEDs during EEG-fMRI scan.

EEG-fMRI also helps predict surgical outcome in the presurgical evaluation of a patient (An et al., 2013; Coan et al., 2015; Thornton et al., 2010a; van Houdt et al., 2013). Previous work suggested that resecting a brain region that does not include the area presenting significant IED-correlated BOLD signal usually results in a poor surgical outcome, while conducting surgery where the area of maximal BOLD signal change is concordant with resection is more likely to lead to postsurgical seizure-freedom (An et al., 2013; Thornton et al., 2010a).

Using EEG-fMRI to investigate epileptic network is another important application in epilepsy (Gotman, 2008; Kobayashi et al., 2006a; Leite et al., 2013). IED-related studies revealed complex and specific propagation network of the hemodynamic changes associated with focal IEDs (An et al., 2015; Fahoum et al., 2012; Luo et al., 2014; Vulliemoz et al., 2009). Besides, it was also shown that epileptic discharges affect the default mode network, which may explain the reduction in consciousness level and cognitive reserve during epilepsy (Centeno and Carmichael, 2014; Fahoum et al., 2013; Pittau et al., 2012b).

Although less common, EEG-fMRI has also been applied to map seizure-related hemodynamic changes and has yielded promising results, e.g. in focus localization (Sierra-Marcos et al., 2013) and in seizure network study (Moeller et al., 2010), see Chaudhary et al. (2013) for a recent review. However, EEG-fMRI generally has difficulties in recording seizures as they are unpredictable and rarely occur at the exact moment of scanning (Di Bonaventura et al., 2006). The difficulty in recording seizures with fMRI is exacerbated by the fact that small patient movements during a seizure (which is very likely) can have a severely negative effect on data quality (Gotman et al.,

2006; Hajnal et al., 1994), in which case complex artifact removal analysis is required (Donaire et al., 2009; LeVan et al., 2010; Thornton et al., 2010b).

2.2.4 Ictal Single photon emission computed tomography

Single photon emission computed tomography (SPECT) is a technique that is able to provide three-dimensional (3D) imaging of the dynamic changes in rCBF (Groch and Erwin, 2000; Livieratos, 2012). Gamma-emitting radiotracers are first injected into the patient's body through bloodstream, and are irreversibly trapped in the tissue compartment instantly after they cross the blood-brain barrier. Therefore, the distribution of the radiotracers is considered to be proportional to the cerebral perfusion seconds after the tracer injection, and is able to be maintained for a few hours which permits subsequent image acquisition (Fougère et al., 2009; Kim et al., 2011).

Ictal SPECT identifies the epileptic focus region based on the fact that the increase in rCBF from baseline (i.e. the hyperperfusion) is at its maximum at the site of seizure origin (Goffin et al., 2008; Van Paesschen, 2004). Early analysis showed good sensitivity for ictal SPECT localization (> 80%) (Devous et al., 1998; Spanaki et al., 1999). Furthermore, a recent multimodal neuroimaging technique called subtraction ictal SPECT coregistered to MRI (SISCOM) combines the information from ictal SPECT and structural MRI, and shows its advantage in recognizing the extent of epileptogenic zone or discovering potential epileptogenic regions (Brinkmann et al., 2000; Lee et al., 2011; Newey et al., 2013; O'Brien et al., 2004, 1998; So, 2000). Concordant localization results with SISCOM and with other localization modalities might indicate favorable postsurgical outcome (Ahnlide et al., 2007; Kudr et al., 2013; von Oertzen et al., 2011).

Compared with the high sensitivity, the localization specificity of ictal SPECT is lower (~70%), especially with extratemporal lobe epilepsies (Newton et al., 1995; Weil et al., 2001). In a SPECT scan, the time for the radiotracers to be injected, to travel to the brain, and to be fixed in the brain tissue normally takes more than 40 seconds (Van Paesschen, 2004). Therefore, ictal SPECT can rarely discriminate between the seizure onset zone and areas receiving propagated activity (Fougère et al., 2009; Paesschen et al., 2003). Ictal SPECT is now used more along with other imaging modalities (e.g. icEEG) to assist in the formulation of an epileptogenic zone localization, rather than being used to determine a resection directly (Duncan et al., 2016; Lascano et al., 2016).

2.2.5 18F-fluorodeoxyglucose positron emission tomography

Positron emission tomography (PET) is similar to SPECT in terms of its use of radioactive tracers and detection of gamma rays (Bailey et al., 2005; Livieratos, 2012), but has a relatively higher spatial resolution and better signal contrast (Kim et al., 2011; Spencer, 1994). The 18F-fluorodeoxyglucose, an analogue of glucose, is often selected as the radiotracer (FDG-PET). Therefore, the distribution of FDG in the brain tissue reflects cerebral metabolism (Fougère et al., 2009; Lee et al., 2001), which is also an indirect measure of neural activity. However, in epilepsy, FDG-PET is normally applied in the interictal period due to a long tracer uptake time (>30 min), which is significantly longer than averaged seizure duration (Kim et al., 2011; Sager et al., 2011).

The basis of FDG-PET in focus localization is that epileptogenic zone of focal epilepsies usually shows interictal hypometabolism (Engel, 1988; Savic et al., 1997). FDG-PET was reported to be most sensitive in localizing the epileptic focus for temporal lobe epilepsies (Fougère et al., 2009; Rathore et al., 2014; Spencer, 1994), with its sensitivity comparable to ictal SPECT (>80%) (Drzezga et al., 1999; Gok et al., 2013; Kim et al., 2011; Won et al., 1999). Moreover, FDG-PET helps select good surgical candidates. Patients showing unilateral temporal hypometabolism ipsilateral to the EEG foci normally have a higher possibility of achieving postsurgical seizure freedom (Kim et al., 2011; Willmann et al., 2007).

FDG-PET suffers from low localization specificity. Sites showing cerebral hypometabolism might distribute much wider than the actual epileptogenic zone (Duncan et al., 2016), making it difficult to decide the precise extent of the area to be resected if only an FDG-PET image is presented (Sarikaya, 2015). Besides, FDG-PET is a single snapshot that lacks temporal information, which is a disadvantage shared with SPECT.

2.2.6 Combined EEG-fNIRS

Except for EEG, none of the techniques reviewed above is suitable for long-term recording for several reasons including cost, availability, safety and portability, which may be addressable by fNIRS. In past decades, different groups have assessed the clinical potential of EEG-fNIRS as an auxiliary method of epilepsy diagnosis (Adelson et al., 1999; Arca Diaz et al., 2006; Buchheim et al., 2004; Cooper et al., 2011; Haginoya et al., 2013, 2002; Jeppesen et al., 2015; Munakata et al., 2004; Pellegrino et al., 2016; Rizki et al., 2015; Roche-Labarbe et al., 2008; Seyal, 2014; Shuhaiber

et al., 2004; Singh et al., 2014; Slone et al., 2012; Sokol et al., 2000; Sokoloff et al., 2015; Steinhoff et al., 1996; Villringer et al., 1994; Vinette et al., 2015; Wallois et al., 2009; Watanabe et al., 2002, 2000; Yücel et al., 2014a), summarized in Table 2.1. In these works, the hemodynamic effects of epileptic events (mostly seizures) were preliminarily investigated in adults, children and neonates. Early studies revealed heterogeneous patterns of oxygenation changes that might be specific to seizure types (Adelson et al., 1999; Haginoya et al., 2002; Sokol et al., 2000; Steinhoff et al., 1996; Villringer et al., 1994). For example, Villringer et al. reported cerebral blood volume increases concordant with seizure origin in three patients with presumed extratemporal epilepsy (Villringer et al., 1994), while a reproducible deoxygenation was also observed over the frontal lobe by Steinhoff et al. on two patients with mesial temporal lobe epilepsy (Steinhoff et al., 1996). Sokol et al. studied 8 patients with drug refractory temporal epilepsy using fNIRS and showed distinct patterns of cerebral oxygenation for complex partial seizures and for rapidly secondarily generalized complex partial seizures (Sokol et al., 2000). Haginoya et al. studied various types of pediatric epileptic seizures with fNIRS in 15 children and reported heterogeneous CBV changes depending on seizure types (convulsions, absence, tonic status epilepticus, and infantile spasms) (Haginoya et al., 2002). These initial observations suggested the utility of fNIRS in epilepsy research but did not make direct progress towards evaluating its preclinical value for focus lateralization or localization because of the limited number of subjects, the use of a single fNIRS channel (frequently affixed to the hairless skin overlying the frontal cortex to avoid hair contamination) distant from the seizure focus, heterogeneity in seizure types, and/or lack of clear confirmation of the epileptogenic zone. One pioneer fNIRS study on focus lateralization was carried out by Watanabe et al. in 2002, where they performed bihemispheric sampling of brain hemodynamics and correctly lateralized the focus for 28 of the 29 patients (Watanabe et al., 2002). Their recent work on mesial temporal lobe epilepsy presented four successful focus lateralization cases when using HbO changes as the index (Rizki et al., 2015). However, the behavior of other chromophores was not discussed and information on remote changes was not elaborated.

Table 2.1 Summary of the literature on EEG-fNIRS in human epilepsy (Other groups)

Work	Number of patients	Number of channels	Epilepsy type and event	Major contributions
Villringer et al. (1994)	3	1	Focal seizure (extratemporal)	Increases in blood volume and HbO concentration were found over the presumed epileptic focus region.
Steinhoff et al. (1996)	2	1	Focal seizure (temporal)	Reproducible cerebral deoxygenation was detected in the ipsilateral frontal cortex.
Adelson et al. (1999)	3	1	Focal seizure (foci not specified)	A perfusion-metabolism mismatch was observed during seizures.
Sokol et al. (2000)	8	1	Focal seizure (temporal)	Complex partial seizures and rapidly secondarily generalized complex partial seizures showed distinct pattern of cerebral oxygenation.
Watanabe et al. (2000)	12	8-24	Focal seizure (10 temporal, 2 parietal)	In all 12 cases, rCBV increased rapidly on the focus side after partial seizure onsets.
Haginoya et al. (2002)	15	1	Cryptogenic or symptomatic, generalized or focal, seizure	Heterogeneous CBV changes were reported depending on seizure types.
Watanabe et al. (2002)	29	8-24	Focal seizure (25 temporal, 2 frontal, 2 parietal)	Significant hyper-perfusion on the side of seizure foci was observed in 96% of cases (28/29).
Buchheim et al. (2004)	3	1	Generalized seizure (absence)	Absence seizures were associated with a decrease in HbO and an increase in HbR over the frontal cortex.
Munakata et al. (2004)	3	24	Generalized seizure (West syndrome)	An increase in rCBV occurred in multiple areas during clusters of spasms.

Table 2.1 (Continued) Summary of the literature on EEG-fNIRS in human epilepsy (Other groups)

Work	Number of patients	Number of channels	Epilepsy type and event	Major contributions
Shuhaiber et al. (2004)	1	2	Focal seizure (frontal)	Seizures produced a progressive decline and wide fluctuations in regional oxygen saturation (rSO_2) on the side ipsilateral to the focus.
Arca Diaz et al. (2006)	1	2	Focal seizure (frontal)	Fluctuations in rSO_2 were observed in bilateral frontal regions during concurrent seizures.
Roche-Labarbe et al. (2008)	6	1	Generalized seizure	Generalized spike-and-wave discharges were related to complex oxygenation changes in frontal areas.
Wallois et al. (2009)	1	2	Focal seizure (temporal, neonatal seizures)	Seizure-like discharges induced increases first in HbR, then in HbO and HbT. An undershoot was seen only for HbR.
Cooper et al. (2011)	4	Up to 60	Generalized seizure (neonatal seizures)	Transient hemodynamic events identified were associated first with an increase followed by a rapid decrease of HbO concentration.
Slone et al. (2012)	5	2	Focal seizure (temporal)	A decrease in HbO, HbT and oxygen saturation (SO_2) were observed in the frontal lobe up to 15 min before the seizure onset.
Sato et al. (2013)	1	48	Focal seizure (frontal)	Increased cerebral blood flow was seen in the seizure onset zone after the onset of a supplementary motor area seizure, with rapid propagation to adjacent areas.
Seyal (2014)	6	1	Focal seizure (temporal)	Preictal SO_2 increase was observed in the frontal lobe, followed by periictal SO_2 decrease and postictal increase.

Table 2.1 (Continued) Summary of the literature on EEG-fNIRS in human epilepsy (Other groups)

Work	Number of patients	Number of channels	Epilepsy type and event	Major contributions
Singh et al. (2014)	1	58	Neonatal seizures	High amplitude HbO, HbR and HbT increased prior to extended decreases were seen to be associated with all seven electrographic neonatal seizures.
Yücel et al. (2014a)	2	6-7	Focal seizure	An increase in HbO, HbT, blood flow and metabolic rate of oxygen ($CMRO_2$) was located over the epileptic focus region during seizures. A subsequent deoxygenation phase was also seen for one seizure.
Jeppesen et al. (2015)	15	2	Focal seizure (10 temporal, 3 frontal, 1 parietal, 1 unspecified)	NIRS-measured hemoglobin concentration changes in the frontal lobe during seizures may not be suitable as biomarkers for seizure detection.
Rizki et al. (2015)	4	44	Focal seizure (mesial temporal)	EEG-fNIRS captured HbO increases during seizures in mesial temporal lobe epilepsy, which could be used to lateralize the epileptic focus side.
Sokoloff et al. (2015)	11	2	Neonatal seizures	Neonatal seizures were associated with reduced rSO_2 on both hemispheres.
Vinette et al. (2015)	4	2	Focal seizure (3 temporal, 1 central)	Slowly varying changes in hemodynamics might precede epileptic seizures.
Pellegrino et al. (2016)	9	Up to 8 emitters and 16 detectors	Focal IED (3 frontal, 3 temporal, 2 occipital, 1 parieto-occipital)	An HbO response to IEDs was observed over the presumed focus region for 8 patients. The response was long-lasting, often bilateral and patient-specific in its shape.

Table 2.2 Summary of the results of our group using EEG-fNIRS in human epilepsy

Work	Number of patients	Number of channels	Epilepsy type and event	Major contributions
Nguyen et al. (2012)	3	95-120	Focal seizure (temporal)	An initial HbO increase with an HbR decrease was first observed in the focus area. Long complex partial seizures were associated with a subsequent HbR increase while HbO continued to increase or even decreased. Similar hemodynamic profile was seen over the region contralateral to the focus area.
Nguyen et al. (2013)	9	44-203	Focal seizure (frontal)	Over the seizure focus, an initial concentration increase for HbO and HbT from baseline to peak was noted, followed by a gradual decline to a plateau or to the baseline. The behavior of HbR concentration was heterogeneous. Similar changes in HbO, HbR and HbT were seen in homologous contralateral region, albeit of lower amplitudes.
Pouliot et al. (2014)	9 (3 had seizures)	47-173	Focal seizure and IED (2 occipital, 1 parieto-occipital)	An HbR decrease associated with seizures was located in the focus region for 2/3 patients. For IEDs, an HbR decrease consistent with the focus region was seen on 6/7 patients.
Machado et al. (2011)	1	43	Focal IED (frontal)	EEG-fNIRS showed an increase of CBV (HbO↑, HbR↓, HbT↑) spatially concordant with the presumed epileptic focus.
Pouliot et al. (2012)	3	100-150	Focal IED (1 left fronto-centro-temporal, 1 right frontal, 1 left parieto-occipital)	The hemodynamic response to IEDs contained significant second order inhibitive component in the case of numerous IEDs taking place in rapid succession.

In the past few years, the feasibility of applying an optical imaging technique in the study of the hemodynamic response to neonatal seizures has been explored by different groups (Cooper et al., 2011; Singh et al., 2014; Sokoloff et al., 2015; Wallois et al., 2009), see also Wallois et al. (2010) for a review of early discoveries. Their recent results showed that the shape of the hemodynamic changes associated with neonate seizures might be distinct from the standard responses to functional stimulations on older children or adults. Since reading neonatal EEG can be extremely challenging, and performing SPECT, PET or fMRI on neonates is usually not possible due to ethical and technical restrictions (Wallois et al., 2009), their studies are remarkable in showing the potential of fNIRS for monitoring in neonatal intensive care units.

Another particular interest of recent fNIRS work was in the observation of oxygenation variations preceding the EEG onsets of epileptic seizures. With EEG-fNIRS, two different groups observed preictal oxygenation changes over the frontal lobe prior to temporal lobe seizures (Seyal, 2014; Slone et al., 2012). Although a subsequent attempt of using fNIRS-measured hemoglobin concentration changes as biomarkers for seizure detection was unsuccessful (Jeppesen et al., 2015), this endeavor suggests a potential for fNIRS as a home monitoring seizure detection or prediction device.

Some other studies focused on the application of recent fNIRS methodological improvements to epilepsy. For example, aiming at removing the movement artifact from clinical fNIRS recordings, Yücel and colleagues proposed to use collodion-fixed prism-based optical fibers which were eventually proven to be helpful in recovering the hemodynamic response to three epileptic seizures in their study (Yücel et al., 2014a). Serving the same purpose, data-based filtering techniques were also adapted into the analysis of long term fNIRS data (Vinette et al., 2015). In addition, efforts have been made by Machado et al. to provide an optimal fNIRS emitter/detector montage in IED studies to maximize sampling sensitivity over one or several brain regions (Machado et al., 2014). The personalized montage was used in their follow-up study of IEDs on 9 patients, in which an HbO response with a patient-specific shape was located over the epileptic focus region and sometimes over the unaffected contralateral area as well (Pellegrino et al., 2016).

In summary, preliminary work of other groups confirms the clinical potential and usefulness of fNIRS: 1) it was seen as a robust tool to explore hemodynamics associated with seizures on adults, children and neonates; 2) studies of seizures indicated a potential for epileptic focus localization;

3) it can possibly be used to study preictal hemodynamic changes; 4) fNIRS hardware and software have steadily improved over the last few years and will most likely continue to improve, which may in turn benefit future clinical studies.

Our group has been trying to complement the current research paradigm by recording from more channels (typically 100-150) to reconstruct 2-dimensional (2D) topographic images of activations with much larger brain coverage. The relatively large number of channels ascertained complex local and remote oxygenation changes associated with focal seizures in a fair number of patients. Our work on temporal lobe seizures (Nguyen et al., 2012), frontal lobe seizures (Nguyen et al., 2013) and posterior seizures (Pouliot et al., 2014) confirms that continuous EEG-fNIRS can indeed detect hemodynamic changes during focal seizures. In most cases, we observed an increase in HbO but more heterogeneous behavior of HbR (usually decreased, sometimes unchanged or even increased) over the epileptic focus region. These changes can last much longer than the EEG evidence of seizure activity. In addition, early complex hemodynamic changes outside the focus were frequently observed, notably in contralateral homologous areas but also in more remote regions as seizures evolve. In summary, the hemodynamic changes associated with epileptic seizures are more complex than previously thought, and can sometimes complicate the focus localization process.

On the other hand, our group also published the first studies that showed a clinical potential of EEG-fNIRS in studying the hemodynamic response to focal IEDs (Machado et al., 2011; Pouliot et al., 2014). For example, on a 10 year-old boy with right frontal lobe epilepsy, Machado et al. (2011) observed a significant HbO increase and an HbR decrease temporally synchronized with IEDs and spatially concordant with the presumed epileptic focus region. With careful modeling, (Pouliot et al., 2012) also showed that the hemodynamic response is associated with significant inhibitive nonlinearities when numerous IEDs take place in rapid succession, and that modeling this nonlinear contribution helped to obtain the concordant localization of the epileptic focus with fMRI for some patients (Pouliot et al., 2012). However, due to the limited number of patients involved in these studies, the overall sensitivity and the specificity of using the fNIRS-measured hemodynamic response to IEDs in activation detection and in focus localization were not estimated.

CHAPTER 3 THEORY AND METHODOLOGY

This chapter first gives a brief introduction of the theory of light propagation in diffused media. The rest of this chapter covers the hardware setup as well as the data analysis pipeline that were used in the two IED-related studies presented in chapter 4 and chapter 5.

3.1 Brief introduction of diffuse optical imaging basics

3.1.1 Forward modeling and inverse problem

Photon transport in biological tissue can be equivalently simulated numerically with Monte Carlo method, or analytically modeled with the radiative transport equation (RTE) as follows (Durduran et al., 2010; Wang and Wu, 2007):

$$\frac{1}{v}\frac{\partial L(\vec{r},\hat{s},t)}{\partial t} = -\hat{s}\cdot\nabla L(\vec{r},\hat{s},t) - \mu_t L(\vec{r},\hat{s},t) + S(\vec{r},\hat{s},t) + \mu_s \int_0^{4\pi} L(\vec{r},\hat{s}',t) f(\hat{s},\hat{s}') d\hat{s}' \qquad (3.1)$$

The RTE is a differential equation describing the changes in the light radiance, $L(\vec{r},\hat{s}',t)$ which is defined as the light power per unit area along the $\hat{s}$ direction at the distance $\vec{r}$ and time t. The first two terms in the right hand side of the RTE, $-\hat{s}\cdot\nabla L(\vec{r},\hat{s},t)$ and $-\mu_t L(\vec{r},\hat{s},t)$, represent the loss in light radiance due to beam divergence and light extinction (i.e. absorption and scattering), while the last two terms describe the energy incident from the light source S and from light scattering from any direction $\hat{s}'$ into the direction $\hat{s}$. In the RTE, v is the speed of light in the medium; μ_s is the scattering coefficient; $\mu_t = \mu_s + \mu_a$ where μ_a is the absorption coefficient; $f(\hat{s},\hat{s}')$ is a probability density function that represents the likelihood of light scattering from the direction $\hat{s}'$ into $\hat{s}$. The scattering coefficient μ_s and the scattering coefficient μ_a are respectively the reciprocals of the photon scattering length and the photon absorption length, which are defined as the typical distances traveled by a photon before it is scattered or absorbed. Both the scattering coefficient and the absorption coefficient are dependent on the wavelength of the light.

Unfortunately, the RTE is quite complex and is difficult to solve (Rutily and Chevallier, 2006). In brain imaging, the RTE is often simplified into the diffusion equation (DE) for the photon fluence rate, $\Phi(\vec{r},t)$, by assuming that brain tissue is highly diffusive, i.e. $\mu_s \gg \mu_a$ (Boas et al., 2004b). The DE is less accurate compared with Monte-Carlo methods or the RTE, but is more efficient in computation:

$$vS(\vec{r},t) + \nabla \cdot D(\vec{r})\nabla\Phi(\vec{r},t) - v\mu_a(\vec{r})\Phi(\vec{r},t) = \frac{\partial\Phi(\vec{r},t)}{\partial t} \quad (3.2)$$

where D is the photon diffusion coefficient $D = \frac{v}{3(\mu_a+\mu_s')} \approx \frac{v}{3\mu_s'}$; $\mu_a(\vec{r})$ and $\mu_s'(\vec{r})$ are the position dependent absorption coefficient and reduced scattering coefficient. In diffuse optical imaging, the tissue is usually considered to be homogeneous, thus we have $\mu_a(\vec{r}) = \mu_a, \mu_s'(\vec{r}) = \mu_s'$. Note that μ_s' differs from μ_s as μ_s' incorporates μ_s and the anisotropy factor g, i.e. $\mu_s' = (1-g)\mu_s$ where $g = <\cos(\theta)>$ is the averaged cosine of the scattering angle θ for a single scattering event. This is because that light tends to scatter predominantly in the forward direction. Therefore, the typical distance traveled by a photon before its direction is randomized by scattering events is longer than the photon scattering length (thus $\mu_s' < \mu_s$, "reduced"). In summary, the DE explains the temporal changes in photon concentration in a unit volume (the right hand side) as the contribution from the source (the first term on the left hand side) plus the photons scattered into the volume (the second term) minus the photon loss due to absorption within the volume (the third term) (Buckley, 2011).

The DE needs be solved to find the absorption and scattering properties of the tissue. This is known as the inverse problem, which is often ill-posed in real practice (Gibson et al., 2005). The reader is referred to other materials (e.g. Buckley (2011); Durduran et al. (2010); Wang and Wu (2007)) for a discussion of its theoretical solution under different boundary conditions, as such discussion is out of the scope of this thesis. In the context of NIRS, the main absorber of near infrared light is hemoglobin (HbO and HbR). Therefore, by using two or more wavelengths within the near infrared range (650nm to 950nm, e.g. λ_1 and λ_2), the absorption coefficient of each wavelength (μ_a) can be related to the HbO concentration, C_{HbO}, and HbR concentration, C_{HbR}, with the following extinction equations:

$$\begin{cases} \mu_a(\lambda_1) = \varepsilon_{HbO}^{\lambda_1} C_{HbO} + \varepsilon_{HbR}^{\lambda_1} C_{HbR} \\ \mu_a(\lambda_2) = \varepsilon_{HbO}^{\lambda_2} C_{HbO} + \varepsilon_{HbR}^{\lambda_2} C_{HbR} \end{cases} \quad (3.3a)$$

where ε is the extinction coefficient dependent on the type of hemoglobin and the wavelength of the near infrared light. The extinction coefficients of HbO and HbR corresponding to different light wavelengths have been measured *in vitro* and are available online (Prahl, 1998).

3.1.2 The differential pathlength approach

Equation 3.3a also holds for relative values of hemoglobin concentration (ΔC_{HbO} and ΔC_{HbR}) and absorption coefficients ($\Delta\mu_a$), i.e.

$$\begin{cases}\Delta\mu_a(\lambda_1) = \varepsilon_{HbO}^{\lambda_1}\Delta C_{HbO} + \varepsilon_{HbR}^{\lambda_1}\Delta C_{HbR} \\ \Delta\mu_a(\lambda_2) = \varepsilon_{HbO}^{\lambda_2}\Delta C_{HbO} + \varepsilon_{HbR}^{\lambda_2}\Delta C_{HbR}\end{cases} \tag{3.3b}$$

Therefore, if we are only interested in the temporal concentration changes of hemoglobin (rather than absolute values), we simply need to find the relative changes in absorption coefficients from the NIRS recordings. In this case, a much simpler differential pathlength approach can be applied using only the variations in the optical density (OD) of the detected light:

$$\Delta OD(\lambda, d, t) = -\ln\left(\frac{\Phi(\lambda,d,t)}{\Phi_0(\lambda,d)}\right) \tag{3.4}$$

where d is the distance of the NIRS source and detector (SD) separation; Φ is the detected photon fluence at time t; Φ_0 is the detected photon fluence during baseline. Three hypotheses are required here. First, the relative changes in absorption coefficients are much smaller than their baseline values, i.e. $\Delta\mu_a \ll \mu_{a0}$. Second, the absorption change is homogeneous along the light pathway within the tissue. Finally, the scattering change is negligible, i.e. $\Delta\mu_s' \approx 0$. Under these hypotheses, the Taylor series can be used to expand the OD when a small change in absorption is present, for a certain wavelength of light and a certain SD separation (Durduran et al., 2010):

$$OD(\mu_{a0} + \Delta\mu_a, \mu_{s0}' + \Delta\mu_s') \approx OD(\mu_{a0} + \Delta\mu_a, \mu_{s0}') \approx OD(\mu_{a0}, \mu_{s0}') + \frac{\partial OD(\mu_{a0},\mu_{s0}')}{\partial\mu_a}\Delta\mu_a \tag{3.5}$$

Therefore, we have

$$\begin{aligned}\Delta OD(\lambda, d, t) &= OD(\mu_{a0} + \Delta\mu_a, \mu_{s0}' + \Delta\mu_s', \lambda, d, t) - OD(\mu_{a0}, \mu_{s0}', \lambda, d) \\ &\approx \frac{\partial OD(\mu_{a0}, \mu_{s0}', \lambda, d)}{\partial\mu_a}\Delta\mu_a(\lambda, t) = d_a(\lambda, d)\Delta\mu_a(\lambda, t) \approx d \cdot DPF(\lambda) \cdot \Delta\mu_a(\lambda, t)\end{aligned} \tag{3.6}$$

The last step in equation 3.6 employs the modified Beer-Lambert Law (MBLL), which is an approximation that is currently widely applied in optical brain imaging (Delpy et al., 1988; Desjardins et al., 2012; Kocsis et al., 2006). $d_a(\lambda, d) \equiv \frac{\partial OD(\mu_{a0},\mu_{s0}',\lambda,d)}{\partial\mu_a}$ is called the differential absorption pathlength. With the MBLL, $d_a(\lambda, d)$ is expressed as the multiplication of the SD

distance d and a differential pathlength factor (DPF) to account for the additional path travelled by the photons in the medium due to scattering events. The DPF is dependent on the light wavelength, and can be measured with additional instruments or computed with Monte Carlo simulations (Bonnéry et al., 2012; Chatterjee et al., 2015; Duncan et al., 1996).

Note that equation 3.6 assumes the distribution of the small absorption change to be spatially uniform in the medium. However, if the change in light absorption is rather localized, equation 3.6 leads to systemic underestimates for $\Delta\mu_a$ (and thus for the hemoglobin concentration change as well). This is defined as the partial volume effect in optical imaging. In this case, the DPF in equation 3.6 must be replaced with a corrected partial pathlength factor (PPF) that incorporates both the differential pathlength and the partial volume (Steinbrink et al., 2001; Strangman et al., 2003):

$$PPF(\lambda) = \frac{DPF(\lambda)}{PVF(\lambda)} \tag{3.7}$$

where $PVF(\lambda)$ is a wavelength-dependent partial volume factor (PVF). In the field of brain imaging with focal activations, a PVF of 40-60 is often applied (Boas et al., 2001; Strangman et al., 2003).

Combining Equations 3.3b, 3.4, 3.6 and 3.7, we obtain the explicit form to derive hemoglobin concentration changes from detected OD variations:

$$\Delta OD(\lambda, d, t) = -\ln\left(\frac{\Phi(\lambda,d,t)}{\Phi_0(\lambda,d)}\right) = d \cdot PPF(\lambda) \cdot (\varepsilon^{\lambda}_{HbO}\Delta C_{HbO} + \varepsilon^{\lambda}_{HbR}\Delta C_{HbR}) \tag{3.8}$$

3.2 Multichannel EEG-fNIRS recording methods

In the section above, we briefly review the theory relating light propagation properties to hemoglobin concentration when a single SD channel is used. However, in our recordings on epileptic patients, we employed more channels (typically 100 to 150) to reconstruct 2D topographic images of brain activations. This brings additional instrumental and methodological challenges which are introduced respectively in the following subsections.

3.2.1 System setup and recording protocol

In the two studies presented below (chapter 4 & chapter 5), we used a home-modified commercial fNIRS imaging system (ISS Imagent, Champaign, IL., USA). Helmets of different sizes were

designed to ensure a best-fit to a patient's head. Recording hardware included 19 carbon EEG electrodes, 64 fibre sources and 16 fiber detectors mounted on the helmets. A detector was placed 3 to 5 cm away from several adjacent sources, forming multiple optical Source-Detector (SD) channels (Figure 3.1A). Optode positions were then co-registered onto a 3D high-resolution anatomical MRI (obtained prior to EEG-fNIRS) using BrainSight^{TM} (Rogue Research, Montreal, Canada) (Figure 3.1B). 3D coordinates of a SD channel were considered as the midpoint of its source and detector. In our studies, channel positions were intentionally arranged so that the covered area included the whole lobe with the pre-acknowledged epileptic focus, the corresponding contralateral lobe, and as much area from the other lobes as possible, especially on the suspected focus side. Two wavelengths on each side of the 800nm hemoglobin isosbestic point (i.e. the wavelength at which the absorption rates of HbR and HbO are equal) were used: 690 nm which is more sensitive to HbR and 830 nm which is more sensitive to HbO. Optical intensity information is collected by an ISS oximeter at 19.5Hz.

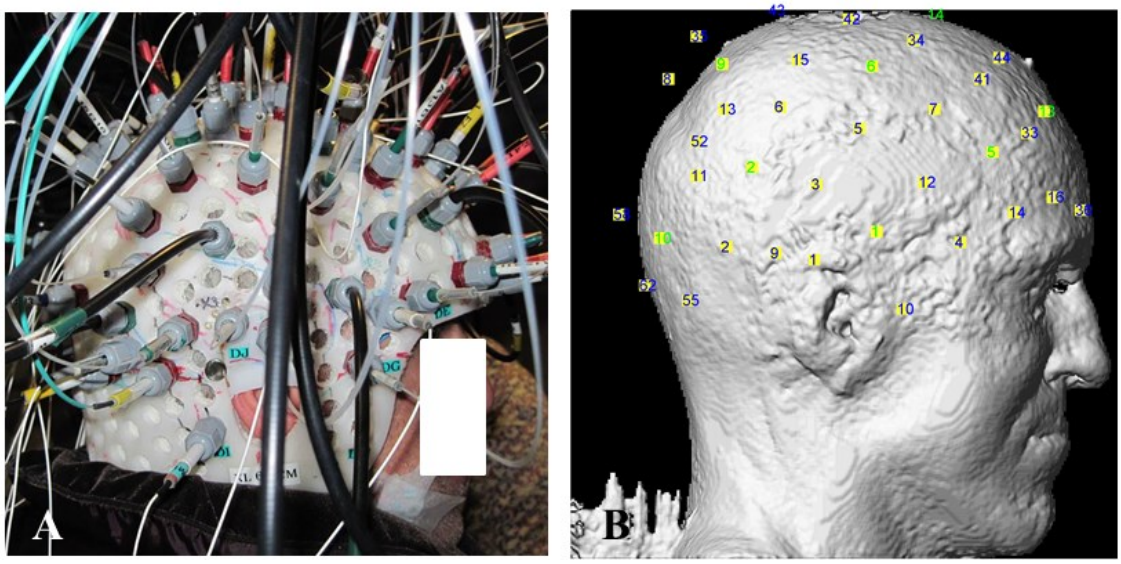

Figure 3.1: (A) Example of helmet configuration in one simultaneous EEG-fNIRS recording on an epileptic patient (B) Co-registered optode distribution projected onto the scalp: sources/detectors are marked in blue/green respectively.

EEG data were recorded at a sampling rate of 500 Hz using a Neuroscan Synamps 2TM system (Compumedics, Charlotte, NC., USA), and were then band-pass filtered between 0.1 Hz and 100 Hz to remove instrumental noise and other artificial disturbances. The electrocardiogram (EKG) of the patient was also plotted.

After installation of the helmet, multiple sessions (typically 15 min each) of simultaneous EEG-fNIRS recording were performed for each patient. During recordings, the patient was simply asked to sit comfortably and relax in a dark room. After the acquisition, the EEG data of the patient were reviewed offline by certified clinical neurophysiologists. Seizure-onset and seizure-offset times, defined respectively as the earliest and latest clinical or electrographic evidence of seizure activity, were marked directly on the EEG along with IEDs using Analyzer 2.0 (Brain Products, Gilching, Germany). Physiological data (e.g. the heartbeats) were also marked on the EKG and are semi-automatically filtered.

3.2.2 Data processing and statistical analysis

The data processing was carried out with our in-house Matlab (MathWorks, USA) toolbox, namely nirs10, which is based on statistical parametric mapping 8 (SPM8) (Friston et al., 2007) and NIRS-SPM (Jang et al., 2009; Ye et al., 2009).

For each patient, the anatomical MRI image was segmented to obtain a grey matter layer, from which four 2D cortical projections (frontal, dorsal, right and left) were extracted. The positions of fNIRS optodes on the standard SPM8 anatomical atlas were then mapped back to these topographical projections of the patient's grey matter layer.

The optical data of each SD channel were first transferred into hemoglobin concentration changes using the MBLL (equation 3.8). The DPFs for the two near infrared wavelengths (690nm & 830nm) were calculated based on the empirical law derived by Duncan et al. (1996). However, the age factor was not considered in our computation of the DPF, due to a recent study from our group in which they confirmed that the difference in DPF between young and old adults was not statistically significant (Bonnéry et al., 2012). A PVF of 50 was used in the first two studies of this thesis (reported in chapter 4 and chapter 5). The extinction coefficients of HbO and HbR corresponding to the near infrared light of 690nm and 850nm were referred from Prahl (1998). Relative changes in HbT concentration were obtained by adding together HbO and HbR concentration changes (i.e. $\Delta C_{HbT} = \Delta C_{HbO} + \Delta C_{HbR}$).

After converting optical data into hemoglobin concentration changes, a first challenge was to interpret these changes, i.e. to separate the hemodynamic response to epileptic events from noise and other systemic physiological signals (e.g. heartbeats, respiration or Mayer wave). In our study,

this was addressed by employing a general linear model (GLM) which decomposes the detected hemoglobin concentration change into a linear combination of the expected hemodynamic response to epileptic or physiological events plus an error term:

$$\boldsymbol{Y} = [X_1\ X_2\ \ldots X_P] \times [\beta_1\ \beta_2\ \ldots\ \beta_P]^T + \boldsymbol{\epsilon} = \boldsymbol{X\beta} + \boldsymbol{\epsilon} \tag{3.9}$$

$\boldsymbol{Y}$ is an M by N matrix where each column contains the M points of the recorded hemoglobin concentration change time course of one channel (thus N channels in total); X_p is an M by 1 regressor vector denoting the expected hemoglobin concentration response to a certain of event (epileptic or physiological, P regressors in total); β_p is an N by 1 vector of regression coefficients corresponding to X_p; $\boldsymbol{\epsilon}$ is an M by N noise term. The GLM is considered as a standard analysis method in the detection of brain activation with BOLD-fMRI (Friston et al., 2007; Monti, 2011; Worsley and Friston, 1995), and has been adapted to fNIRS studies (Koh et al., 2007; Plichta et al., 2007; Schroeter et al., 2004; Ye et al., 2009) thanks to the similar physiological basis as well as the comparable experimental designs between fMRI and fNIRS. In our GLM for one session of recording, we included a regressor for each type of epileptic event marked in our EEG traces (i.e. seizures and/or different types of IEDs, e.g. left temporal lobe IED and right temporal lobe IED for a patient with bilateral temporal lobe epilepsy), a heartbeat rate regressor derived from our EKG recordings and a constant regressor. For each type of epileptic event, the expected hemoglobin concentration response (i.e. the regressor) was formulated by convolving the time and duration of the events (also marked on EEG data) u with a basis function, normally an HRF:

$$X_p = \int_{-\infty}^{+\infty} h(\delta)u(t-\delta)d\delta \tag{3.10}$$

where h is the selected HRF.

For all channels, the estimated regression coefficients $\widehat{\boldsymbol{\beta}}$ and the error covariance matrix $\boldsymbol{C}$ were derived from the GLM (equation 3,9) with least squares estimation (Ye et al., 2009):

$$\widehat{\boldsymbol{\beta}} = (\boldsymbol{X}^T\boldsymbol{X})^{-1}\boldsymbol{X}^T\boldsymbol{Y} \tag{3.11}$$

$$\boldsymbol{C} = \boldsymbol{\Sigma}\otimes\{(\boldsymbol{X}^T\boldsymbol{X})^{-1}\boldsymbol{X}^T\boldsymbol{V}((\boldsymbol{X}^T\boldsymbol{X})^{-1}\boldsymbol{X}^T)^T\}_{P\times P} \equiv \boldsymbol{\Sigma}\otimes\boldsymbol{C}_\beta \tag{3.12}$$

where $\boldsymbol{V}$ is the temporal autocorrelation in the recorded hemoglobin data $\boldsymbol{Y}$; $\otimes$ denotes the Kronecker product; $\boldsymbol{\Sigma}$ is the common error variance matrix of all channels (N by N) as follows:

$$\boldsymbol{\Sigma} = \begin{bmatrix} \sigma_1^2 & 0 & \cdots & 0 \\ 0 & \sigma_2^2 & \cdots & 0 \\ \vdots & \vdots & \ddots & \vdots \\ 0 & 0 & 0 & \sigma_N^2 \end{bmatrix} \tag{3.13}$$

Suppose that the p_0th regressor X_{p_0} is from an event of interest, the next step is to conduct a hypothesis test for the corresponding coefficient β_{p_0} to test whether X_{p_0} can explain the variance in $\boldsymbol{Y}$ at a stastically significant level. However, in order to reconstruct 2D topographic maps of brain activations, such statistical test needs to be performed at pixel-level of the four 2D cortical projections (rather than at the channel level), which thus requires spatial interpolation of the channel-wise regression coefficients $\widehat{\boldsymbol{\beta}}$ and the error covariance matrix $\boldsymbol{C}$. A central difficulty here is that the sparse and irregular spatial distribution of fNIRS recordings (unlike the dense measurements from fMRI) breaks the basic assumption of homogeneous Gaussian random field model in the conventional spatial analysis of functional signals. This problem has been addressed in Ye et al. (2009) by proposing an inhomogeneous interpolation kernel $\boldsymbol{K}$, and analyzing the interpolated fNIRS statistics with the inhomogeneous Gaussian random field theory. By incorporating their contributions, we were able to conduct a t-statistical test on the interpolated regression coefficient at every pixel b, $\hat{\beta}_{p_0} K_b$, of each of the four 2D projections, testing the null hypothesis that the interpolated hemoglobin concentration change at the pixel b is not correlated with the expected hemodynamic response to the p_0th event, i.e. $\hat{\beta}_{p_0} K_b = 0$, with the following t-statistic and effective degrees of freedom (EDoF) (Ye et al., 2009):

$$t_{p_0,b} = \frac{\hat{\beta}_{p_0} K_b}{\sqrt{\Sigma_b C_{p_0}}} \tag{3.14}$$

$$EDoF = \frac{\mathrm{tr}(\boldsymbol{RV})^2}{\mathrm{tr}(\boldsymbol{RVRV})} \tag{3.15}$$

where Σ_b is the element in $\boldsymbol{K}^T \boldsymbol{\Sigma} \boldsymbol{K}$ corresponding to the pixel b; C_{p_0} is the p_0th element in the diagonal of $\boldsymbol{C}_\beta$ in the equation 3.12, $\boldsymbol{C}_\beta = (\boldsymbol{X}^T\boldsymbol{X})^{-1}\boldsymbol{X}^T V((\boldsymbol{X}^T\boldsymbol{X})^{-1}\boldsymbol{X}^T)^T$; $\boldsymbol{R} = \boldsymbol{I} - \boldsymbol{X}(\boldsymbol{X}^T\boldsymbol{X})^{-1}\boldsymbol{X}^T\boldsymbol{Y}$ is the residual forming matrix; tr() denotes the trace operator. The portion of the brain tissue within the pixel b on the 2D map is considered to be activated by the event of interest X_{p_0}, if the absolute value of its t-statistic is large enough that it cannot be a result of the type I error (see below). The detailed derivation of the $t_{p_0,b}$ and $EDoF$ is well documented in the publications from the authors of NIRS-SPM (Tak and Ye, 2014; Ye et al., 2009), and thus is not repeated here.

The temporal autocorrelation matrix of fNIRS data $\boldsymbol{V}$ was estimated through the precoloring procedure (Worsley and Friston, 1995; Ye et al., 2009). We applied a temporal smoothing process to the fNIRS data prior to the GLM estimation. The smoothing kernel was considered to be strong enough to "washout" the intrinsic autocorrelation in the original hemoglobin concentration data. Therefore, the new temporal autocorrelation matrix $\boldsymbol{V}$ is obtained by:

$$\boldsymbol{V} = \boldsymbol{S}^T \boldsymbol{\Lambda} \boldsymbol{S} \approx \boldsymbol{S}^T \boldsymbol{S} \tag{3.16}$$

where $\boldsymbol{\Lambda}$ is the (unknown) intrinsic autocorrelation matrix; $\boldsymbol{S}$ is the temporal smoothing kernel.

For each of the four 2D projections, as t-tests were done at each pixel (which means that tens of thousands of hypothesis tests were performed simultaneously), methods to control the familywise error rate (FWER) need to be considered. The current version of nirs10 integrates the Lipschitz-Killing curvature based expected Euler characteristics (EC) threshold from NIRS-SPM (Li et al., 2012), which is based on the fact that the probability of a family-wise error can be approximated by the expected EC at a high threshold.

Finally, in the case that multiple EEG-fNIRS sessions were conducted on a patient, a "patient-level" analysis was also performed following the individual analysis of each session. By a precision-weighted average of the sessions (Tak and Ye, 2014; Ye et al., 2009), the patient-level analysis intended to pool the information from all the recorded sessions. Therefore, for a regressor of interest X_{p_0}, the t-statistic at each pixel b was calculated at the second level across the estimated regression coefficients $\hat{\beta}_{p_0} K_b$ of different sessions.

Below we plot a flowchart of our data processing and statistical analysis pipeline (Figure 3.2) and briefly explain each module below.

(1) fNIRS data preprocessing:

- Noisy channel removal. This module removes noisy/saturated channels on the median of a channel-wise rolling standard derivation measure.
- Baseline normalization: Through this module, the detected light intensity of a channel is normalized to its median value ($OD \rightarrow \Delta OD$).

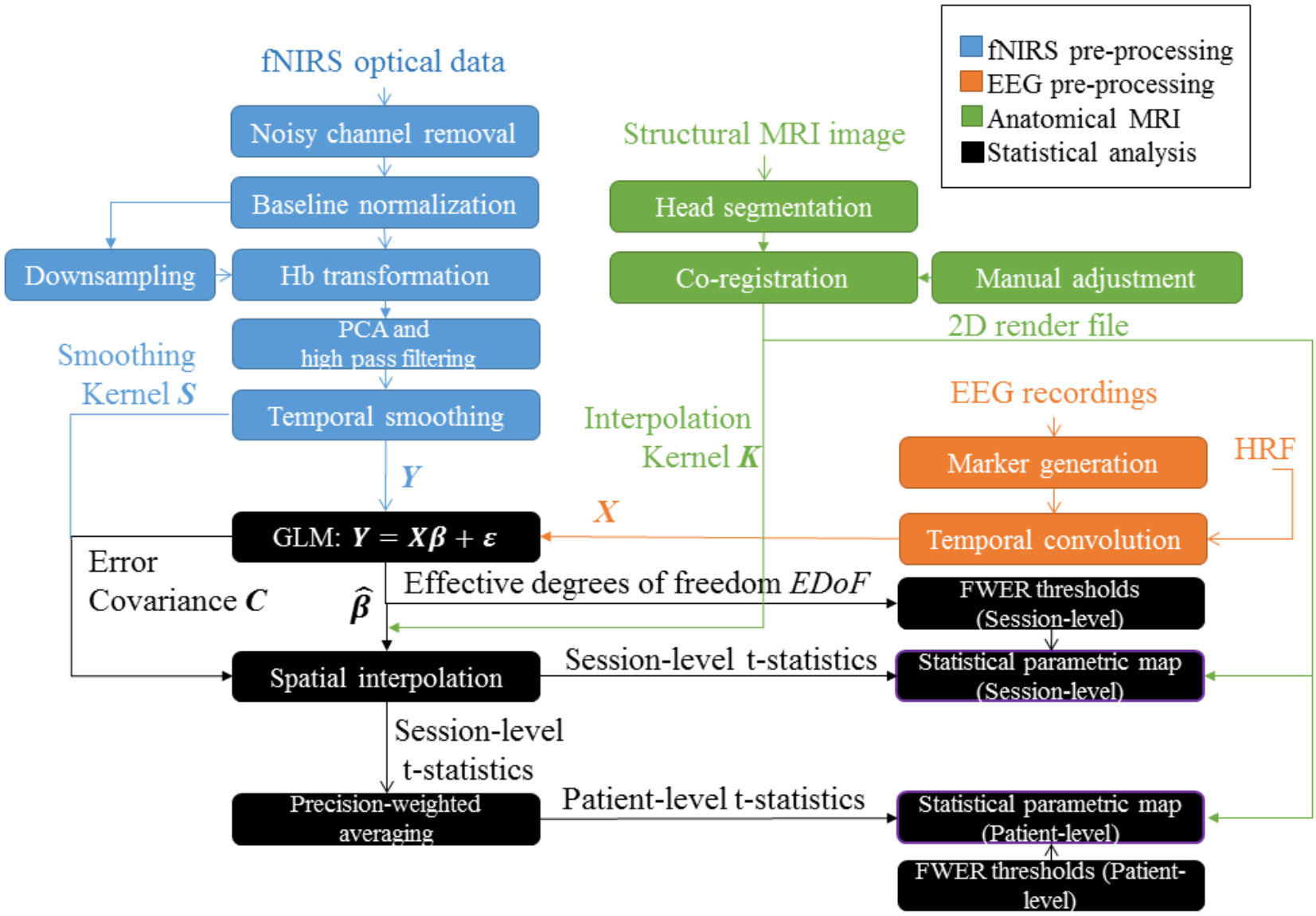

Figure 3.2 Flowchart of EEG-fNIRS data processing and statistical analysis pipeline using the nirs10 toolbox

- Downsampling: If needed (e.g. for a long recording session of 60 minutes or more), the light intensity variations are then downsampled. Low pass filtering is performed prior to the downsampling process according to the Nyquist theorem.
- Hb transformation: The light intensity data of all the channels are transformed to HbO and HbR concentration changes using the MBLL ($\Delta OD \rightarrow \Delta C_{HbO}, \Delta C_{HbR}$).
- PCA and high pass filtering: A principal component analysis (PCA) procedure is applied to the hemoglobin concentration change timecourses of all the channels. This is based on the assumption that movement (such as sudden jumps affecting most channels) and other artifacts such as large physiological responses are common to all channels but unrelated to the IED response. One component with the most variance is removed in this module. A 4^{th} order Butterworth high pass filter is also applied with the cutoff frequency at 0.01Hz.
- Temporal smoothing: We smooth the hemoglobin concentration change data by applying a low pass filter with the shape of the SPM8 canonical HRF. The full width at half maximum (FWHM) is about 4 s wide. Under a simplifying assumption that the shape of the SPM8 canonical HRF is not too different from a Gaussian function, the cutoff frequency *f* is related to the FWHM by $f = 2.36/\text{FWHM}$, or about 0.6 Hz.

(2) EEG recording processing:

- Marker generation: A sequence of time and duration is generated for each type of epileptic event (if present) according to the markers of the neurologists on EEG. A heartbeat rate vector is also generated from EKG and is carefully reviewed.
- Temporal convolution: The sequences (of time and duration) of each type of epileptic event are linearly convolved with a selected HRF to obtain the expected hemodynamic response to these events.

(3) Structural MRI image processing:

- Head segmentation: The structural MRI image of a patient's head is segmented into the following six layers: white matter, grey matter, cerebrospinal fluid (CSF), skull, scalp and air. Four 2D cortical projections (frontal, dorsal, right and left) are extracted from the grey matter layer.

- Coregistration: The positions of all fNIRS optodes (sources and detectors) are mapped automatically to the four cortical projections of the patient's grey matter layer. The coordinates of an fNIRS channel are obtained by mapping the midpoint of its corresponding source and detector onto the cortex.
- Manual adjustment: If the automatic coregistration is not perfect for some optodes, minor manual adjustment is allowed. The positions of all the optodes should correspond to the photo taken on the patient during the actual EEG-fNIRS recording.

(4) Statistical analysis

- General linear model: The hemoglobin concentration changes of all the channels and the expected hemodynamic responses to epileptic or physiological events are aligned with a general linear model. The regression coeffients for all regressors and the error variance are estimated with least square method.
- Spatial interpolation: For each recording session, the estimated regression coefficients and error variance are interpolated to the four 2D projections using an inhomogeneous interpolation kernel.
- FWER threshold calculation (Session-level): With the EC correction method, a t-value threshold is calculated for each of the four 2D projections to control the false positive rate on the corresponding contrast map.
- Statistical parametric mapping (Session-level): A t-statistical test is conducted at each pixel of the four 2D projections. After applying the session-level FWER threshold, the t-statistics are rendered onto the projected grey matter layer.
- Precision-weighted averaging: The session-level estimated regression coefficients of all the sessions are weighted over error variance for a second-level statistic test.
- FWER threshold calculation (Patient-level): The EC method seems to be a bit too restrict for the number of the sessions is usually limited for one patient. In the current version of nirs10, a 2D peak false discovery rate (pFDR) correction is applied for the patient-level t-statistic correction (see chapter 4).

- Statistical parametric mapping (Patient-level): A t-statistical test is conducted at each pixel of the four 2D projections using the estimated regression coefficients of all sessions as data samples. After applying the session-level FWER threshold, the patient-level t-statistics are rendered onto each of the four projected grey matter layer.

CHAPTER 4 ARTICLE #1: FNIRS-EEG STUDY OF FOCAL INTERICTAL EPILEPTIFORM DISCHARGES

Ke Peng[1], Dang Khoa Nguyen[2], Tania Tayah[2], Phetsamone Vannasing[3], Julie Tremblay[3], Mohamad Sawan[1], Maryse Lassonde[3,4], Frédéric Lesage[1,5], Philippe Pouliot[1,5]

1 Département de génie électrique, École Polytechnique de Montréal, C.P.6079, Succ. Centre-ville, Montréal, Qc, Canada H3C3A7; 2 Service de neurologie, Hôpital Notre-Dame du CHUM, 1560 Rue Sherbrooke Est, Montréal, Qc, Canada H3L4M1; 3 Centre de recherche, Hôpital Sainte-Justine, 3175 Chemin de la côte-Sainte-Catherine, Montréal, Qc, Canada H3T1C5; 4 Centre de recherche en neuropsychologie et cognition, Département de psychologie, Université de Montréal, Montréal, Qc, Canada H3C3J7; 5 Institut de cardiologie de Montréal, Centre de recherche, 5000 Rue Bélanger Est, Montréal, Qc, Canada H1T1C8

This article addresses the first objective of this thesis, which is to provide estimates for the sensitivity and the specificity in detecting the hemodynamic response to IEDs and in localizing the epileptic focus region, with a GLM-based approach. This article has been published in *Epilepsy Research* in 2014 (Peng et al., 2014).

4.1 Abstract

Functional near-infrared spectroscopy (fNIRS) acquired with electroencephalography (EEG) is a relatively new non-invasive neuroimaging technique with potential for long term monitoring of the epileptic brain. Simultaneous EEG-fNIRS recording allows the spatio-temporal reconstruction of the hemodynamic response in terms of the concentration changes in oxyhemoglobin (HbO) and deoxy-hemoglobin (HbR) associated with recorded epileptic events such as interictal epileptic discharges (IEDs) or seizures. While most previous studies investigating fNIRS in epilepsy had limitations due to restricted spatial coverage and small sample sizes, this work includes a sufficiently large number of channels to provide an extensive bilateral coverage of the surface of the brain for a sample size of 40 patients with focal epilepsies. Topographic maps of significant activations due to each IED type were generated in four different views (dorsal, frontal, left and right) and were compared with the epileptic focus previously identified by an epileptologist.

After excluding 5 patients due to the absence of IEDs and 6 more with mesial temporal foci too deep for fNIRS, we report that significant HbR (respectively HbO) concentration changes corresponding to IEDs were observed in 62% (resp. 38%) of patients with neocortical epilepsies. This HbR/HbO response was most significant in the epileptic focus region among all the activations in 28%/21% of patients.

Keywords: Focal epilepsy; fNIRS; NIRS-SPM; EEG; Interictal epileptic discharges

4.2 Introduction

Functional near-infrared spectroscopy (fNIRS) is a promising functional imaging approach to monitor brain activity (Jöbsis, 1977). Since hemoglobin is the main absorber of near-infrared (NIR) light (wavelengths in the range from 650 nm to 900 nm), fNIRS is capable of recording the concentration changes in deoxy-hemoglobin (HbR), oxy-hemoglobin (HbO) and total hemoglobin (HbT, which is a proxy for regional cerebral blood volume (rCBV)) in the human brain using their spectroscopic properties (Delpy and Cope, 1997; Desjardins et al., 2012). Application of fNIRS to epilepsy research is of interest as it offers the potential for long-term non-invasive and high temporal resolution hemodynamic imaging, with perhaps more flexibility in experimental setup including lower cost and portability (Irani et al., 2007; Lareau et al., 2011; Lloyd-Fox et al., 2010). With electroencephalographic (EEG) signals simultaneously acquired with fNIRS, the hemodynamic changes associated with epileptiform events such as interictal epileptiform discharges (IEDs) and seizures can be investigated. Using a high number of channels for extended spatial coverage, our group has recently shown the potential of fNIRS to accurately detect hemodynamic changes associated with focal seizures, localize the epileptic focus and characterize the complex local and remote oxygenation changes occurring during such events (Nguyen et al., 2013, 2012). However, because seizures are random and seldom occur during EEG-fNIRS testing, we sought to determine if IEDs captured during these long recordings could also provide useful localization information, as IEDs have been shown to be highly correlated with seizures and are also considered as fundamental components contributing to epileptogenesis (Gotman, 2008; Gotman et al., 2006; Staley and Dudek, 2006).

Although IEDs are more easily captured during recordings than seizures and generally not associated with movement artifacts, they are associated with a weaker neurovascular response than seizures, which poses additional methodological challenges. In a preliminary investigation, we

previously showed the feasibility of recording the hemodynamic response due to IEDs with EEG-fNIRS (Machado et al., 2011). There we found a spatially concordant increase in rCBV at the epileptogenic focus on one patient with focal epilepsy, and on three more in (Pouliot et al., 2012) where concordance with EEG-fMRI was investigated. Here, we extend the results of this work to a larger dataset of forty patients. Our main objectives are to investigate the distribution of activations associated with IEDs and to evaluate the preclinical value of using only EEG-fNIRS data for focus localization.

4.3 Methods

4.3.1 Simultaneous EEG-fNIRS recording

Forty patients with refractory focal epilepsy investigated for potential epilepsy surgery underwent continuous EEG-fNIRS recording at the Optical Imaging Laboratory of Saint-Justine Hospital. The study was approved by the Ethics Committees of Sainte-Justine and Notre-Dame Hospitals and informed consents were obtained from all subjects. Most EEG-fNIRS studies were performed while patients were admitted for video-EEG monitoring as part of their presurgical evaluation, at which time anticonvulsants were frequently reduced or tapered for clinical purposes. An epileptologist was available at all times to ensure patient safety. In addition to video-EEG monitoring, the comprehensive presurgical evaluation included ictal single photon computed tomography (iSPECT), positron emission tomography (PET), anatomical brain magnetic resonance imaging (MRI) and magnetoencephalography (MEG). When needed, an intracranial EEG study was performed. Localization of the most plausible epileptic focus region was carried out by an epileptologist (DKN) based on multimodal analysis of clinical, electrophysiological, structural and functional imaging data as it is usually done in major epilepsy centers for the purpose of epilepsy surgery. Basically, one looked for congruency among clinical semiology analysis, location of scalp interictal and ictal EEG findings, location of the epileptogenic lesion on MRI when present, activations during iSPECT, source localizations by MEG, findings from intracranial EEG recordings when available. The epicenter of the epileptic focus was then transposed onto the 3D brain. The extent of the epileptic focus was arbitrarily set as a 30mm radius sphere around this epicenter.

A detailed description of the EEG-fNIRS recording process can be found in Nguyen et al. (2012). Briefly, custom helmets for different head sizes were designed to mount 64 fibered light sources and up to 16 detectors, as well as 19 carbon EEG electrodes onto the patient heads. For each patient, optode and electrode positions were co-registered onto a 3-D high resolution anatomical MRI image (obtained previously) using the BrainSight software (Rogue-Research, Montreal, Canada). The EEG was recorded at 500Hz with a Neuroscan Synamps 2TM system (Compumedics, USA). A band-pass filter between 0.1Hz and 100Hz was applied to remove instrumental noise and other artificial disturbances. The fNIRS data was captured simultaneously using a multi-channel Imagent Tissue Oximeter (ISS Inc., Champaign, IL, USA). The oximeter employed a frequency-domain method which implied that light sources are intensity modulated over time at 110MHz. Optical channels, consisting of one fiber source and one detector that could see several sources, were usually three to five centimetres apart to ensure sensitivity to cortical tissue. Two different wavelengths were used in recordings, one at 690nm which is more sensitive to HbR and the other one at 830nm which is more sensitive to HbO, and were both recorded through multiple optical channels (115±39 channels per subject). The channel positions were intentionally arranged so that the covered area would include the whole lobe that contained the most probable epileptic focus, the contralateral lobe, and as much area as possible of the other lobes. The DC light intensity probed by detectors was sampled at a frequency of 19.5Hz. Two to twelve consecutive sessions (or "runs") of typically 15 minutes each were recorded for each patient. During the recordings, the patient was simply asked to sit comfortably in a chair and relax. IED regressors and possible seizure regressors were marked offline on the EEG trace using Analyzer 2.0 (Brain Products GmbH, Germany) by a certified clinical neurophysiologist (TT) and reviewed by an epileptologist (DKN). For the 12 patients who had more than one type of IEDs, these were divided in distinct IED types (e.g.1. right temporal spikes and left temporal spikes in some patients with bi-temporal lobe epilepsy; e.g.2. right frontal spikes and diffuse spike and wave from secondary bilateral synchrony in some other patients). IEDs of each type were only analyzed if they occurred frequently enough (>1/200 Hz, i.e. at least 18 IEDs per hour). From the recorded electrocardiogram, a heartbeat rate regressor was derived and manually checked to correct inaccuracies.

4.3.2 Data Processing

The fNIRS data was processed with a Matlab (MathWorks, USA) toolbox developed in-house, called nirs10 (available upon request), based on SPM8 (Friston et al., 2007) and NIRS-SPM (Jang et al., 2009; Ye et al., 2009). Channels with source-detector separation greater than 6 cm or with standard deviation greater than 10% of the mean were removed right away and were not included in channel counts presented later on, following Nguyen et al. (2013, 2012). Concentration changes of HbR and HbO were obtained from light intensity using the modified Beer-Lambert Law. Principal component analysis (PCA) was performed on NIRS data and, following data inspection, one component with the most variance was removed, to reduce movement such as sudden jumps affecting most channels as well as other artifacts such as large physiological responses, common to all channels, and presumed unrelated to the IED response. Concentration changes were then high-pass filtered with an infinite response 4th order Butterworth filter at 0.01Hz, and low-pass filtered using a filter with the shape of the canonical SPM8 hemodynamic response function (HRF).

The hemoglobin concentration changes Y for each channel were fitted by a general linear model (GLM), namely a decomposition of the response variable Y into a linear combination of explanatory variables X_i plus an error term ε, $Y = X\beta + \varepsilon$. The design matrix X contained one regressor for each IED type, and several additional confound regressors included only as confounds, i.e. to remove variance in the data, and not further studied in this work: regressors for all seizure-like events, a heart rate regressor and a constant. The IEDs were treated as brief impulsions of equal amplitude and their contribution to the design matrix was calculated by convolving their timing with a canonical HRF (Friston et al., 1998). The pre-coloring method (Ye et al., 2009) was used to add known correlated noise, as in (Pouliot et al., 2012).

4.3.3 Coregistration and contrasts

For each patient, an anatomical MRI was segmented into six different layers (air, scalp, skull, CSF, grey matter and white matter). The grey matter layer was used to extract six two-dimensional cortical projections. The three-dimensional position of each channel was projected onto these two-dimensional topographic maps, of which 4 views were considered: dorsal, frontal, left and right views. Two-dimensional contrast maps for each IED type were finally generated by interpolation of the amplitudes, β_i, of the hemodynamic responses for the four views, as well as for each session

of each patient. Patient-level analysis followed the analysis of each session as a way to pool the information from all the recorded sessions. As in Ye et al. (2009), this was done by a precision-weighted average of the session contrast maps.

There is evidence that during IEDs a compensatory increase in rCBV in the focus region could be expected, concomitantly with a decrease in local HbR and an increase in local HbO and HbT, to provide extra oxygen supply to the epileptic tissue (Geneslaw et al., 2011; Penfield and Jasper, 1954; Saito et al., 1995; Suh et al., 2006). Thus at each location on 2D maps, a hemodynamic response to IEDs was called "standard", or non-inverted, if the response at that location was a negative change for HbR, or a positive change for HbO/HbT.

One-tailed t-statistic maps (T-maps) were obtained for each IED type, testing the null hypothesis that the HbR did not decrease (resp. that HbO or HbT did not increase), with the other IED types considered as potential confounds.

Assuming a p-value of 0.05, the patient-level significance of the hemodynamic responses to IEDs was decided upon a peak False Discovery Rate (pFDR) correction. A rigorous implementation of pFDR for NIRS is beyond the scope of this paper. Instead, the following heuristic procedure was used (denoted as 2D-pFDR): 1- a list was made of the uncorrected p-values of the pixels at the local peaks on the 2D contrast map of the view of interest. This view (usually left or right, sometimes dorsal) was chosen to best cover the location of the most frequent IED type. 2- Only those peaks which surpassed a first height threshold were then sent to the FDR-BH algorithm (Benjamini and Hochberg, 1995), where their p-values were treated as coming from independent tests. Here we chose $u>2.5$ as this first threshold as in Chumbley et al. (2010). This procedure produced a new height threshold which was then applied to the whole 2D T-maps of all the views to finally control the false positive rate of all pixels.

4.3.4 Sensitivity & specificity definition

The most plausible epileptic focus region, which was represented as a 30mm radius sphere around the epicenter of each patient, was also projected onto the four 2D views. The overlap between the projected focus and the patient-level statistical maps of activations could thus be assessed. The sensitivity and specificity, calculated separately on HbR maps or on HbO/HbT maps, were defined as follows: For each patient, a positive was decided for sensitivity if the epileptic focus region

overlapped a non-inverted significant “standard” hemodynamic response. A positive was decided for specificity if the change in HbR/HbO in the epileptic focus region was the most significant among the other significant HbR/HbO clusters, and thus would lead to a successful identification of the epileptic focus region. An observed hemoglobin concentration change was said to be the most significant if it occupied a larger area on the cortex than any other standard response all over the brain, or if it contained a higher maximum statistical score in case the areas of two or more clusters were very close in size. Specificity was set to negative if sensitivity was negative.

4.4 Results

Forty patients with drug-resistant epilepsy underwent an EEG-fNIRS study (26 males; mean age 33; range 10-62). Three of the forty patients (#19, #22, #34) were excluded as very few IEDs were detected on EEG recordings (#22, #34: no IED was captured; #19: only 1 IED was captured during a 15-minute recording); another (#17) was excluded because fNIRS optodes were not covering the epileptic focus due to technical problems, a fifth one (#37) was excluded because focus localization was clinically uncertain despite extensive multimodal evaluation. Subsequent data analysis was undertaken on the remaining 35 patients.

Table 4.1 provides the type and total number of IEDs that were recorded for each patient. According to conventional anatomy, each hemisphere of the brain was divided into four major lobes: Frontal (F), Temporal (T), Parietal (P) and Occipital lobes (O). Among the 35 remaining patients, 29 patients (83%) suffered from neocortical epilepsy while 6 patients had a mesial temporal focus.

Because EEG-fNIRS can only sample the superficial cortex, data was examined separately between patients with neocortical epilepsies and mesial temporal lobe epilepsies (MTLE). For neocortical epilepsy, the markings of significant ($p<0.05$, 2D-pFDR corrected) concentration changes in HbR are depicted in Table 4.2, while the markings for HbO and HbT can be found in Appendix (Table 4.3). For MTLE, the results for all the chromophores are provided in Appendix (Table 4.4). In these tables, an up arrow ↑ (down arrow ↓) indicates that an increase (resp. a decrease) in the concentration of the hemoglobin was observed in the corresponding locations of the contrast maps. A double arrow sign ↑↑ or ↓↓ means that the given activation was recognised as being the most significant.

Table 4.1 Types and total numbers of IEDs identified on EEG recordings

Neocortical Epilepsy

#	Focus	IED Type (Number)	Number of Channels	Number of Sessions	Recording Time(min)	#	Focus	IED Type (Number)	Number of Channels	Number of Sessions	Recording Time(min)
1	R F(polar)	R F (105)	28	5	81	**24**	R F(IFG)	R FC (298)	135	4	60
2	R P	R P (605)	49	2	35	**25**	L F(SFG+MFG)	L FC (1023)	203	7	100
3	L F(SFG+MFG)	L (865)	45	5	76	**26**	L T(PostMTG+ITG)	L T (1424)	152	5	72
4	L F(MFG)	L CP (3283)	53	7	102	**27**	R T	R T (1128), L T (138)	144	6	87
5	L T(PostSTG+MTG)	L T (72)	57	2	19	**28**	L OrbitalF, L F(IFG)	L T (1969), L F (279)	132	8	120
7	R F(IFG)	R FT (2302) biD R>L (6) biF R>L (15)	134	4	54	**29**	R F(IFG)	R F (1541)	92	4	60
8	R F(IFG+MFG)	R F (238)	94	8	129	**30**	L O	L TO (1157)	107	3	45
10	R F(IFG) R INS	biF R>L (1317), biF L>R (524) F (115)	73	7	100	**31**	R OrbitalF, RF aINS	R FT (494)	129	4	60
11	L T(STG), L INS L F(IFG)	L T (305)	127	7	107	**33**	R F(IFG), R aINS	R F (103)	142	7	106
12	L T(STG) L F(IFG), L INS	L (16)	135	1	15	**35**	R T(PostMTG+ITG) L T	R T (389) L T (23)	146	6	90
13	L T(PostMTG+STG)	L T (97) L F (153)	146	12	181	**36**	L aINS, L F(IFG)	L FT (1088), L F (5) BiF L>R (1450)	144	4	50
15	R INS	R T (63)	106	6	84	**38**	R T(PostITG), R O	R T (666), R FT (530)	106	6	83
16	R F(SFG), R PreCG	R C (3377)	174	3	47	**39**	R F(SFG), R SMA	Cz (550)	121	5	70
21	R F(IFG)	R F (781)	141	6	83	**40**	L PreCG	L F (117)	140	9	135
23	L F(SFG+MFG)	L FCP (1210)	118	5	38						

Mesial Temporal Lobe Epilepsy

#	Focus	IED Type (Number)	Number of Channels	Number of Sessions	Recording Time(min)	#	Focus	IED Type (Number)	Number of Channels	Number of Sessions	Recording Time(min)
6	L T(mesial) R T(mesial)	L T (242) R T (577)	68	3	41	**18**	L T(mesial)	L F (74), L T (44)	133	6	83
9	R T(mesial)	R T (148), R FT (34)	61	6	90	**20**	L T(mesial)	L FT (159)	153	10	143
14	R T(mesial) L T(mesial)	R T (43) L T (1148)	150	11	156	**32**	L T(mesial)	L T (249), L CP (6)	101	5	74

Abbreviations: L: Left; R: Right; F: Frontal; T: Temporal; P: Parietal; O: Occipital; C: Center; SFG: Superior frontal gyrus; MFG: Middle frontal gyrus; IFG: Inferior frontal gyrus; CG: Central gyrus; STG: Superior temporal gyrus; MTG: Middle temporal gyrus; ITG: Inferior temporal gyrus; Post: Posterior; INS: Insular; aINS: anterior insular; SMA: Supplementary motor area.

4.4.1 EEG-fNIRS response in neocortical epilepsies versus mesial temporal lobe epilepsies

4.4.1.1 Neocortical epilepsies

Detailed results from Patient #36 and Patient #7 are presented below to illustrate the analytical procedure, followed by a summary of results from all the 29 patients with a neocortical focus.

• Illustrative case 1 (Patient #36):

This 36 year-old man with pharmacoresistant predominantly nocturnal seizures had an epileptic focus in the left inferior frontal gyrus confirmed by MEG (Figure 4.1A), intracranial EEG and a good surgical outcome following epilepsy surgery (Engel II; follow-up 3 years). 144 fNIRS and 19 EEG channels provided a full coverage of bilateral frontal lobe, temporal lobe and central areas (Figure 4.1B). Three types of IEDs were identified from four sessions with a total recording time of 50 min (Figure 4.1C): 1088 left fronto-temporal IEDs at a rate of 22 per minute (referred as type I IEDs); 1450 bi-frontal (L>R) IEDs at a rate of 29 per minute (type II); 5 left frontal IEDs at a rate of 6 per hour (type III). Ignoring type III IEDs due to their low frequency, we show the projection onto the grey matter image of 2D-pFDR corrected patient-level HbR concentration contrasts associated with type I and II IEDs in Figure 4.1D and E. No significant HbO or HbT response to type I or type II IEDs was observed. The most probable epileptic focus region determined from pre-surgical evaluation was represented as a green circle of 30mm radius. Sensitivity and specificity were decided by jointly looking at the T-maps of type I and II IEDs: type I IEDs were ignored since only very small activations were present in the left and right pre-central gyrus. For type II IEDs, significant HbR decreases were located in the left inferior frontal gyrus and part of the left superior temporal gyrus, mostly inside the focus circle with a minimum t-value of -3.2. On the contralateral right inferior frontal gyrus, less significant HbR decreases were also located as expected with a minimum t-value of -2.9. Hence, both the sensitivity and the specificity were declared positive on HbR.

Comparing the T-maps of the left and the right view, experts could easily lateralize to the left hemisphere. A left inferior frontal focus could be immediately inferred for this patient, following the position of the most significant HbR decreases.

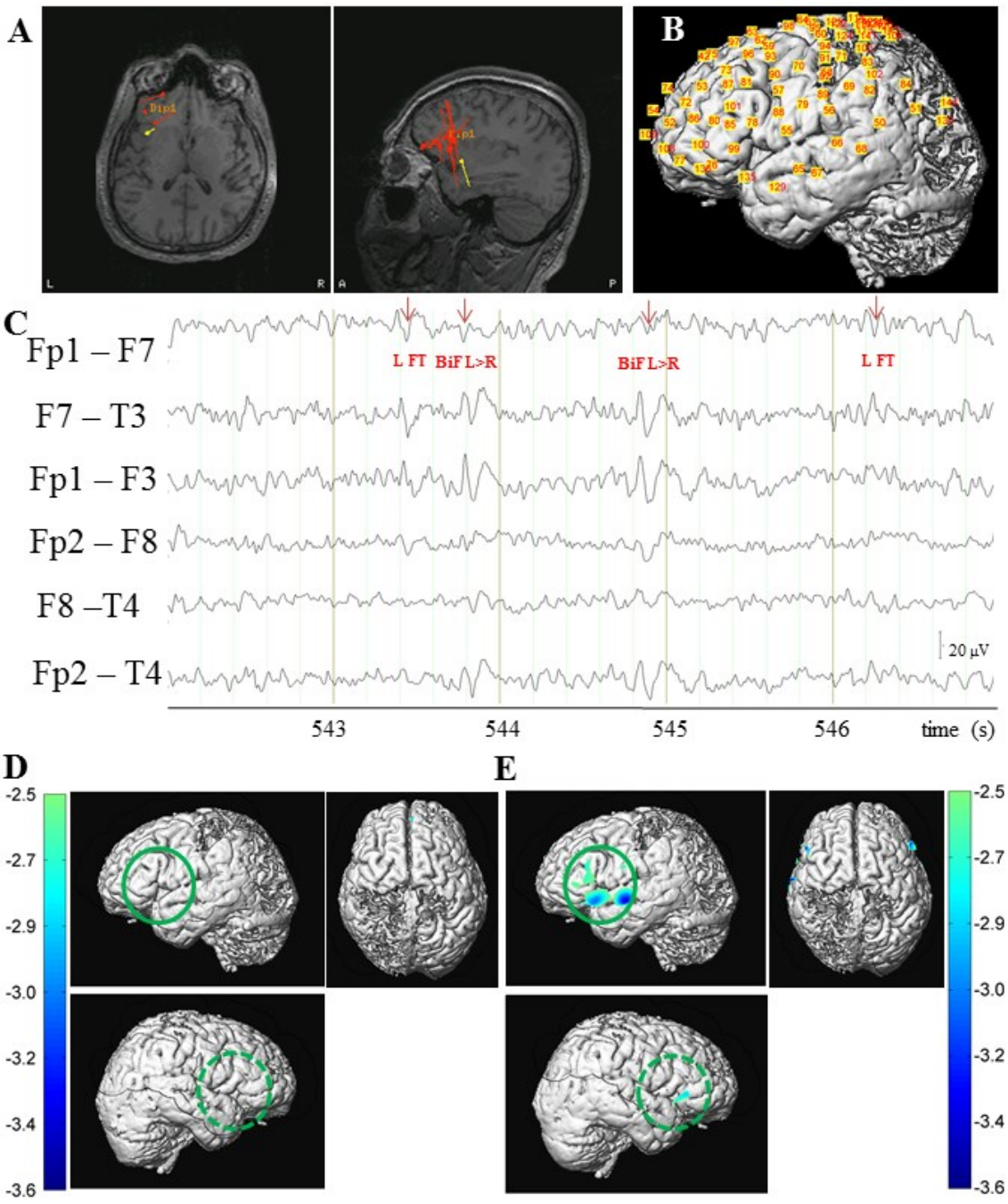

Figure 4.1 Patient #36. (A) MEG dipole localization of epileptic spikes revealing a cluster of sources in the L inferior frontal gyrus and L anterior insula. (B) Reconstructed NIRS channel map over grey matter layer (Left view). (C) EEG fragment with marking for L fronto-temporal and bi-frontal IEDs. (D) Hemodynamic response (HbR) to R fronto-temporal IEDs (Type I) at patient-level (2D-pFDR corrected, $p<0.05$). Solid green circle (30mm radius): focus region; dashed green circle: contralateral region corresponding to focus. (E) HbR response to bi-frontal IEDs (Type II).

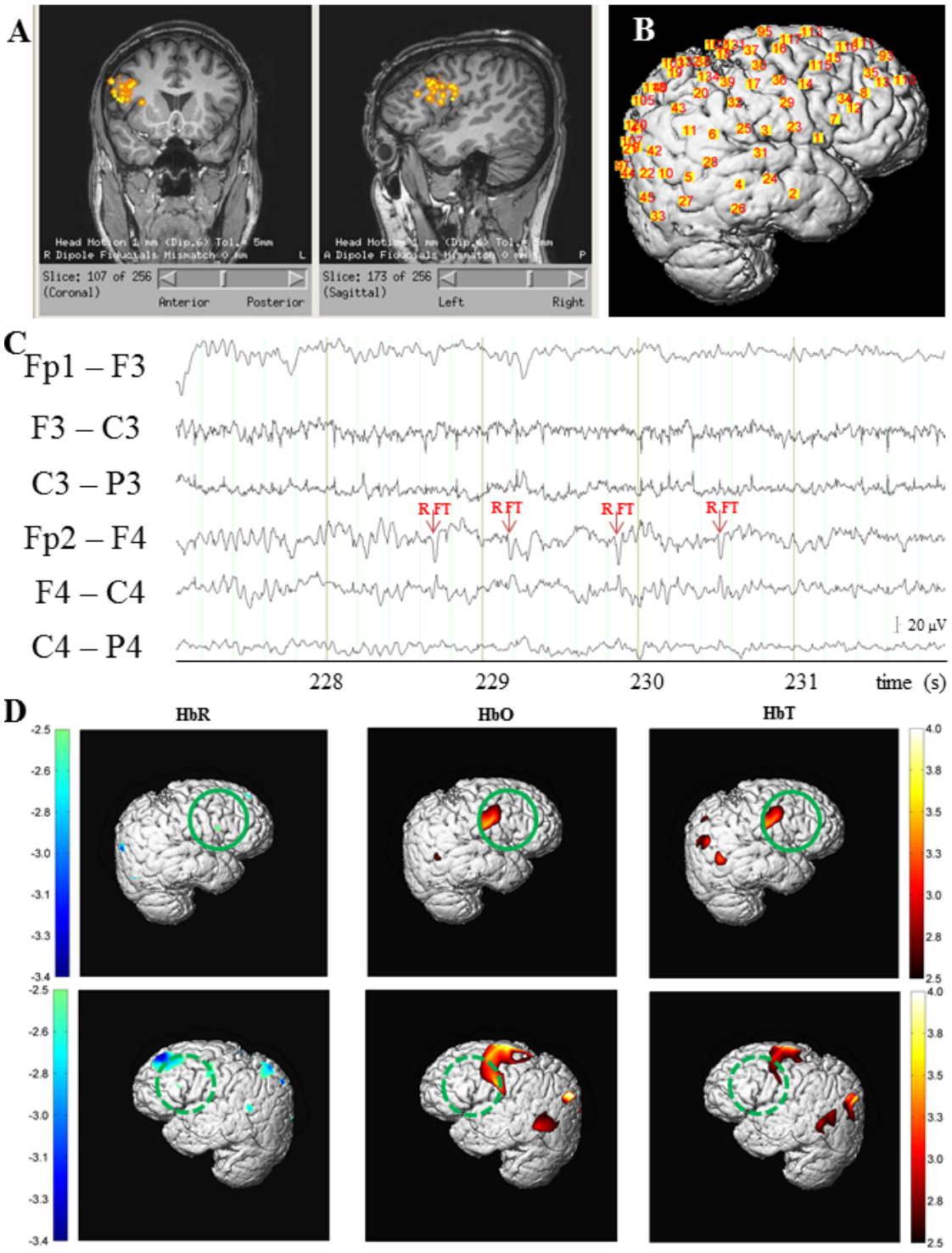

Figure 4.2 Patient #7. (A) MEG dipole localization of epileptic spikes revealing a cluster of sources in the right inferior frontal gyrus. (B) Reconstructed NIRS channel map over grey matter layer (Right view). (C) EEG fragment with marking for right fronto-temporal IEDs. (D) Hemodynamic responses to right fronto-temporal IEDs, patient level (2D-pFDR corrected, $p<0.05$). Solid green circle (30mm radius): focus region; dotted green circle: contralateral region corresponding to focus.

Table 4.2 Hemodynamic response regions of focal IEDs in neocortical epilepsy (HbR)

Neocortical Epilepsy										
#	Focus	Hemodynamic response					SENS	SPEC		MIRR
		Congruent with focus	Outside focus				↓	U	L	
			Intra lobar	Extra lobar	Contralateral					
					Mirrored (to focus)	Not-Mirrored				
1	RF(polar)	↓↓R F (polar)					1	1	1	0
2	RP						0	0	0	
3	L F (SFG+MFG)				↓↓R F (SFG+MFG)		0	0	0	
4	L F(MFG)	↓↓L F (MFG)					1	1	1	0
5	L T (postSTG +MTG)						0	0	0	
7	R F (IFG)	↓R F (IFG)		↓RO	↓L F (IFG)	↓↓L F (SFG), ↓L T, ↓L P	1	0	0	1
8	R F (IFG+MFG)	↓R F (IFG)				↓↓L P	1	0	1	0
10	R F (IFG), R INS		↓↓R F (SFG)	↓R F (PreCG)	↓L F (IFG)	↓LT (STG)	0	0	0	
11	L T(STG) L F (IFG), L INS		↓L F (SFG)		↓L F (IFG)	↓↓R F (preCG)	0	0	0	
12	L T (STG) L F (IFG) L INS						0	0	0	0
13	L T (postMTG + STG)	↓L T (postMTG)		↓L F (IFG)	↓R F (postCG)	↓↓R F (SFG + postCG)	1	0	0	1
15	R INS						0	0	0	
16	R PreCG R F (SFG)						0	0	0	
21	R F (IFG)	↓R F (IFG)	↓R preCG ↓R F(SFG)	↓R T (STG)	↓↓L F (IFG)	↓L T (STG)	1	0	1	1
23	L F (SFG+MFG)	↓L F (SFG)			↓R F (SFG)	↓↓R T (Post STG) ↓R F (MFG)	1	0	1	1
24	R F (IFG)						0	0	0	
25	L F (SFG + MFG)	↓↓L F (SFG + MFG)	↓L F (IFG)		↓R F (SFG+MFG)		1	1	1	1
26	L T (PostMTG + ITG)	↓↓L PostMid	↓L T (STG)				1	1	1	0
27	R T					↓↓L F (IFG)	0	0	0	
28	L ObitalF L F (IFG)			↓↓L P		↓R F (SFG)	0	0	0	
29	R F (IFG)	↓R F (IFG)			↓L F (IFG)	↓↓L T (PostTG)	1	0	1	1
30	L O	↓↓L O				↓R P	1	1	1	0
31	R aINS, R F(IFG)	↓R F (IFG)			↓L F (IFG)	↓L T (ITG) ↓↓L F (SFG)	1	0	1	1
33	R F (IFG), R aINS	↓R F (IFG)		↓↓R P			1	0	0	0
35	RT (PostMTG+ITG)	↓R T (STG)	↓R T (STG)		↓L T	↓L P, ↓↓L F (IFG)	1	0	0	1
36	L aINS, L F (IFG)	↓↓L F (IFG)		↓L T (STG)	↓R F (IFG)		1	1	1	1
38	R postITG,R O	↓R T, ↓R O		↓R P	↓↓L P	↓L T, ↓L O	1	0	0	1
39	R F (SFG), R SMA	↓R F (SFG) ↓↓R SMA					1	1	1	0
40	L PreCG	↓↓L PreCG			↓R PreCG		1	1	1	1
					Neocortical Epilepsy Subtotal (Percentage, 29 subjects in total)		62	28	45	61

Abbreviations: L: Left; R: Right; F: Frontal; T: Temporal; P: Parietal; O: Occipital; C: Center; SFG: Superior frontal gyrus; MFG: Middle frontal gyrus; IFG: Inferior frontal gyrus; CG: Central gyrus; STG: Superior temporal gyrus; MTG: Middle temporal gyrus; ITG: Inferior temporal gyrus; Post: Posterior; INS: Insular; aINS: anterior insular; SMA: Supplementary motor area; SENS: sensitivity; SPEC: specificity; U: unbiased; L: pre-lateralized; MIRR: mirrored activation.

• Illustrative case 2 (Patient #7):

This 22-year-old man with pharmacoresistant gelastic seizures had an epileptic focus located in the right inferior frontal gyrus confirmed by MEG (Figure 4.2A), intracranial EEG and seizure-freedom following epilepsy surgery (follow-up 1 year). Prior to surgery, three 15-minute sessions were recorded with EEG-fNIRS followed by a fourth session of 8.4 minutes. 134 NIRS channels (Figure 4.2B) were widely and symmetrically distributed on the helmet, providing a full coverage of the focus region as well as other lobes on the same right side or on the contralateral side. Figure 4.2C shows a segment of EEG recording in Session 2 with 4 IEDs marked. A total number of 2302 right fronto-temporal IEDs were captured in the primary focus region, occurring at an overall rate of 43 per minute. In the meantime, 21 bi-frontal IEDs were also marked, arising at a rate of 23 per hour. Only the hemodynamic response to the right frontal-temporal IEDs is presented as the bi-frontal IEDs arose at less frequently than 1/200 Hz (actual analysis showed no significant activation). In Figure 4.2D, T-maps from the patient-level one-tailed t-tests are depicted. T-thresholds from a 2D-pFDR correction procedure are calculated and applied for the contrast maps. The most plausible epileptic focus region was shown as a circle of 30mm radius.

The activated area in the right inferior frontal gyrus seen in Figure 4.2D was in good concordance with the focus region. A negative concentration change in HbR with a minimum t-value of -2.5, as well as positive changes in HbO and in HbT (resp. 3.5/3.4 maximal t-values), was observed in the green circle which describes the focus region, and was recognized as possible response to IEDs. On the contralateral side, homologous responses (decrease in HbR together with increases in HbO and in HbT) were found both inside and outside the dotted green circle. However, the contralateral response clusters seemed to be more scattered.

Although the analysis has shown sensitivity to the location of epileptic focus, stronger activations in the left superior frontal gyrus were present. Hence, current results with EEG-fNIRS for this patient do not allow specific identification of the focus.

• Summary of neocortical epilepsies (29 patients)

Among the 29 patients who had a neocortical focus, 18 patients (62%) had significant negative HbR concentration changes in the epileptic focus region, which led to a sensitivity of 62% for EEG-fNIRS in HbR. 8 patients (28% of 29 patients, 44% of the 18 patients whose sensitivity has been decided to be positive) had the most significant decrease in HbR in the focus region. Hence

for our sample of patients with neocortical epilepsy, specificity of HbR measured was thus estimated to be 28%.

The results based on HbO and HbT are quite similar. 12 patients (38%) showed a positive HbO concentration change as well as a positive HbT concentration change as expected in the focus region. For 6 patients (21% of 29 patients, 50% of 12 patients), the positive concentration change in the focus region was the most significant positive change. Thus the total sensitivity and specificity based on HbO was estimated to be 38% and 21% respectively.

4.4.1.2 Mesial temporal lobe epilepsies

EEG-fNIRS was insensitive for 5 out of 6 patients (#6, #9, #14, #18 and #32) who suffered from MTLE, while for one patient (#20), it showed increases in HbO and in HbT in the overlying temporal neocortex albeit less significant when compared with other activations, see Appendix (Table 4.4).

4.4.2 Overall concordance between EEG-fNIRS response and epileptic focus region

Combing the results for neocortical epilepsy and for MTLE, we noted that, in the total 35 patients with sufficient IEDs, concordant negative HbR concentration changes could be located near the focus region in 18 patients (12 patients for HbO/HbT), wherein the changes near the focus region was the most significant in 8 patients (6 patients for HbO/HbT). As a result, the estimated HbR sensitivity dropped to 51% (34% for HbO/HbT) while the estimated HbR specificity dropped to 23% (17% for HbO/HbT), when the patient set was undifferentiated to epilepsy types.

4.5 Discussion

With the accelerated technical and methodological developments seen over the last few years, simultaneous EEG-fNIRS is getting closer to the clinical realm. In particular, our group has been working towards implementing long-term EEG-fNIRS in the epilepsy unit and neurological intensive care unit with the development of wireless and wearable multichannel wearable system dedicated for simultaneous EEG-fNIRS acquisitions at the bedside (Lareau et al., 2011; Sawan et al., 2013, Le Lan et al., 2013) and showed that the technique has definite potential to detect, localize and assess the impact of focal seizures (Nguyen et al., 2013, 2012; Pouliot et al., 2014). Although

only a few patients experienced seizures during the one or two hour-long EEG-fNIRS recordings, most had IEDs on EEG. Hence, we decided to determine if such events could provide useful information. Compared with previous work (Machado et al., 2011; Pouliot et al., 2012), this study benefited from several improvements. First, a relatively large number of patients were recorded. Second, hemodynamic responses were systematically analyzed with the same processing pipeline applied to all patients. This uniformity and large sample size allowed for the first time a preliminary estimation of the sensitivity and specificity. Finally, typically about one hundred fNIRS channels provided for a large spatial coverage, which has motivated the discussion below of the concurrent hemodynamic behavior due to IEDs in other remote regions.

4.5.1 Sensitivity and Specificity estimates

In 18 of 29 patients with neocortical epilepsies, concordant HbR decreases due to IEDs in the epileptic focus region were observed (11 for HbO/HbT), which led to an estimation of overall sensitivity to be 62% for HbR (34% for both HbO and HbT). In 8 patients, concordant HbR decreases in the focus region were the most significant (6 for HbO/HbT), thus the overall specificity of EEG-fNIRS was estimated to be 28% for HbR (23% for HbO/HbT). Previous work from our group with fNIRS-EEG showed that temporal and frontal lobe seizures were associated with significant local hemodynamic changes resulting in a considerable sensitivity on the observation of seizures and good specificity (Nguyen et al., 2013, 2012). In this work focussing on IEDs, EEG-fNIRS showed only modest sensitivity, in part explained by the fact that IEDs evoke a less important neurovascular response compared to seizures, even when many IEDs are statistically pooled. Similar studies on the estimation of sensitivity and specificity have also been conducted with EEG-fMRI. The first assessment was done by Salek-Haddadi et al. (2006), where the authors stated that EEG-fMRI was sensitive to the hemodynamic correlates of IEDs in over 68% of their 34 patients with focal epilepsy (while no information about specificity was revealed). In a more recent EEG-fMRI study of 33 patients (Pittau et al., 2012a), the estimates were much higher: the BOLD response was concordant in 29 patients (88% sensitivity) and contributed to the localization of focus in 21 patients (64% specificity). This is somewhat not surprising since EEG-fMRI has better spatial resolution, being able to assess hemodynamic changes from deep-seated structures as well, without surface physiology confounds. As expected, the EEG-fNIRS approach encountered difficulties with MTLE cases. Even if temporal IEDs detected on scalp EEG meant that IEDs from

mesial structures had projected to ~6-10 cm2 of temporal neocortex (Cooper et al., 1965; Tao et al., 2007), we did not detect significant and specific temporal neocortical activations in most cases.

In real clinical practice, lateralization to the left or right hemisphere is seldom an issue as clinical manifestations and scalp EEG findings can usually provide that information. Obtaining more precise localization information within that hemisphere is the more clinically relevant need. If we had restricted our analysis only to fNIRS activations that are topographically related on the basis of observed epileptiform activity (i.e. in the assumed hemisphere of epileptogenicity), specificity would have been increased to 45% for HbR (see Table.2, column SPEC 'L') and 24% for HbO (see Appendix A) while keeping the same sensitivity (62%/38% for HbR/HbO). In this paper, we opted to remain as unbiased as possible and reported sensitivity and specificity estimates without prior assumptions on focus lateralization.

4.5.2 Remote hemodynamic responses

It is increasingly recognized that focal IEDs or seizures generate various hemodynamic changes in areas contiguous, contralateral or remote from the epileptic focus, observable on EEG-fNIRS, EEG-fMRI and SPECT studies (Huberfeld et al., 2006; Kobayashi et al., 2006a; Lee et al., 2000; Nguyen et al., 2013, 2012; Zijlmans et al., 2011). This EEG-fNIRS study of IEDs was no different: in the 18 patients who already had significant HbR responses near the focus, similar HbR activations in the corresponding area of the contralateral lobe, were seen in 11 patients (61%, see Table 4.2; 50% for HbO/HbT, see Appendices Table 4.3 and Table 4.4). More work is necessary to better understand the pathophysiology of these remote changes temporally synchronized with the IEDs.

4.5.3 Limitations

Due to the interpretation of fNIRS responses as cortical activations being confounded in several ways, it was recognized that the development of proper statistical method of fNIRS data was challenging. The group of Ye et al. (2009) refined the statistical threshold calculation by using the expected Euler characteristic, which can be applied at the session or at the group level (Li et al., 2012). In the present work, the EC correction at the session-level was applied (results not shown) leading to clinically reasonable results, but a practical way of pooling this information from all the sessions was not found. On the other hand, using the EC correction at the patient level would have

led to a sensitivity of only 3% and no specificity at all for both HbR and HbO. Thus we observed that, when there are a small number of sessions, EC correction is not a suitable threshold to apply at the patient level, and instead a 2D-pFDR criterion was devised. In future work, pooling the sessions together in the 1st-level analysis and applying the EC correction on that will be considered, ideally by using continuous recordings.

One particular drawback in evoked brain activity detection as mentioned above is the ability to distinguish NIRS signals from various sources of noise originating from tissue layers over the brain and systemic physiology. Here a PCA was used on raw data as a filter to eliminate movement artifacts and other large fluctuations common to most channels, while a heart rate regressor was included in the GLM to remove the effects of cardiac oscillation. Tests were conducted on the data from several patients to ensure that removing the one component with the most variance was a reasonable and effective choice to remove artefacts. A potential consequence of these filtering efforts is that the true sensitivity and specificity could have been misestimated. Improvements on this technique include the use of short source-detector separation (Gagnon et al., 2011; Zhang et al., 2007). However, due to the constraint of maintaining high spatial coverage and of instrumental gain limitations, short channels were not feasible in this study, but were considered to be included in future work.

Also, there was no standard definition to rely upon for sensitivity and specificity of EEG-fNIRS in the analysis of responses due to epileptic events. It was therefore necessary to make a practical proposal for their definition. It is possible that the reliance on experienced neurologists introduced a bias in the estimates of sensitivity and specificity in this study.

4.6 Conclusion

In this work, we extended recent developments using EEG-fNIRS in epilepsy research, contributing new evidence that this technique can detect and characterize local and remote hemodynamic changes associated with IEDs. Our preliminary observations suggest modest sensitivity and specificity to localize the epileptic focus, attributed to an inability to observe hemodynamic changes in deep seated structures and ‘unexpected’ large-scale effects of IEDs that are traditionally considered focal based on EEG readings. Further methodological work and validation work are clearly necessary before the move from bench to bedside.

4.7 Acknowledgments

This work was supported by the Fonds de Recherche en Santé du Québec (FRSQ) grant 14385, the Canadian Institutes of Health Research (CIHR), Institute of Circulatory and Respiratory Health (ICRH) and the Heart and Stroke Foundation of Canada (HSFC) grant 62573, and the Savoy Foundation.

4.8 Appendix

Table 4.3 Hemodynamic response regions of focal IEDs in neocortical epilepsy (HbO/HbT)

Neocortical Epilepsy										
#	Focus	Hemodynamic response					SENS	SPEC		MIRR
		Congruent with focus	Outside focus				↑	U	L	
			Intra lobar	Extra lobar	Contralateral					
					Mirrored (to focus)	Not-Mirrored				
1	RF(polar)		↑↑R PreCG (HbT)				0	0	0	
2	RP						0	0	0	
3	L F (SFG+MFG)	↑↑L F (SFG)			↑R F (SFG) (HbT)		1	1	1	0/1
4	L F(MFG)	↑↑L F (SFG)			↑R PreCG (HbO)		1	1	1	1/0
5	L T (postSTG+MTG)						0	0	0	
7	R F (IFG)	↑R F (IFG)			↑L F (IFG)	↑↑L F (SFG), ↑L T, ↑L P	1	0	1	1
8	R F (IFG+MFG)				↑↑L F (IFG) (HbO) ↑L F (IFG) (HbT)	↑L P (HbO) ↑↑L F (PosCG) (HbT)	0	0	0	
10	R F (IFG) R INS	↑R F (IFG)	↑R F (MFG+SFG)	↑R T (PosITG) (HbO)	↑↑L F (IFG+MFG)	↑L (PreCG)	1	0	0	1
11	L T(STG) L F (IFG) L INS	↑↑L F (IFG)			↑R F (IFG)	↑R P (HbT)	1	1	1	1
12	L T (STG) L F (IFG) L INS						0	0	0	
13	L T (postMTG + STG)	↑↑L T (PostSTG)			↑R T (STG)		1	1	1	1
15	R INS						0	0	0	
16	R PreCG R F (SFG)						0	0	0	
21	R F (IFG)	↑↑R F (IFG)	↑R F (SFG)			↑L T (MTG) (HbO)	1	1	1	0
23	L F (SFG+MFG)			↑L T (STG+MTG) (HbO) ↑L T (STG) (HbT)		↑↑R T (STG + MTG)	0	0	0	
24	R F (IFG)						0	0	0	
25	L F (SFG + MFG)			↑↑L P			0	0	0	
26	L T (PostMTG + ITG)	↑L T (MTG + ITG)		↑↑L P, ↑L O		↑R P	1	0	0	0
27	R T	↑R T (MTG)		↑↑R O, ↑R P		↑L P	1	0	0	0
28	L ObitalF L F (IFG)					↑↑RPostCG	0	0	0	
29	R F (IFG)	↑R F (MFG)	↑R F (MFG) (HbO) ↑↑R F (MFG)(HbT)	↑R P ↑R postCG		↑↑L PreCG (HbO) ↑L PreCG (HbT) ↑L F	1	0	0	0
30	L O					↑↑R P (HbO)	0	0	0	
31	R aINS, R orbtoF(IFG)					↑↑L F (polar) (HbT)	0	0	0	
33	R F (IFG) R aINS					↑↑L T (MTG)	0	0	0	
35	R T (postMTG + ITG)		↑↑R PreCG			↑L F (MFG)	0	0	0	
36	L aINS ,L F (IFG)						0	0	0	
38	R postITG, R O			↑R O, ↑R P		↑↑L O	0	0	0	
39	RF (SFG) R SMA		↑R F (IFG) (HbT)		↑↑L F (SFG)		0	0	0	
40	L PreCG	↑↑L PreCG			↑R PreCG	↑R P	1	1	1	1
					Neocortical Epilepsy Subtotal (Percentage, 29 subjects in total)		38	21	24	55

Abbreviations: L: Left; R: Right; F: Frontal; T: Temporal; P: Parietal; O: Occipital; C: Center; SFG: Superior frontal gyrus; MFG: Middle frontal gyrus; IFG: Inferior frontal gyrus; CG: Central gyrus; STG: Superior temporal gyrus; MTG: Middle temporal gyrus; ITG: Inferior temporal gyrus; Post: Posterior; INS: Insular; aINS: anterior insular; SMA: Supplementary motor area; SENS: sensitivity; SPEC: specificity; U: unbiased; L: pre-lateralized; MIRR: mirrored activation.

Table 4.4 Hemodynamic response regions of focal IEDs in mesial temporal lobe epilepsy (HbR/HbO/HbT)

Mesial Temporal Lobe Epilepsy									
#	Focus	Hemodynamic response				SENS	SPEC		MIRR
		Congruent with focus	Outside focus				U	L	
			Intra lobar	Extra lobar	Contralateral				
					Mirrored (to focus)	Not-Mirrored			
HbR									
	L T (mesial)						0	0	0	
6	R T (mesial)						0	0	0	
9	R T (mesial)			↓↓R F (MFG)		↓L F (MFG)	0	0	0	
	R T (mesial)			↓R F (SFG)		↓↓L F (MFG +SFG)	0	0	0	
14	L T (mesial)					↓↓R F (SFG)	0	0	0	
18	L T (mesial)			↓L P		↓↓R T (PostMTG) ↓R inf P	0	0	0	
20	L T (mesial)			↓LF (MFG)		↓↓R F (MFG)	0	0	0	
32	L T (mesial)		↓L postT	↓↓L preCG ↓L postCG		↓R preCG ↓R postCG	0	0	0	
						HbR: MTLE Subtotal (Percentage, 6 subjects in total)	0	0	0	
						HbR: Overall (Neocortical epilepsy + MTLE Percentage, 35 subjects in total)	51	23	37	61
HbO/HbT									
	L T (mesial)						0	0	0	
6	R T (mesial)			↑↑R F (IFG) (HbT)			0	0	0	
9	R T (mesial)					↑↑L F (IFG)	0	0	0	
	R T (mesial)			↑R PreCG ↑R F (IFG)		↑↑L F (IFG+ MFG)	0	0	0	
14	L T (mesial)			↑↑L F (SFG)		↑R F (IFG)	0	0	0	
18	L T (mesial)			↑L PreCG		↑↑R T (ITG)	0	0	0	
20	L T (mesial)	↑L T (antiMTG)	↑L T (MTG)	↑↑L F (IFG)			1	0	0	0
32	L T (mesial)			↑L Post CG ↑L P ↑↑L PreCG (HbO)		↑R PreCG (HbO) ↑R PostCG (HbO) ↑↑R P (HbT)	0	0	0	
						HbO/HbT: MTLE Subtotal (Percentage, 6 subjects in total)	17	0	0	
						HbO/HbT: Overall (Neocortical epilepsy + MTLE Percentage, 35 subjects in total)	34	17	20	50

Abbreviations: L: Left; R: Right; F: Frontal; T: Temporal; P: Parietal; O: Occipital; C: Center; SFG: Superior frontal gyrus; MFG: Middle frontal gyrus; IFG: Inferior frontal gyrus; CG: Central gyrus; STG: Superior temporal gyrus; MTG: Middle temporal gyrus; ITG: Inferior temporal gyrus; Post: Posterior; INS: Insular; aINS: anterior insular; SMA: Supplementary motor area; SENS: sensitivity; SPEC: specificity; U: unbiased; L: pre-lateralized; MIRR: mirrored activation.

4.9 References

Benjamini, Y., Hochberg, Y., 1995. Controlling the false discovery rate: a practical and powerful approach to multiple testing. *Journal of the Royal Statistical Society*. Series B. Methodological 57, 289–300.

Chumbley, J., Worsley, K., Flandin, G., Friston, K., 2010. Topological FDR for neuroimaging. *Neuroimage* 49, 3057–3064.

Cooper, R., Winter, A.., Crow, H.., Walter, W.G., 1965. Comparison of subcortical, cortical and scalp activity using chronically indwelling electrodes in man. *Electroencephalography and Clinical Neurophysiology* 18, 217–228.

Delpy, D.T., Cope, M., 1997. Quantification in tissue near-infrared spectroscopy. *Philos Trans R Soc Lond B Biol Sci* 352, 649–659.

Desjardins, M., Pouliot, P., Lesage, F., 2012. Principles and Applications of Diffuse Optical Imaging for the Brain. *Current Medical Imaging Reviews* 8, 157–173.

Friston, K.J., Ashburner, J.T., Kiebel, S.J., Nichols, T.E., Penny, W.D., 2007. Statistical Parametric Mapping: The Analysis of Functional Brain Images. Academic Press.

Friston, K.J., Fletcher, P., Josephs, O., Holmes, A., Rugg, M.D., Turner, R., 1998. Event-related fMRI: characterizing differential responses. *Neuroimage* 7, 30–40.

Gagnon, L., Perdue, K., Greve, D.N., Goldenholz, D., Kaskhedikar, G., Boas, D.A., 2011. Improved recovery of the hemodynamic response in diffuse optical imaging using short optode separations and state-space modeling. *NeuroImage* 56, 1362–1371.

Geneslaw, A.S., Zhao, M., Ma, H., Schwartz, T.H., 2011. Tissue hypoxia correlates with intensity of interictal spikes. *Journal of Cerebral Blood Flow and Metabolism* 31, 1394–402.

Gotman, J., 2008. Epileptic networks studied with EEG-fMRI. *Epilepsia* 49 Suppl 3, 42–51.

Gotman, J., Kobayashi, E., Bagshaw, A.P., Bénar, C.-G., Dubeau, F., 2006. Combining EEG and fMRI: a multimodal tool for epilepsy research. *J Magn Reson Imaging* 23, 906–920.

Huberfeld, G., Habert, M.-O., Clemenceau, S., Maksud, P., Baulac, M., Adam, C., 2006. Ictal Brain Hyperperfusion Contralateral to Seizure Onset: The SPECT Mirror Image. *Epilepsia* 47, 123–133.

Irani, F., Platek, S.M., Bunce, S., Ruocco, A.C., Chute, D., 2007. Functional near infrared spectroscopy (fNIRS): an emerging neuroimaging technology with important applications for the study of brain disorders. *Clin Neuropsychol* 21, 9–37.

Jang, K.E., Tak, S., Jung, J., Jang, J., Jeong, Y., Ye, J.C., 2009. Wavelet minimum description length detrending for near-infrared spectroscopy. *J Biomed Opt* 14, 034004.

Jöbsis, F.F., 1977. Noninvasive, infrared monitoring of cerebral and myocardial oxygen sufficiency and circulatory parameters. *Science* 198, 1264–1267.

Kobayashi, E., Bagshaw, A.P., Benar, C.-G., Aghakhani, Y., Andermann, F., Dubeau, F., Gotman, J., 2006. Temporal and Extratemporal BOLD Responses to Temporal Lobe Interictal Spikes. *Epilepsia* 47, 343–354.

Lareau, E., Lesage, F., Pouliot, P., Nguyen, D., Le Lan, J., Sawan, M., 2011. Multichannel wearable system dedicated for simultaneous electroencephalography/near-infrared spectroscopy real-time data acquisitions. *J. Biomed. Opt* 16, 096014–096014.

Le Lan, J., Dupuy, O., Kassab, A., Dehbozorgi, M., Pouliot, P., Vannasing, P., Nguyen, D.K., Fraser, S.A., Bherer, L., Lassonde, M., Lesage, F., Sawan, M., 2013. High-Channel-Count Wearable NIRS-EEG System for Long-Term Clinical Imaging. submitted to Journal of Biomedical Optics.

Lee, S.K., Lee, S.H., Kim, S.K., Lee, D.S., Kim, H., 2000. The clinical usefulness of ictal SPECT in temporal lobe epilepsy: the lateralization of seizure focus and correlation with EEG. *Epilepsia* 41, 955–962.

Li, H., Tak, S., Ye, J.C., 2012. Lipschitz-Killing curvature based expected Euler characteristics for p-value correction in fNIRS. *Journal of Neuroscience Methods* 204, 61–67.

Lloyd-Fox, S., Blasi, A., Elwell, C.E., 2010. Illuminating the developing brain: The past, present and future of functional near infrared spectroscopy. *Neuroscience & Biobehavioral Reviews* 34, 269–284.

Machado, A., Lina, J.M., Tremblay, J., Lassonde, M., Nguyen, D.K., Lesage, F., Grova, C., 2011. Detection of hemodynamic responses to epileptic activity using simultaneous Electro-EncephaloGraphy (EEG)/Near Infra Red Spectroscopy (NIRS) acquisitions. *Neuroimage* 56, 114–125.

Nguyen, D.K., Tremblay, J., Pouliot, P., Vannasing, P., Florea, O., Carmant, L., Lepore, F., Sawan, M., Lesage, F., Lassonde, M., 2012. Non-invasive continuous EEG-fNIRS recording of temporal lobe seizures. *Epilepsy Research* 99, 112–126.

Nguyen, D.K., Tremblay, J., Pouliot, P., Vannasing, P., Florea, O., Carmant, L., Lepore, F., Sawan, M., Lesage, F., Lassonde, M., 2013. Noninvasive continuous functional near-infrared spectroscopy combined with electroencephalography recording of frontal lobe seizures. *Epilepsia* 54, 331–340.

Penfield, W., Jasper, H., 1954. Epileptic Mechanisms (cortical circulation), in: Epilepsy and the Functional Anatomy of the Human Brain. Little, Brown and Company Ed., Boston, pp. 246–264.

Pittau, F., Dubeau, F., Gotman, J., 2012. Contribution of EEG/fMRI to the definition of the epileptic focus. *Neurology* 78, 1479–1487.

Pouliot, P., Tran, T.P.Y., Birca, V., Vannasing, P., Tremblay, J., Lassonde, M., Nguyen, D.K., 2013. Hemodynamic changes during posterior epilepsies: an EEG-fNIRS study. Submitted to *Epilepsy Research*.

Pouliot, P., Tremblay, J., Robert, M., Vannasing, P., Lepore, F., Lassonde, M., Sawan, M., Nguyen, D.K., Lesage, F., 2012. Nonlinear hemodynamic responses in human epilepsy: A multimodal analysis with fNIRS-EEG and fMRI-EEG. *Journal of Neuroscience Methods* 204, 326–340.

Saito, S., Yoshikawa, D., Nishihara, F., Morita, T., Kitani, Y., Amaya, T., Fujita, T., 1995. The cerebral hemodynamic response to electrically induced seizures in man. *Brain Res*. 673, 93–100.

Salek-Haddadi, A., Diehl, B., Hamandi, K., Merschhemke, M., Liston, A., Friston, K., Duncan, J.S., Fish, D.R., Lemieux, L., 2006. Hemodynamic correlates of epileptiform discharges: an EEG-fMRI study of 63 patients with focal epilepsy. *Brain Res.* 1088, 148–166.

Sawan, M., Salam, M.T., Le Lan, J., Kassab, A., Gelinas, S., Vannasing, P., Lesage, F., Lassonde, M., Nguyen, D.K., 2013. Wireless Recording Systems: From Noninvasive EEG-NIRS to Invasive EEG Devices. *IEEE Transactions on Biomedical Circuits and Systems* 7, 186–195.

Staley, K.J., Dudek, F.E., 2006. Interictal Spikes and Epileptogenesis. Epilepsy Curr 6, 199–202.

Suh, M., Ma, H., Zhao, M., Sharif, S., Schwartz, T.H., 2006. Neurovascular coupling and oximetry during epileptic events. *Mol. Neurobiol*. 33, 181–197.

Tao, J.X., Baldwin, M., Hawes-Ebersole, S., Ebersole, J.S., 2007. Cortical substrates of scalp EEG epileptiform discharges. *J Clin Neurophysiol* 24, 96–100.

Ye, J.C., Tak, S., Jang, K.E., Jung, J., Jang, J., 2009. NIRS-SPM: Statistical parametric mapping for near-infrared spectroscopy. *NeuroImage* 44, 428–447.

Zhang, Q., Brown, E.N., Strangman, G.E., 2007. Adaptive filtering for global interference cancellation and real-time recovery of evoked brain activity: A Monte Carlo simulation study. *Journal of Biomedical Optics* 12.

Zijlmans, M., Jacobs, J., Kahn, Y.U., Zelmann, R., Dubeau, F., Gotman, J., 2011. Ictal and interictal high frequency oscillations in patients with focal epilepsy. *Clin Neurophysiol* 122, 664–671.

CHAPTER 5 ARTICLE #2: USING PATIENT-SPECIFIC HEMODYNAMIC RESPONSE FUNCTION IN EPILEPTIC SPIKE ANALYSIS OF HUMAN EPILEPSY: A STUDY BASED ON EEG-FNIRS

Ke Peng[1], Dang Khoa Nguyen[2], Phetsamone Vannasing[3], Julie Tremblay[3], Frédéric Lesage[1,4], and Philippe Pouliot[1,4]

1 Département de génie électrique, Institut de génie biomédical, École Polytechnique de Montréal, C.P.6079, Succ. Centre-ville, Montréal, Qc, Canada H3C3A7; 2 Service de neurologie, Hôpital Notre-Dame du CHUM, 1560 Rue Sherbrooke Est, Montréal, Qc, Canada H3L4M1; 3 Centre de recherche, Hôpital Sainte-Justine, 3175 Chemin de la côte-Sainte-Catherine, Montréal, Qc, Canada H3T1C5; 4 Institut de cardiologie de Montréal, Centre de recherche, 5000 Rue Bélanger Est, Montréal, Qc, Canada H1T1C8

As the standard GLM analysis with a canonical HRF might not be optimal, this article developed novel analysis methods which were to model the linear and the nonlinear patient-specific HRFs with a simple deconvolution algorithm. Detailed study of five patients has suggested that, in most cases, including the proposed specific HRFs in the GLM analysis leads to improved detection of hemoglobin activations. This article addresses the second objective of this thesis, and has been published in *NeuroImage* in 2016.

5.1 Abstract

Functional near infrared spectroscopy (fNIRS) can be combined with electroencephalography (EEG) to continuously monitor the hemodynamic signal evoked by epileptic events such as seizures or interictal epileptiform discharges (IEDs, aka spikes). As estimation methods assuming a canonical shape of the hemodynamic response function (HRF) might not be optimal, we sought to model patient-specific HRF (sHRF) with a simple deconvolution approach for IED-related analysis with EEG-fNIRS data. Furthermore, a quadratic term was added to the model to account for the nonlinearity in the response when IEDs are frequent. Prior to analyzing clinical data, simulations were carried out to show that the HRF was estimable by the proposed deconvolution methods under proper conditions. EEG-fNIRS data of five patients with refractory focal epilepsy were selected due to the presence of frequent clear IEDs and their unambiguous focus localization. For each patient, both the linear sHRF and the nonlinear sHRF were estimated at each channel.

Variability of the estimated sHRFs was seen across brain regions and different patients. Compared with the SPM8 canonical HRF (cHRF), including these sHRFs in the general linear model (GLM) analysis led to hemoglobin activations with higher statistical scores as well as larger spatial extents on all five patients. In particular, for patients with frequent IEDs, nonlinear sHRFs were seen to provide higher sensitivity in activation detection than linear sHRFs. These observations support using sHRFs in the analysis of IEDs with EEG-fNIRS data.

Keywords: hemodynamic response function, nonlinear, deconvolution, IED, EEG-fNIRS, epilepsy

5.2 Introduction

Functional near-infrared spectroscopy (fNIRS) has recently been combined with electroencephalography (EEG) and shown great clinical potential in the study of epilepsy (Obrig, 2014). Based on the measurement of cortical oxy-, deoxy- and total hemoglobin (HbO, HbR and HbT) (Jöbsis, 1977), EEG-fNIRS has specifically been used in epileptic patient assessment for localizing the brain regions that generate abnormal activity (Watanabe et al., 2002).

Our group has recently demonstrated the feasibility of analyzing simultaneous EEG-fNIRS data of interictal epileptiform discharges (IEDs) under a general linear model (GLM) framework for the purpose of activation detection and focus localization (Machado et al., 2011; Peng et al., 2014; Pouliot et al., 2014, 2012). By assuming an invariant hemodynamic response function (HRF) across time, brain regions and subjects (e.g. the SPM8 canonical HRF), we reported modest sensitivity and specificity in the localization of epileptic focus for all chromophore types in our first EEG-fNIRS study on 40 patients with refractory epilepsy (Peng et al., 2014).

However, there is evidence showing that the shape of HRF varies across time, subjects or brain regions in epilepsy (Bagshaw et al., 2004; Bénar et al., 2002; Handwerker et al., 2004; Jacobs et al., 2008; Lemieux et al., 2008) as well as in other brain diseases (Ben Bashat et al., 2012; Veldsman et al., 2015). Based on blood oxygenation level dependent (BOLD)-functional magnetic resonance imaging (fMRI), a variety of specific HRF (sHRF) models have been provided as alternatives to the canonical HRF (cHRF) in the GLM to account for such variability, including using parametric models (Friston et al., 2007, 1998; Gössl et al., 2001; Rajapakse et al., 1998), finite impulse response filters (Goutte et al., 2000; van Houdt et al., 2010), Fourier basis sets

(Josephs et al., 1997), deconvolution (Lu et al., 2006; Ward, 2006), Bayesian methods (Marrelec et al., 2003; Woolrich et al., 2004), machine learning (Pedregosa et al., 2014), etc. Compared with the traditional cHRF, the implementation of a flexible sHRF in fMRI data analysis usually presented larger sizes of detected clusters and higher peak statistic scores in the detection of neuronal activation associated with epileptic events (Jacobs et al., 2007; Lindquist et al., 2009; Proulx et al., 2014; Storti et al., 2013), which reflected a reduction in model misspecification and an improvement in detection sensitivity.

On the other hand, the simplifying assumption of linearity in the hemodynamic response may not hold with the presence of high frequency stimuli (Friston et al., 2000; Heckman et al., 2007; Zhang et al., 2008). The nonlinear aspect of the HRF has been observed in both human epilepsy and animal models. In Jacobs et al. (2008), an fMRI study on children with epilepsy, the authors reported a decrease in HRF peak amplitude with increasing IED frequency. Similar results were obtained from rat experiments in Vanzetta et al. (2010), showing that their measured cerebral blood flow (CBF) did not increase linearly as expected when IED rates exceeded 0.2Hz. In a previous multi-modal study, we used the Volterra kernels (Friston et al., 2000) to quantify the nonlinear hemodynamic effects in epilepsy, and showed improved results both for fMRI and fNIRS (Pouliot et al., 2012). The Volterra series were also applied in a recent approach for multi-subject fMRI (Zhang et al., 2014) to provide sHRF models. However, benefits to the detection power in individual analysis were not discussed.

When processing EEG-fNIRS, similarities with EEG-fMRI can be found as the two techniques share the same physiological basis as well as have comparable experimental designs (Plichta et al., 2007). However, fNIRS recordings usually suffer from a lower signal-to-noise ratio (SNR) and higher contributions from physiology which can then lead to a much weaker statistical significance for the activation (Toronov et al., 2007). Moreover, some inhomogeneity between BOLD signals and optically-measured hemoglobin concentration changes was also reported (Cui et al., 2011; Minati et al., 2011). In summary, despite the fairly large body of literature on the sHRF modeling for fMRI, little work has been done based on fNIRS.

In this paper, we sought to implement a simple nonlinear deconvolution model using Volterra series for the estimation of a patient-specific HRF in fNIRS. The model was validated through tests conducted on extensive simulations. Finally, EEG-fNIRS data acquired from five epileptic patients

with frequent IEDs were processed using a GLM with its design matrix constructed respectively by the sHRFs and an SPM8 cHRF (Friston et al., 2007). Quantitative result comparison was then conducted focusing on the outcomes of activation detection.

5.3 Method

5.3.1 Reconstruction of a specific HRF

In this section, we introduce the nonlinear deconvolution model in detail, as well as our heuristic procedure based on surrogate series to calculate the 95% confidence level on the deconvolved sHRF.

5.3.1.1 The nonlinear deconvolution model

Using Volterra expansion up to second order, fNIRS-measured hemoglobin concentration changes can be related to the stimulus sequence (here IEDs) u with the following model:

$$y(t) = \int_{-\infty}^{\infty} k_1(\sigma)u(t-\sigma)d\sigma + \frac{\lambda}{2}\int\int_{-\infty}^{\infty} k_2(\sigma,\tau)u(t-\sigma)u(t-\tau)d\sigma d\tau + \sum_{i=0}^{I} t^i\omega(i) + \varepsilon(t) \tag{5.1}$$

where k_1 and k_2 are respectively the first and the second Volterra kernels. The ratio of nonlinear expression in the response is controlled by a constant $\lambda/2$. t^i is a polynomial term of order i, $\omega(i)$ is its corresponding coefficient, and $\varepsilon(t) \sim N(0, \delta^2)$ is Gaussian white noise. As in (Pouliot et al., 2012), the first order Volterra term (V_1) and the second order Volterra term (V_2) can be explicitly modelled with respect to the stimulus sequence u and a basis function h as:

$$V_1 = \int_{-\infty}^{\infty} h(\sigma)u(t-\sigma)d\sigma\,, V_2 = \left(\int_{-\infty}^{\infty} h(\sigma)u(t-\sigma)d\sigma\right)^2$$

where h denotes the HRF. Hence, equation (1) becomes:

$$y(t) = \int_{-\infty}^{\infty} h(\sigma)u(t-\sigma)d\sigma + \frac{\lambda}{2}\left(\int_{-\infty}^{\infty} h(\sigma)u(t-\sigma)d\sigma\right)^2 + \sum_{i=0}^{I} t^i\omega(i) + \varepsilon(t) \tag{5.2}$$

Equation (2) can be re-formulated into a discretized form:

$$y_t = \sum_{k=-K_1}^{K_2} u_{t-k}h_k + \frac{\lambda}{2}\left(\sum_{k=-K_1}^{K_2} u_{t-k}h_k\right)^2 + \sum_{i=0}^{I} t^i\omega_i + \varepsilon_t \tag{5.3}$$

Given y, u and assuming reasonable positive integers for K_1, K_2, I, we can derive h, ω and λ using suitable nonlinear parameter estimation algorithms. In this work, for the sake of computation

simplicity, we linearize the nonlinear model and solve it with the Gauss-Newton iteration method (Montgomery et al., 2006), see section 5.8.1.1. It should also be noted that our nonlinear model is a generalization of the linear deconvolution model used in Lu et al. (2006) (see section 5.8.1.2), by introducing the nonlinear coefficient $\lambda \neq 0$.

5.3.1.2 Presentation of confidence levels

The computation of a 1-α_1 confidence level for a deconvolved sHRF (referred to as the true sHRF in this section) was based on a surrogate method (Timmer, 2000): a) for each hemoglobin data time-course, N_s = 1000 surrogate series were first generated using phase randomization (Maiwald et al., 2008) to maintain the autocorrelation of the original signal; b) a spurious sHRF was then deconvolved from each of these surrogate series; c) these N_s spurious sHRFs were compared with the true sHRF under a user-specified criterion. In this work, we used the highest peak amplitude (HPA) of a sHRF within 0 to 15 seconds after the stimulus. The 1-α_1 confidence threshold was set to be the smallest amplitude value that was higher than the HPAs of 1-α_1 of the N_s spurious sHRFs.

5.3.2 Simulation methodology

Simulations were then conducted to validate the use of the nonlinear term in the model. We compared the reconstruction outcome from the model with or without the nonlinear term. We denoted the model without the nonlinear term as the "linear model". The sHRFs reconstructed from the nonlinear model and the linear models are thus called respectively the "nonlinear sHRF" and the "linear sHRF".

5.3.2.1 Baseline signal used for the simulation

A ten-minute time period of the EEG-fNIRS recording on another one of our epileptic patients (not presented in this paper) was selected as the baseline signal. This "quiet" time period was carefully chosen to avoid any epileptic event or large body movement. Raw fNIRS data were first normalized to unit median, and were then transformed to HbO and HbR concentration changes with the Modified Beer-Lambert Law (MBLL). Simulations were done on both HbO and HbR recordings from 8 emitter-detector pairs (i.e. 8 HbO channels and 8 HbR channels). These pairs were selected with respect to channel length and position (with 2 located over the frontal lobe, 2 over the temporal

lobe, 2 over the parietal lobe and 2 over the occipital lobe). These base channels will be referred to as B_m later on.

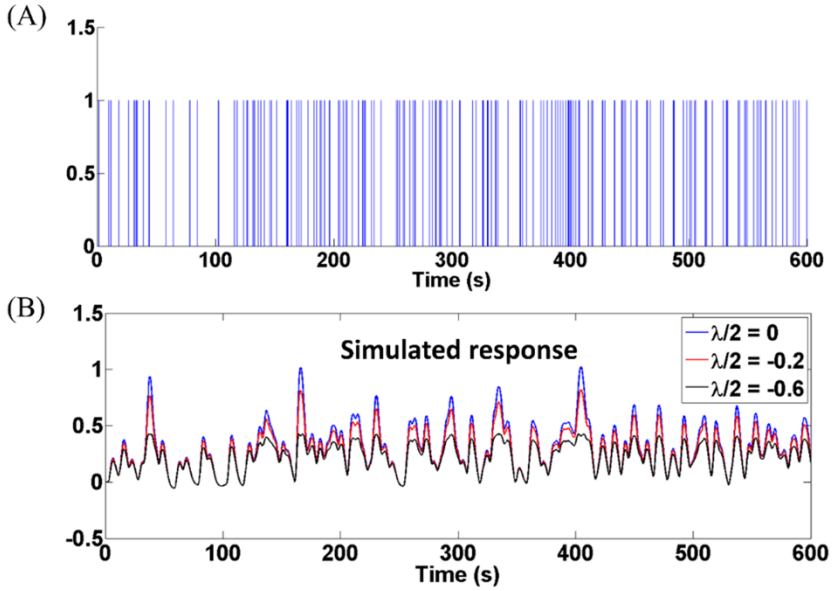

Figure 5.1 (A) Depiction of one random pulse stimulus sequence generated using a Poisson process with incidence rate of 20 per minute (or with expectation of stimulus interval of 3s). (B) Simulated hemodynamic responses of the stimulus sequence with different nonlinear coefficients.

5.3.2.2 Stimulus sequence protocols and simulated signal pre-processing

For each channel, we generated J=100 random pulse stimulus sequences U_j (j=1,2,...,J) using a Poisson process with an incidence rate κ = 20/minute, equivalent to a mean interval of 3s, see Figure 5.1A. The spike sequences were convolved with the SPM8 cHRF (H, normalised to unit area) to calculate first order $V_{1,j}$ and second order $V_{2,j}$ Volterra contributions. Simulated responses $R_j(\lambda)$ were generated by combining the linear and the nonlinear components with different ratio parameters λ, i.e. $R_j(\lambda) = (H \otimes U_j) + (H \otimes U_j)^2\ \lambda/2$, where $\otimes$ denotes the outer product. In our simulation, we varied $\lambda/2$ from 0 to -0.6, which corresponded to a gradual increase of mean nonlinear amplitude from 0 to approximately -30% of the mean linear amplitude in the response, see Figure 5.1B. One spurious response time series $G_j(\lambda)$ for each true simulated response $R_j(\lambda)$ was also produced by constructing ten phase-randomized surrogates of $R_j(\lambda)$ and averaging them. As depicted in Figure 5.2, each set of spurious responses $G_j(\lambda)$ and their true simulated responses $R_j(\lambda)$ were then respectively added to the M=16 baseline signal B_m (m=1,2,...,M) to produce spurious

signals $F_{jm}(\lambda,s) = B_m + \eta_{jm}(s)\, G_j(\lambda)$ or true simulated signals $C_{jm}(\lambda,s) = B_m + \eta_{jm}(s)\, R_j(\lambda)$, where $\eta_{jm}(s)$ is a scalar parameter that controls the SNR (s), for which four levels from -15dB to -2dB were chosen. The SNR was specified as $s = 10\log_{10}(PWR_R/PWR_B)$ where PWR_R is the power of simulated response and PWR_B is the power of the baseline. All the simulated signals C, F were then passed through temporal filters (Huppert et al., 2009) consisting of a high-pass Butterworth infinite response filter of order 4 with cut-off at 0.01 Hz, and a low-pass filter with an SPM8 cHRF shape, as e.g. in Ye et al. (2009).

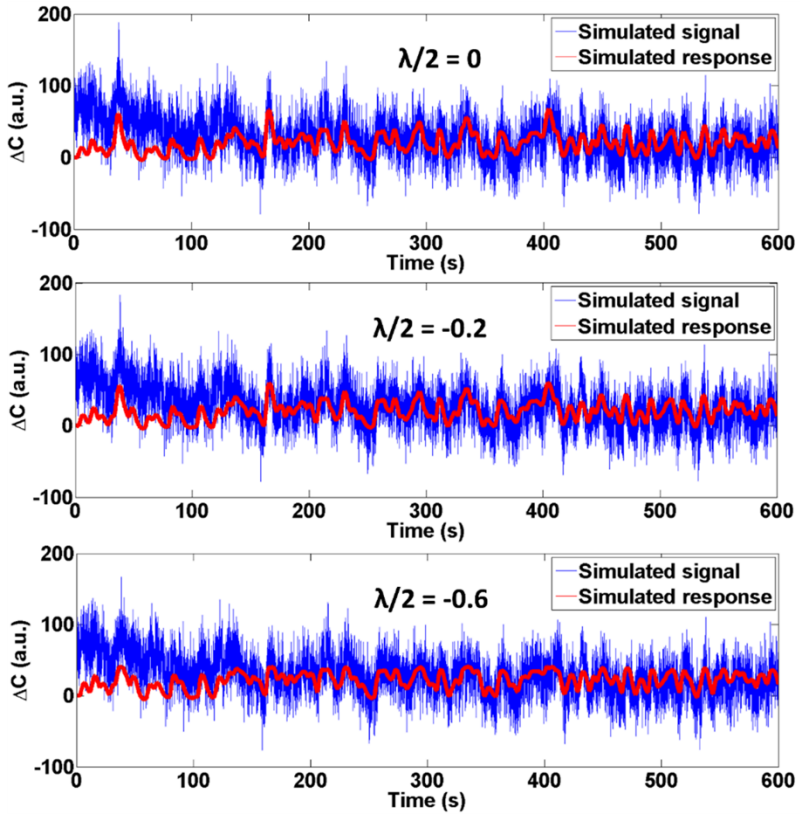

Figure 5.2 Hemodynamic responses computed from Figure 5.1 after adding a same baseline chosen as one typical HbO channel (channel 5) recording from one patient. SNR = -2db.

5.3.2.3 Model validation with simulations

From the filtered simulated signals $C_{jm}(\lambda,s)$ and $F_{jm}(\lambda,s)$, we deconvolved the HRF estimates using the linear model (L) and the nonlinear model (N), producing sHRFs that we labeled $D_{eljm}(\lambda,s)$, e=C,F; l=L,N; j=1,…,J; m=1,...M, respectively. A Gaussian low pass filter with full width at half maximum (FWHM) at 1.5s was applied to all estimated sHRFs to eliminate oscillations originating

from the iterative reconstruction process. HPAs were also calculated for all the sHRFs, denoted correspondingly as $A_{eljm}(\lambda,s)$. Pearson's correlation coefficients $<H,D>$ were first computed between the SPM8 cHRF H and the estimated linear and nonlinear sHRF, $D_{.L..}$ and $D_{.N..}$. These two types of sHRFs were then compared under the HPA criterion, in order to test whether $D_{.N..}$ was able to better account for the nonlinearities in the data than $D_{.L..}$. For each of the M underlying channels, Wilcoxon signed-rank tests were conducted testing the null hypothesis that $A_{.N..}$ was not significantly higher than $A_{.L..}$ (i.e. the nonlinear deconvolution did not perform significantly better than the linear method under the criterion of HPA), Wilcox($A_{.N..}$,$A_{.L..}$). This was done by applying the Wilcoxon test to compare the list of J=100 $A_{eNjm}(\lambda,s)$ to the list of $A_{eLjm}(\lambda,s)$, for true or spurious sHRF e=C,F; each base channels m=1,...,M; each nonlinear coefficient λ (including $\lambda = 0$) and each SNR level s. The resulting p-value $P_{em}(\lambda,s)$ of the test was then calculated.

Finally, we assessed the sensitivity and specificity of using the difference between the HPAs of reconstructed nonlinear sHRFs and linear sHRFs to detect the presence of nonlinearity in a certain channel. This consisted in choosing a nonlinear coefficient λ_0 and an SNR level s_0, collecting the corresponding p-values given by the Wilcoxon tests Wilcox($A_{CN..}$,$A_{CL..}$,) on the ensemble of M channels with ($P_{Cm}(\lambda_0,s_0)$, m=1,…,M) and without nonlinear effects ($P_{Cm}(0,s_0)$, m=1,…,M) respectively, and graphing the receiver operating characteristic (ROC) curves resulting from varying a threshold p_0 among these p-values: true positive rate at λ_0 and s_0, TPR(λ_0,s_0) = proportion of $P_{Cm}(\lambda_0,s_0) < p_0$ (i.e. proportion of the M nonlinear channels correctly recognized), false positive rate at λ_0 and s_0, FPR(λ_0,s_0) = proportion of $P_{Cm}(0,s_0) < p_0$ (i.e. proportion of the M linear channels mistakenly identified as containing nonlinearity).

5.3.3 Epileptic patient data acquisition and analysis

Patients with refractory focal epilepsy were recruited to undergo simultaneous EEG-fNIRS recording at the Optical Imaging Laboratory of Saint-Justine Hospital. The study was approved by the Ethics Committees of Sainte-Justine and Notre-Dame Hospitals and informed consents were obtained from all participants prior to the scan. Besides EEG-fNIRS, a comprehensive neurological evaluation was applied to the patients including ictal single photon computed tomography (iSPECT), positron emission tomography (PET), anatomical brain magnetic resonance imaging (MRI) and magnetoencephalography (MEG). An intracranial EEG study was also performed when needed. The most plausible epileptic focus region was then localized by an epileptologist (DKN)

based on multimodal analysis of clinical, electro-physiological, structural and functional imaging data (Nguyen et al., 2013, 2012).

5.3.3.1 Simultaneous EEG-fNIRS recording

We refer to Nguyen et al. (2012) for a detailed description of our EEG-fNIRS system. In brief, custom helmets adapted to different head sizes were made to mount up to 64 fibered light sources, up to 16 detectors as well as 19 carbon EEG electrodes. Two wavelengths of light were emitted, one more sensitive to HbO (830nm) and the other one more sensitive to HbR (690nm). The detectors were placed 3-5cm away from the sources so that a penetration depth of 1-2cm could be obtained to ensure cortical sensitivity of fNIRS signals (Strangman et al., 2013). The positions of the optical channels were intentionally arranged to cover areas including the whole lobe that contained the most probable epileptic focus, the contralateral lobe, and as much area as possible of the other lobes. FNIRS data was recorded at a frequency of 19.5 Hz using a multi-channel Imagent Tissue Oximeter (ISS Inc., Champaign, IL, USA). With a standard 10-20 layout for electrodes, EEG data were recorded at 500 Hz with a Neuroscan Synamps 2TM system (Compumedics, USA), and were band-pass filtered between 0.1 Hz and 100 Hz to remove instrumental noise and other artificial disturbances. For each patient, multiple consecutive EEG-fNIRS sessions of typically 15 min each were usually recorded. During the recordings, the patient was simply asked to sit comfortably and relax.

5.3.3.2 Data Pre-processing and HRF reconstruction

Epileptic events such as IEDs and seizures were marked offline on the EEG traces using Analyzer 2.0 (Brain Products GmbH, Germany) by certified clinical neurophysiologists and reviewed by an epileptologist (DKN). For some patients, recorded IEDs were classified into distinct types regarding the location where they took place, e.g. left temporal IEDs and right temporal IEDs for a patient suffering from bi-temporal lobe epilepsy. FNIRS data was processed with our home-made Matlab (MathWorks, USA) toolbox, nirs10, based on SPM8 (Friston et al., 2007) and NIRS-SPM (Jang et al., 2009; Ye et al., 2009). Optical channels with length greater than 6cm or a standard deviation of more than 10% of the mean were excluded (Nguyen et al., 2013, 2012). Hemoglobin concentration changes were calculated from light attenuation data for the remaining channels with the MBLL. A filter based on principal component analysis (PCA) was then applied by setting to zero the largest eigenvalue in the decomposition over all channels (Peng et al., 2014). Besides the

PCA filter, temporal filtering was also applied on HbO and HbR data with the same filters introduced in section 5.2.2.2. HbT changes were obtained by a direct summation of HbO and HbR changes (HbT = HbO + HbR).

A time period was selected conservatively for each patient by a careful visual inspection on his/her EEG recordings. This period was a time interval between 2 and 15 minutes (depending on patients and sessions) during which the patient only had frequent IEDs but no other epileptic event or large body movement. The reconstruction of sHRFs of each channel as well as further statistical analysis (described below in section 2.3.3) was conducted only on these chosen "clean" periods. The sHRFs were then passed to the same Gaussian low pass filter as described in section 5.2.2.3.

5.3.3.3 Statistical parametric mapping with patient-specific sHRFs

Hemoglobin concentration changes for each channel were fitted with three different GLMs. These GLMs contained a design matrix consisting of a constant regressor, a heart rate regressor, and a distinct IED regressor which was obtained respectively using the SPM8 cHRF, linear sHRFs and nonlinear sHRFs. The IED regressor was either formulated by the convolution of IED onsets with the SPM8 cHRF in the first case, or was obtained by averaging the expected HbO responses of IEDs from three selected channels in the other two cases, with linear or nonlinear sHRFs. For each patient, we selected three HbO channels that showed highest HPAs for both linear sHRFs and nonlinear sHRFs. To be selected, a channel was also required to be located on the ipsilateral hemisphere to the epileptic focus and the HPAs of both types of sHRFs had to exceed the 95% threshold from the surrogate method (refer to section 2.1.2).

Two-tailed 2D t-statistic maps (t-maps) were obtained with inhomogeneous interpolation kernels (Ye et al., 2009) for the IED regressor of each GLM, testing the null hypothesis that the hemoglobin concentration (HbO/HbR/HbT) did not change with the presence of IEDs. The patient-level results were then corrected against false positives using the Euler Characteristic (EC) correction (Li et al., 2012), assuming a p-value of 0.05. T-maps of each GLM were presented in four views (left, right, frontal and dorsal). The most plausible epileptic focus region of the patient was represented as a 30mm radius sphere around the epicenter of each patient, and was also projected onto the four 2D views.

5.4 Results

5.4.1 Simulation results

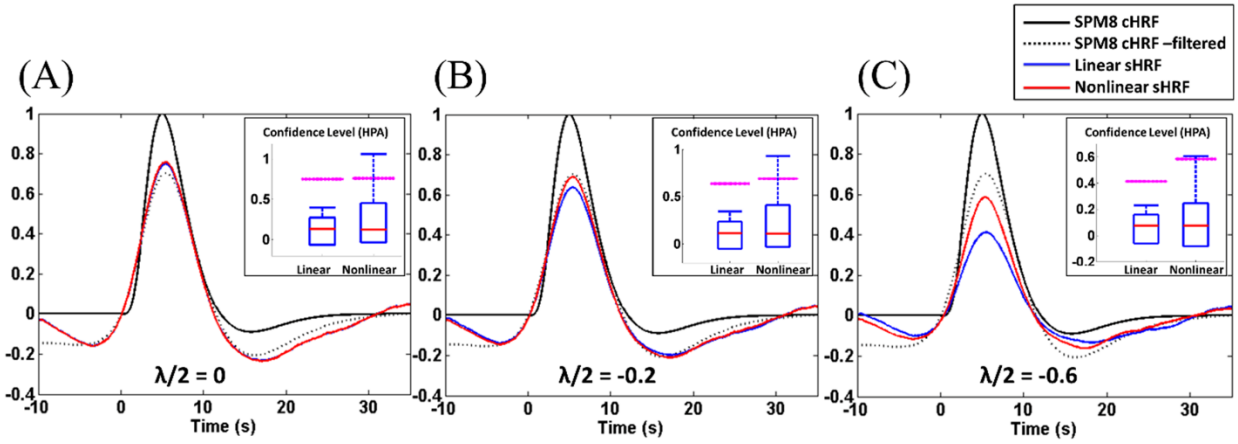

Figure 5.3 Reconstructed linear sHRFs and nonlinear sHRFs in one simulation. HbO channel 5 was used as baseline. Stimulus sequence protocol and simulated signals were shown in Figure 5.1 and in Figure 5.2. The original SPM8 cHRF as well as the filtered SPM8 cHRF are also plotted for comparison. Nonlinear coefficient λ/2 = (A) 0; (B) -0.2; (C) -0.6. Confidence levels ($p<0.05$) for HPA were calculated using the surrogate series method.

Figure 5.3 shows the deconvolved sHRFs of one simulation (channel 5, SNR = -2dB, stimulus sequence and simulated signals were depicted in Figure 5.1 and Figure 5.2). All sHRFs in Figure 5.3 were normalized so that the SPM8 cHRF had unit HPA. The filtered SPM8 cHRF was produced by simply passing the SPM8 cHRF through the same spatial filters that were applied to the simulated signals. It can be seen from Figure 5.3 that both the linear sHRFs and the nonlinear sHRFs retained properties of the SPM8 cHRF such as peaking time and undershoot time. When no nonlinear effect was induced in the signal, the shape of the nonlinear sHRF overlapped quite well with the linear sHRF. The nonlinear sHRF showed its advantage in better retaining the peak amplitude (i.e. the HPA) of the true HRF when a relatively large amount of nonlinear effects was present in the data.

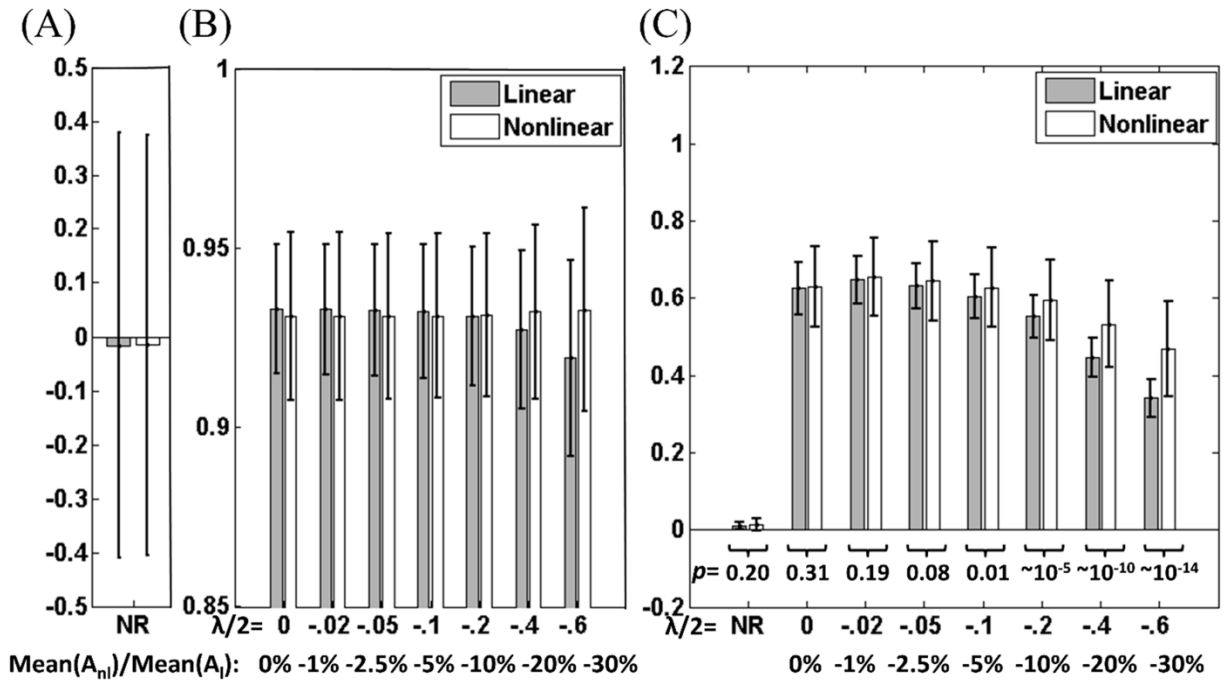

Figure 5.4 Simulation results with constant SNR = -2dB and varying nonlinear coefficient λ/2 from 0 to -0.6: (A) Mean value and standard deviation of the Pearson's correlation coefficients between the true HRF and either the reconstructed linear or nonlinear sHRFs from channels without true response (NR) and (B) with responses at different nonlinear coefficients. (C) Mean value and standard deviation of HPAs of linear sHRFs and nonlinear sHRFs, also for channels without true response (NR) and with responses at different nonlinear coefficients. HPAs have been normalized as explained in the text. P-values from Wilcoxon signed-rank test were averaged over 16 channels and displayed for HPA comparison.

Next, we explored the correlation and HPA between the SPM8 cHRF and the reconstructed sHRFs. We first maintained a constant SNR = -2dB in the simulation (Figure 5.4), and then a constant nonlinear coefficient $\lambda/2$ = -0.2 (Figure 5.5). At each choice of SNR and λ, the HbO and HbR channels for the different random IED sequences (1600 time series) were pooled because of their correlations and HPAs were quite similar. At SNR = -2dB, channels that did not contain any true response were easily distinguished as most of the HPAs were within the range of -0.1 to 0.1 (Figure 5.4A). When a real simulated response was included in the data but with no or small amount of nonlinearity ($\lambda/2$ from 0 to -0.05, corresponding to a mean nonlinear to linear amplitude ratio from 0 to -2.5% over the 100 stimulus protocols), both the linear sHRFs and the nonlinear sHRFs provided excellent estimates of the true HRF, reflected by the large correlation coefficients of more

than 0.9. In these cases, the differences in the HPAs of the nonlinear sHRFs and the linear sHRFs were insufficient to reject the null hypothesis for most of the channels, suggesting comparable performance of the nonlinear model with the linear one (Figure 5.4B). As the nonlinear effect became more dominant ($\lambda/2$ from -0.1 to -0.6, mean nonlinear to linear amplitude ratio from -5% to -30%), a slight decrease in the correlation coefficients for linear sHRFs was noticed, together with an increase for nonlinear sHRFs. The loss in HPAs of the linear sHRFs was seen to be much greater than that of the nonlinear sHRFs. The null hypothesis of the Wilcoxon signed-rank test was also rejected at 0.05 for most of the channels, indicating that the HPAs of the nonlinear sHRFs were significantly higher than those of linear sHRFs (Figure 5.4C). However, the overall correlation for both types of sHRF estimates was still high (>0.85).

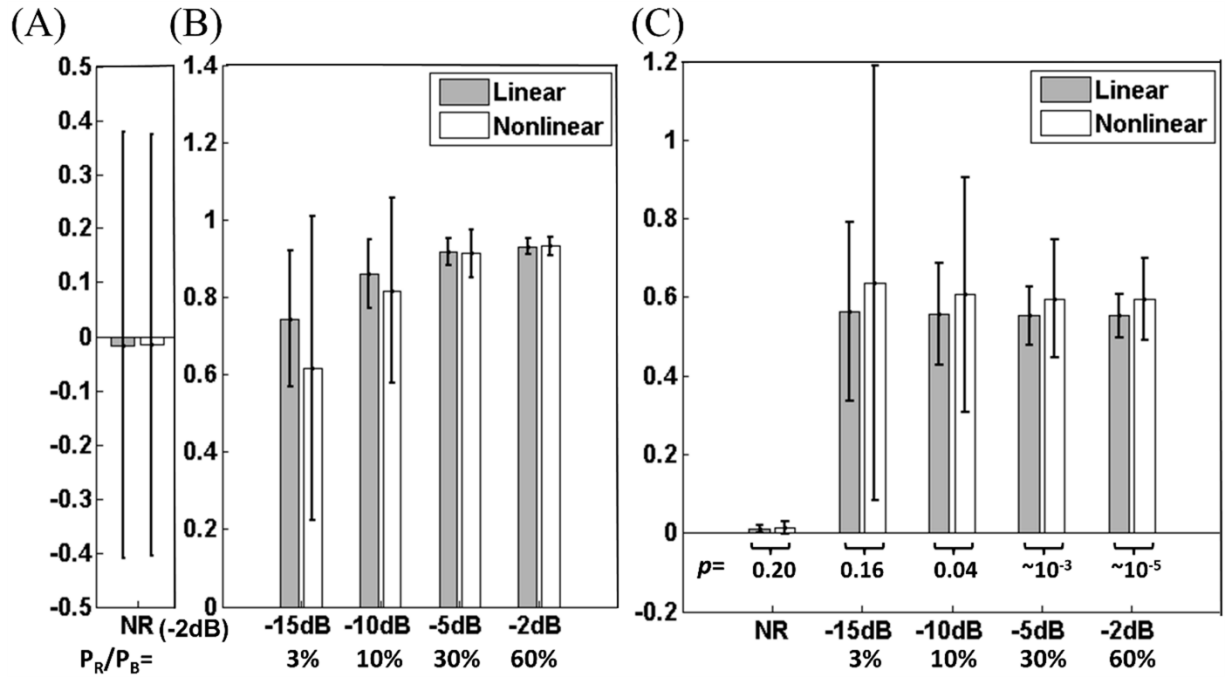

Figure 5.5 Results from similar simulations as in Fig. 4 but this time with constant nonlinear coefficient $\lambda/2 = -0.2$ and varying SNR from -15dB to -2dB.

The impact of the SNR on the sHRF reconstruction can be clearly seen in Figure 5.5, where the SNR was varied from -15dB to -2dB and the nonlinear coefficient was maintained constant. With the SNR decreasing to -15dB, while the mean correlation between the true HRF and the estimated sHRFs was still at a moderate level (>0.6), the correlations dropped dramatically in some

simulations which implied a severe misspecification of the sHRF model (Figure 5.5A). The HPAs also tended to be more stable with increasing SNR, especially for nonlinear sHRFs (Figure 5.5B).

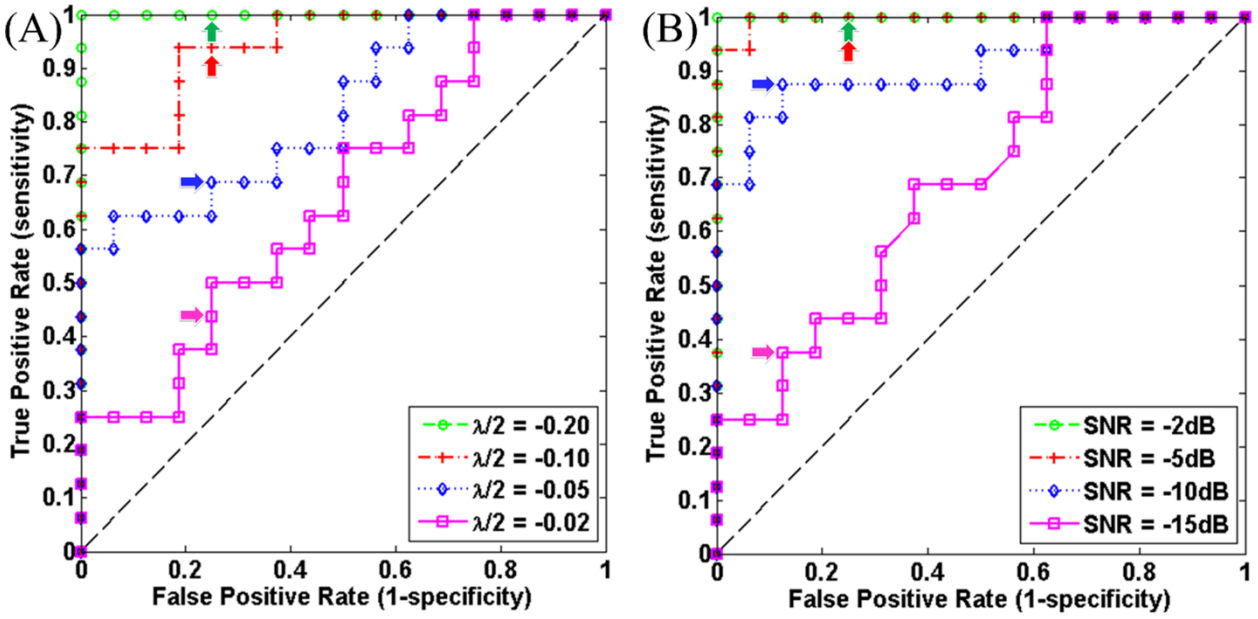

Figure 5.6 Simulation results: detectability of nonlinearity using the nonlinear algorithm under the HPA criterion. (A) ROC curves for using the significance of HPA difference (p-value) of linear sHRFs and nonlinear sHRFs to detect nonlinear channels. SNR was fixed at -2dB. ROC curves at a $\lambda/2$ more negative than -0.2 (e.g. -0.4 or -0.6) maintained a same shape as that at $\lambda/2 = -0.2$. The arrows indicate a threshold of $p = 0.05$ on each ROC curve. (B) ROC curves of nonlinearity detection of channels at different SNRs with $\lambda/2 = -0.2$.

These findings were supported by the ROC measures plotted in Figure 5.6, where the detectability of nonlinear channels using HPA was seen to be better with a larger nonlinear coefficient or with a higher SNR. For example, at a nonlinear coefficient of $\lambda/2 = -0.2$ and a threshold of $p = 0.05$, the detection sensitivity increased from around 0.4 to 0.9 with the improvement of SNR from -15dB to -10dB, while the specificity remained unchanged (at about 0.9, see the magenta arrow and the blue arrow in Figure 5.6B), i.e. at SNR = -10dB, 14/16 nonlinear channels and 12/16 linear channels were successfully identified under $p = 0.05$. The sensitivity and the specificity were generally poor in those cases where $\lambda/2$ was between 0 and -0.02 (mean nonlinear amplitude ratio $\leq 1\%$, area under curve $\leq 66\%$ in Figure 5.6A) or the SNR was smaller than -15dB (area under curve $\leq 70\%$ in Figure 5.6B).

5.4.2 Patient results

Five patients with refractory focal epilepsy were selected on the basis of unambiguous focus localization and frequent and clear IEDs. Focus localization was established by multimodal evaluation and confirmed by seizure-freedom following epilepsy surgery with a follow-up of more than a year. Table 5.1 lists the most plausible focus region, the length of selected recording time period as well as the frequency of recorded IEDs for each of the five patients. In the following sub-sections, two case studies representative of overall results are presented. The readers are referred to Appendix B for the results on the other three patients.

Table 5.1 Types and numbers of IEDs observed on EEG for the five selected patients.

Patient #	**1**	**2**	**3**	**4**	**5**
Focus region	R F (IFG)	L O (MOG)	R OrbitoF, R aINS	R T (ITG)	R TO
IED location on EEG	R F	L TO	R FT	R T, R FT	R POT biPOT
Total data length (min)	60	45	60	82.5	45
Total IED number – Total	1541	1157	494	1196	1507
Mean IED interval (s) – Total	2.3	2.3	7.3	4.0	1.8
Median IED interval (a) – Total	1.3	1.3	4.0	0.5	0.9
STD of IED intervals (s) - Total	3.6	5.4	10.3	9.5	2.1
Sample data length (s)	654	180	221	230	133
Total IED number – Sample	164	51	34	123	56
Mean IED interval (s) - Sample	4.0	3.6	5.6	1.9	2.0
Median IED interval (s) - Sample	3.0	2.6	4.6	0.5	0.9
STD of IED intervals (s) - Sample	3.6	3.4	4.9	4.1	2.2
• IED interval less than 1s (%)	12	14	12	67	51
• IED interval between 1s to 5s (%)	63	52	48	21	40
• IED interval greater than 10s (%)	8	4	24	3	0

Abbreviations: STD, standard deviation; L, left; R, right; F, frontal; T, temporal; P, parietal; O, occipital; IFG, inferior frontal gyrus; MOG, middle occipital gyrus; OrbitoF, orbitofrontal; aINS, anterior insula; ITG, inferior temporal gyrus; bi, bilateral.

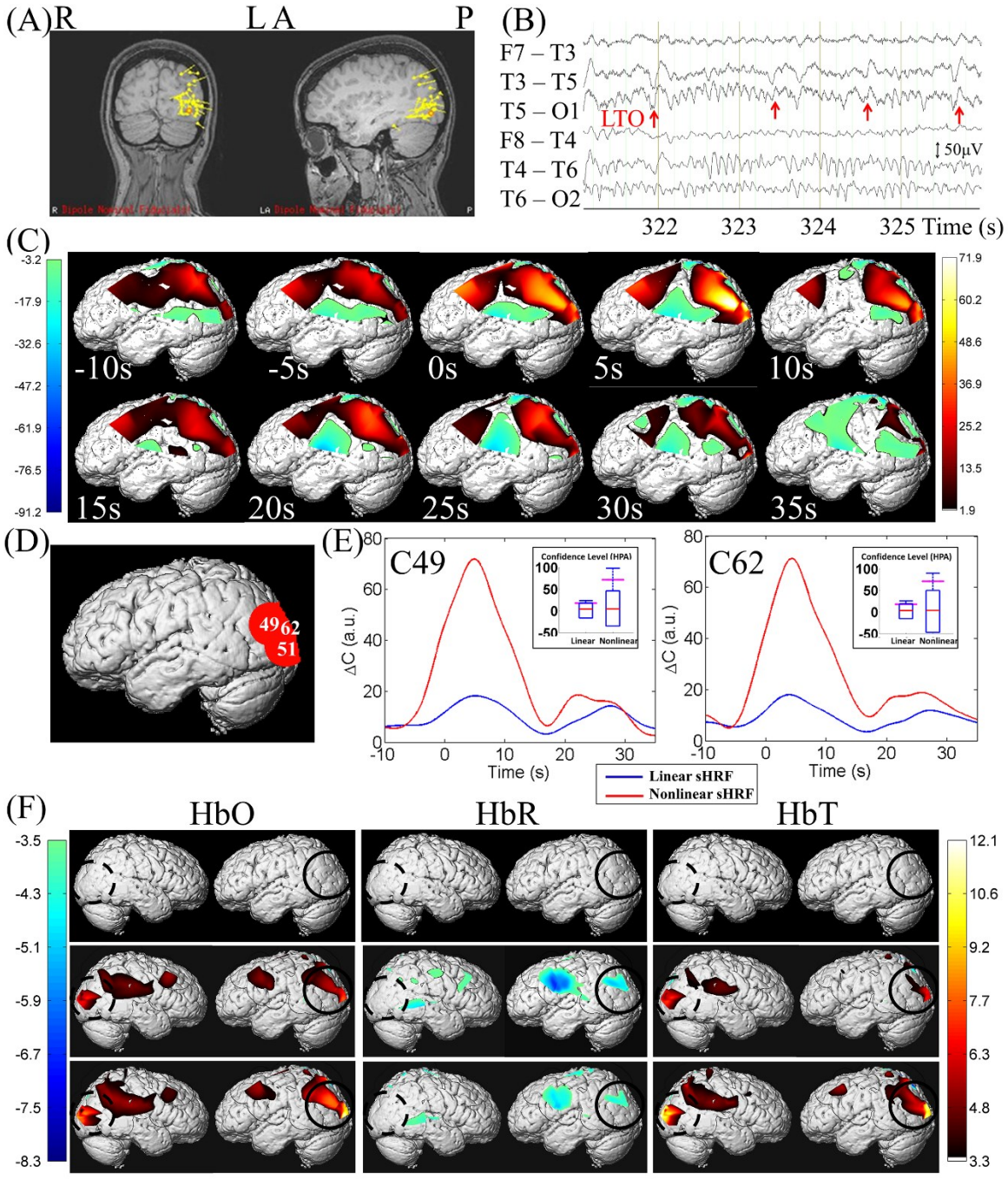

Figure 5.7 Patient 2. (A) MEG dipole localization of IEDs revealing a cluster of sources located in the left middle occipital gyrus; (B) EEG fragment with marking for left tempo-occipital IEDs; (C) Interpolated maps of nonlinear sHRFs, from 10s before an IED to 35s after the IED (left view); (D) The covered brain areas of the three selected ipsilateral channels with highest HPAs; (E) The reconstructed linear sHRF and nonlinear sHRF of channel 49 and 62. Compared with linear sHRFs, the first peak of the nonlinear sHRFs was greatly enhanced. Confidence levels of each deconvolved sHRF were presented using the surrogate method; (F) T-statistical maps of HbO, HbR and HbT response to left tempo-occipital IEDs, generated from GLMs using respectively the SPM8 canonical HRF (the first row), linear sHRFs (the second row) and nonlinear sHRFs (the third row). T-maps were EC-corrected, $p<0.05$. Solid black circle (30mm radius) indicates the projected most plausible focus region; dotted black circle shows the contralateral region corresponding to focus.

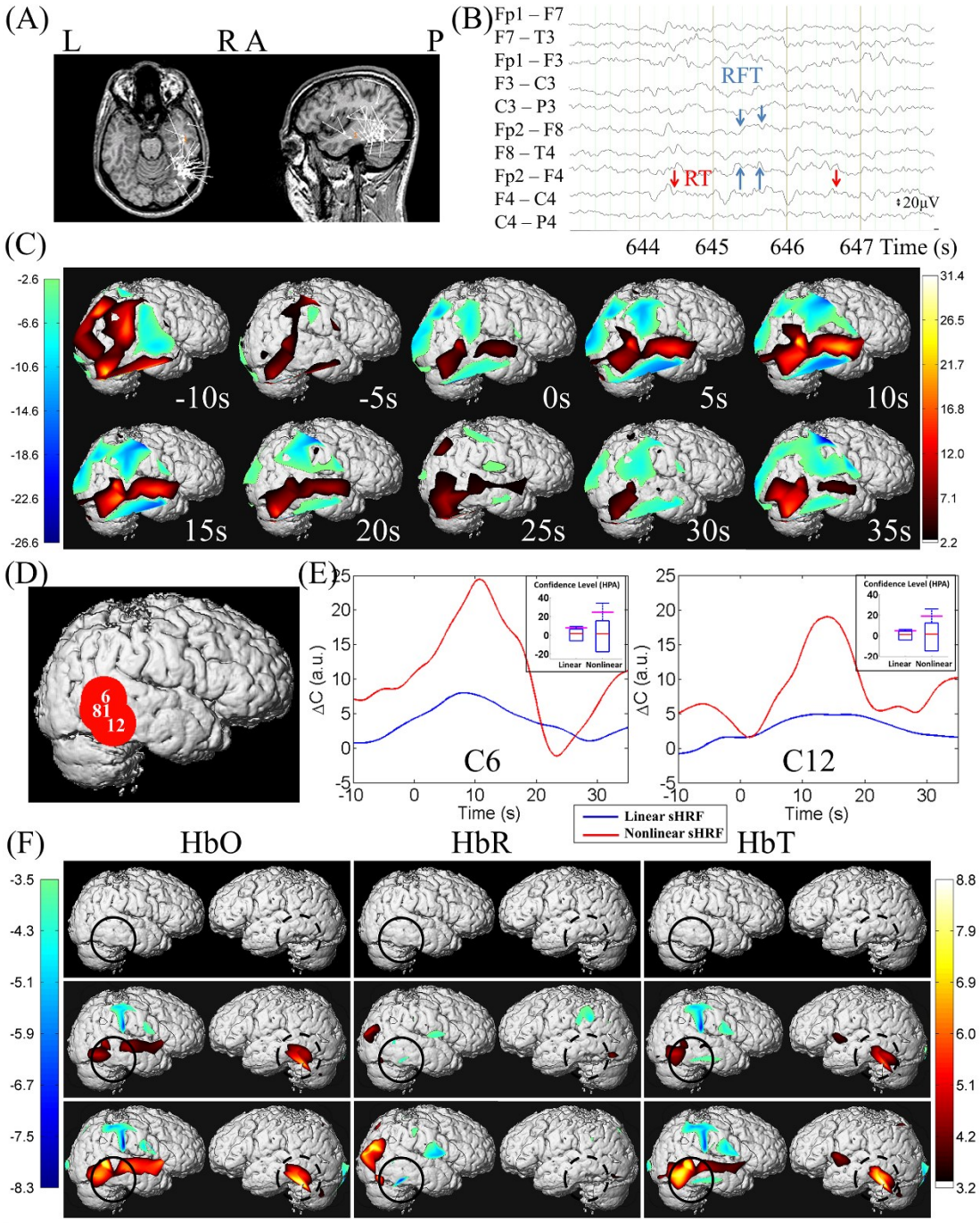

Figure 5.8 Patient 4. (A) MEG dipole localization of IEDs revealing a cluster of sources located in the posterior portion of inferior temporal gyrus; (B) EEG fragment with marking for right temporal IEDs and right fronto-temporal IEDs; (C) Interpolated maps of nonlinear sHRFs, from 10s before an IED to 35s after the IED (right view); (D) The covered brain areas of the three selected ipsilateral channels with highest HPAs; (E) The reconstructed linear sHRF and nonlinear sHRF of channel 6 and 12. Nonlinear sHRFs clearly showed higher HPAs. Both the linear and the nonlinear sHRFs peaked later than the cHRF, at around 12s; (F) T-statistical maps of HbO, HbR and HbT response to IEDs combined from right temporal IEDs and right fronto-temporal IEDs, generated from GLMs using respectively the SPM8 canonical HRF (the first row), linear sHRFs (the second row) and nonlinear sHRFs (the third row). T-maps were EC-corrected, $p<0.05$. Solid black circle (30mm radius) indicates the projected most plausible focus region; dotted black circle shows the contralateral region corresponding to focus.

5.4.2.1 Case study - Patient 2

This 19 year-old girl with tuberous sclerosis suffered from drug-refractory epilepsy since age 14. Presurgical multimodal investigations localized her epileptic focus to the left middle occipital gyrus (Figure 5.7A, 5.7B).

On the left view maps of interpolated nonlinear sHRFs (Figure 5.7C), the first positive peak of HbO arrived near 5s after an IED, and had the highest amplitude in the left middle occipital regions. A simultaneous HbO increase in posterior frontal area was also noticed (Figure 5.7D). The linear sHRFs and nonlinear sHRFs of the three selected channels (49, 62 and 51) are depicted in Fig. 7E. Two peaks with comparable amplitudes and durations were present in the plotted linear sHRFs, one peaking at about 5s and the other near 27s. In the nonlinear sHRFs however, while the peak value of the second peak remained more or less unchanged, the amplitude of the first peak was greatly enhanced. We were then able to recognize the first peak as the main response to IEDs.

T-statistical maps generated using SPM8 cHRF, linear sHRFs and nonlinear sHRFs are shown in Figure 5.7F. No activation was seen for HbO, HbR and HbT on t-maps with the cHRF. On the other hand, significant increases in HbO and in HbT as well as a decrease in HbR were observed inside the focus circle on t-maps generated with either linear or nonlinear sHRFs, leading to a positive sensitivity of all hemoglobin types. The peak t-value of the activation at the focus site was higher with nonlinear sHRFs than with linear ones for HbO (nonlinear/linear: 11.6/7.8) and HbT (11.3/6.7), but was slightly lower in absolute value for HbR (-4.5/-5.2). Activations distant from the focus site were also discovered with sHRFs, such as in the contralateral occipital lobe (for HbO and HbT), or left posterior frontal areas.

5.4.2.2 Case study - Patient 4

This 17 year-old man suffered from daily pharmacoresistant seizures related to a cavernoma in the posterior portion of the right inferior temporal gyrus (Figure 5.8A). Two types of IEDs were recorded from 230s of selected time period: 62 right temporal IEDs and 61 right temporo-frontal IEDs (Figure 5.8B). These two types of IEDs were combined in sHRF reconstruction due to their spatial contiguity seen on EEG. From interpolated maps of nonlinear HbO sHRFs, large increases peaking at around 11s were observed in posterior temporal areas, anterior portion of temporal lobe, as well as a part of the inferior frontal gyrus (Figure 5.8C). Three channels (6, 81 and 12) located in the posterior temporal lobe were selected (Figure 5.8D, 5.8E). Two channels located in the

anterior temporal region were excluded in the selection (despite the high HPAs) because of their abnormally large mean square errors (MSE) when fitted with the nonlinear sHRFs.

As seen in Figure 5.8F, we were unable to locate any significant activation on the contrast maps generated with cHRF. The detection ability was improved with linear sHRFs, thanks to significant HbO and HbT increases as well as an HbR decrease in the bilateral posterior temporal areas and in central regions. However, in this case, the activations observed on the side contralateral to the focus region (peak t-values for HbO/HbR/HbT: 6.7/-4.7/6.1) were stronger than those on the ipsilateral side (peak t-values: 4.8/-4.6/4.9). On contrast maps generated with nonlinear sHRFs, much higher t-scores and larger extent were estimated for the detected activations, especially on the side ipsilateral to the focus (peak t-values: 7.9/-6.8/7.9).

5.4.3 Summary of patient results

For the five patients, the markings as well as the peak t-scores that were congruent with the focus region are depicted in Table 5.2. For all the patients, the improvement on detection was seen when the cHRF was replaced by the sHRFs. The nonlinear sHRFs generally had the best performance among the three HRF models especially on HbO and HbT.

In Table 5.2 and in Figure 5.9, we further explored the scale of nonlinear effect in the hemodynamic response to IEDs by presenting the estimated nonlinear coefficients and the temporal-averaged amplitudes of the reconstructed first-order component (i.e. V1 as defined in section 5.3.1.1) and second-order component (V2) of channels. For more accurate localization of the nonlinear effects, we reconstructed the V1 response and the V2 response only on channels that had a high t-statistic score in the previous GLM analysis using nonlinear sHRFs. The Bonferroni threshold was applied to the channel t-values to yield a corrected p value of 0.05. It was consistently seen for the five patients that the V2 response had amplitude of the opposite sign than the corresponding V1 response, which suggested inhibitive nonlinear effect in patient data. Furthermore, the V2 response was also discovered to be of comparable order of magnitude to the V1 response. In most of the cases (except patient #4), the degree of suppression varied within the range of 0.1 to 0.5 relative to the highest mean V1 amplitude (or 10% to 90% relative to the corresponding V1 mean amplitude). These findings were in good agreement with our previous nonlinear study (Pouliot et al., 2012).

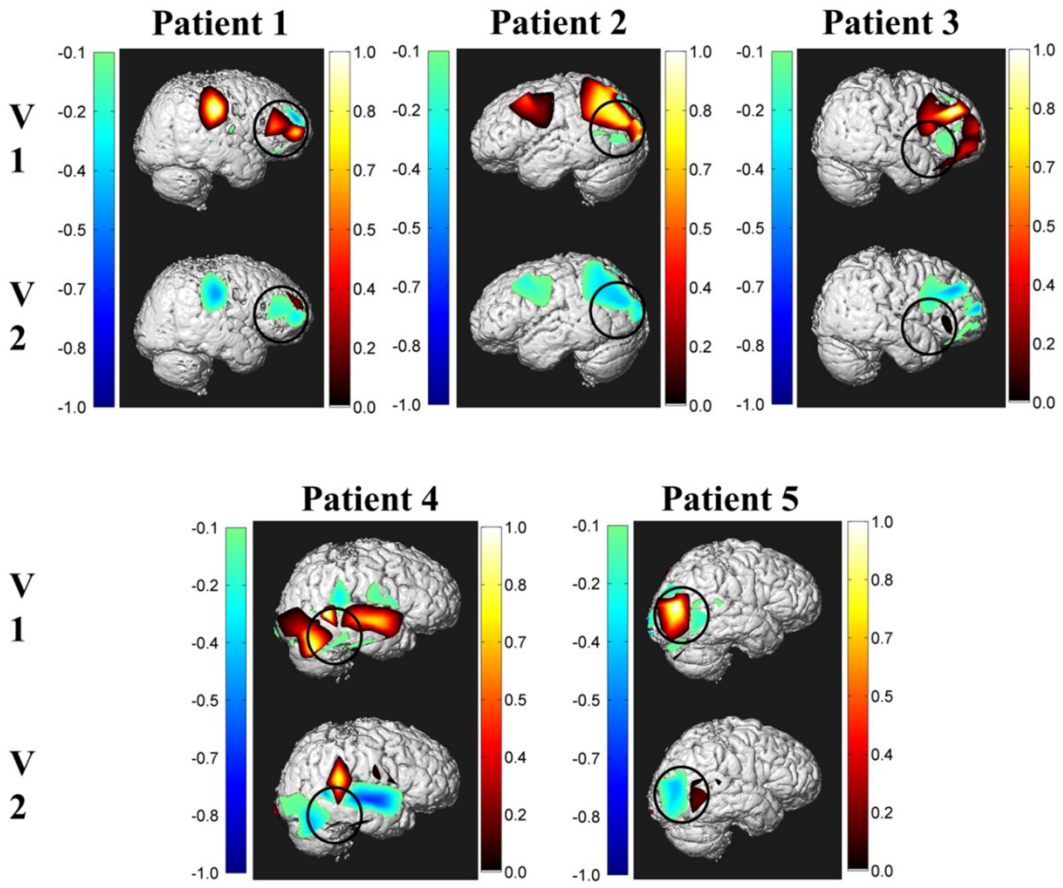

Figure 5.9 Ipsilateral hemisphere of the epileptic focus (circled in black) for the 5 patients: depiction of the first order Volterra component (the linear term, V1) and the second order Volterra component (the nonlinear term, V2) in the expected HbO response reconstructed using the nonlinear sHRFs. Only channels that presented significant nonlinear activations were chosen for interpolation (Bonferroni threshold). For each selected channel, the mean amplitudes of the V1 term and of the V2 term in the expected response were calculated. For illustration purposes, the mean V1 amplitudes and the mean V2 amplitudes of a patient were both normalized so that the highest mean V1 amplitude had a unit value.

Table 5.2 Summary of patient results. Hemodynamic response congruent with focus: location and peak *t*-statistic value. An up arrow ↑ (down arrow ↓) indicates that an increase (resp. a decrease) in the hemoglobin concentration was observed in the corresponding locations, while a double arrow sign ↑↑ or ↓↓ indicates that the given activation was recognized as being the most significant among all the activations of the same hemoglobin type on the current set of contrast maps. The distribution of nonlinear coefficients ($\lambda/2$) and ratios of mean nonlinear to linear amplitudes (A_{nl}/A_l) is described using median value and median absolute deviation (MAD) to mitigate the influence of outlier channels. The negative sign of $\lambda/2$ and A_{nl}/A_l indicated an inhibitory effect of nonlinear components to linear components in the response.

#	Focus	H	Hemodynamic Response (SPM8 cHRF)	Hemodynamic Response (Linear sHRF)	Hemodynamic Response (Nonlinear sHRF)	$\lambda/2$ (median ± MAD)	A_{nl}/A_l (median ± MAD)
1	R F (IFG)	HbO	↑↑ R F (MFG): 4.0	↑↑ R F (MFG+IFG): 4.8	↑↑ R F (MFG+IFG): 5.7	-0.57 ± 0.26	-0.67 ± 0.30
		HbR	↓ R F (IFG): -4.2	↓ R F (IFG): -4.5	↓ R F (IFG): -5.2	-0.49 ± 0.40	-0.27 ± 0.57
		HbT	↑↑ R F (MFG): 4.3	↑↑ R F (MFG): 4.4	↑↑ R F (MFG): 4.9	-0.39 ± 0.19	-0.80 ± 0.38
2	L O (MOG)	HbO		↑↑ L O (MOG): 7.8	↑↑ L O (MOG): 11.6	-1.18 ± 0.21	-0.36 ± 0.07
		HbR		↓ L O (MOG): -5.2	↓ L O (MOG): -4.5	-0.95 ± 0.41	-0.29 ± 0.13
		HbT		↑↑ L O (MOG): 6.7	↑↑ L O (MOG): 11.3	-1.29 ± 0.14	-0.40 ± 0.05
3	R OrbitoF R aINS	HbO	↑ R F (IFG): 3.8	↑ R F (IFG): 3.9	↑ R F (IFG): 4.8	-0.92 ± 0.43	-0.41 ± 0.27
		HbR					
		HbT	↑ R F (IFG): 4.2	↑ R F (IFG): 3.6	↑ R F (IFG): 4.6	-0.65 ± 0.31	-0.61 ± 0.89
4	R T (ITG)	HbO		↑ R posT: +4.8	↑↑ R posT: +7.9	-0.73 ± 0.30	-0.50 ± 0.25
		HbR		↓ R T (ITG): -4.6	↓↓ R T (ITG): -6.8	-0.39 ± 0.19	-0.50 ± 0.18
		HbT		↑ R posT: +4.9	↑↑ R posT: +7.9	-0.67 ± 0.40	-0.63 ± 0.22
5	R TO	HbO	↓ R O: -4.3	↑↑ R O, R posT: 17.3	↑↑ R O, R posT: 19.3	-0.57 ± 0.50	-0.40 ± 0.27
		HbR	↓ R O: -4.2	↓↓ R O, R posT: -16.6	↓↓ R O, R posT: -16.0	-0.84 ± 0.40	-0.41 ± 0.16
		HbT	↓ R O: -4.1	↑↑ R O, R posT: 12.6	↑↑ R O, R posT: 13.3	-0.55 ± 0.47	-0.34 ± 0.28

Abbreviations: L, left; R, right; F, frontal; T, temporal; P, parietal; O, occipital; IFG, inferior frontal gyrus; MFG, middle frontal gyrus; MOG, middle occipital gyrus; OrbitoF, orbitofrontal; aINS, anterior insula; ITG, inferior temporal gyrus; posT, posterior temporal lobe.

5.5 Discussion

To the best of our knowledge, this work is the first to make an effort to model the HRF variability in epilepsy with fNIRS data. Besides the linear method, a nonlinear deconvolution approach using Volterra series was proposed for patients with frequent IEDs. This allowed also for the first time more precise HRF modelling in epilepsy with compensation for first order nonlinearity. The sHRF was reconstructed over a time interval from 10 seconds before a stimulus (an IED) to 35 seconds after the stimulus in the hope of capturing most of the characteristics of the hemodynamic response in the data. A constant term and a linear trend term were also added in the model.

In the first part consisting of model validation, simulation results have shown that the deconvolution method yielded reasonable results in reconstructing the HRF under appropriate conditions. The second part of the work focused on using the sHRF models on real epileptic data with frequent IEDs. As fNIRS depth is insufficient for epileptiform activity arising from deeper cortical structures (Obrig, 2014; Peng et al., 2014; Steinhoff et al., 1996), we selected five patients with only neocortical epilepsies. Results confirmed that the specific HRFs were significantly different from the cHRF in both shape and latency. Higher HPAs were derived using nonlinear sHRFs, especially from channels sampling near the epileptic focus site. Compared with cHRF, using sHRFs (especially the nonlinear sHRFs) in the GLM analysis not only greatly improved the statistical significance of detected activations on all of our five patients, but also located new activated areas which were unable to be detected with the cHRF at the same threshold of significance.

5.5.1 Criteria for sHRF comparison

In the GLM analysis using sHRFs, the IED regressor was constructed by averaging the fitted responses of three distinct HbO channels. The purpose of the averaging was to enhance the robustness of the algorithm by mitigating the influence of false positives. Tests were conducted to ensure that choosing three channels was reasonable (results not shown here). Previous combined EEG-fMRI studies selected active voxels based on criteria including the concordance of voxel location with the spike field on EEG (Jacobs et al., 2009), the statistical significance of an activation in pre-conducted GLM analysis using the cHRF (Storti et al., 2013), or a combination of the two (Masterton et al., 2010). In our case, we opted to be as unbiased as possible by including

significant activity that might be distant from the irritative zone. Moreover, it was also noticed that for some of our patients, no significant response was detected with the conventional GLM (e.g. Figure 5.7F, Figure 5.8F). Hence, in this work, we constrained the selected channels to be on the ipsilateral side of the spike field, while comparing sHRFs mainly on the criteria of HPA and peak latency (Richter and Richter, 2003; Watanabe et al., 2014). The HPA was chosen as an indicator over other characteristics such as the area under curve (AUC) of the sHRF, mainly because using HPA was more accurate and specific in detecting nonlinear channels at low SNRs (see the Appendix section, Figure 5.13).

5.5.2 HbO vs. HbR

In this work, we decided to use the sHRFs for HbO to construct the design matrix in the GLM for all three types of chromophores, mainly because the sHRF for HbO was usually able to present a clear first peak within 0 to 15s that was able to be recognized as the main response to IEDs. By contrast, for four of our five patients (except patient 5), the shapes of the deconvolved sHRFs for HbR were less distinguishable from background noise and were more difficult to interpret. This difference between sHRFs for HbO and for HbR might be due to the fact that a much smaller SNR is often seen in the NIRS measurement of HbR relative to HbO, as reported in other NIRS studies (Ding et al., 2014; Schaeffer et al., 2014). The lower SNR might increase the variability of sHRF shape (see Fig. 4B) which made sHRFs for HbR less reliable to reflect the aspects of the true hemodynamic response. On the other hand, it is also worth noting that despite the use of sHRFs for HbO in GLM analysis, the statistical significance of HbR response and HbT response were still improved in most of the cases. However, it may be that including the chromophore-specific sHRF with a correctly-specified shape in the GLM analysis can further improve the statistical scores of HbR and HbT responses.

5.5.3 Localization of the epileptic focus

We assessed the accuracy of focus localization using different HRF models by examining the overlap between the projected focus region and the detected activation locations on each set of contrast maps. As in Peng et al. (2014), we defined the localization sensitivity to be positive for a patient if the epileptic focus region overlapped a non-inverted significant hemodynamic response. A positive specificity was assigned if the hemodynamic change in the focus region was the most

significant (i.e. held a highest t-score) among all the detected clusters, and thus would lead to a successful identification of the epileptic focus region. On the contrast maps generated with the SPM8 cHRF, we were only able to report positive localization sensitivity on two of the five patients (patient #1, #3) and positive localization specificity on one patient (patient #1) using HbO. The localization sensitivity and specificity were improved with sHRF models. For example, the localization sensitivity for HbO was observed to be positive on all the five patients with either of the two sHRF models, while the localization specificity for HbO was positive on three patients with the linear model and on four patients with the nonlinear model. The detailed localization results with all three types of chromophores are listed in the Appendix, Table 5.3.

5.5.4 Early response preceding IEDs

Early hemodynamic response preceding epileptic events has been reported in focal epilepsy with multiple types of imaging modalities (Hawco et al., 2007; Mäkiranta et al., 2005; Moeller et al., 2008; Osharina et al., 2010; Zhao et al., 2007). The localizing value of these early signals was also well discussed by the Montreal Neurological Institute's group (Jacobs et al., 2009; Pittau et al., 2011; Rathakrishnan et al., 2010). In this EEG-fNIRS study, we observed on some patients that at least a part of the first HbO peak was earlier than the IED event marked on EEG (patients #2, #3 and #5). Moreover, the deconvolved sHRF might be able to provide a more direct view on the early phase of a response. For example, for patient #2, the significant HbO increase near the left middle occipital gyrus (which was recognized as the response to IEDs) was clearly shown to occur from approximately 5 seconds preceding the IEDs (Fig. 7(D) (F)). However, we are unaware of the confidence levels of these early phases as the 95% threshold used in this study was constructed according to the peak amplitude. Hence, more work is needed to confirm the presence of the early responses observed on our epileptic patients.

5.5.5 Limitations

For each epileptic patient, the reconstruction of sHRFs as well as the statistical analysis was conducted on a very conservative recording sample period in which only clear IEDs were included with a comparable frequency as in the total recording time (Table 1). By doing this, we intended to ensure the best SNR for IED response by minimizing the influence of all other confounding events. However, as the duration of the selected interval can be quite limited in contrast to the total

recording time, the relatively small sample size of IEDs may also lower the statistical significance of the reconstructed sHRFs. For example, no linear sHRF for patient 5 was seen to pass the 95% confidence level possibly due to the short sample data of around 2 minutes (Fig. 12E). Proper algorithms may need to be applied in future work to correct the effect of motion artifacts and other events in the data (Brigadoi et al., 2014).

In this work, we applied temporal filters as well as a PCA technique to recorded data for the purpose of separating NIRS signals from various sources of noise originating from tissue layers over the brain and systemic physiology. However, this pre-processing step might also cause some distortion in reconstructed estimates of the true HRF, e.g. in our simulations, the spurious early dips occurring between -10s to 0s in the sHRFs were possibly due to the high-pass filtering of the simulated signals in pre-processing as we made an attempt to remove the DC component (see Fig. 3, the sHRFs and the filtered cHRF).

Finally, with this work being one of methodology development, the experimental design in this study was not randomized, not blinded and consisted of a relatively small number of patients (five). Future work with a randomized, blinded protocol and a larger patient number may be beneficial to further test our method.

5.6 Conclusion

In this work, we highlighted the importance of modeling patient-specific HRF to IEDs in the analysis of EEG-fNIRS data. Results acquired on five epileptic patients have suggested that including patient-specific HRFs in the GLM might be able to improve activation detection by increasing statistical significance and producing larger spatial extents of activations. In addition, nonlinear sHRFs generally had a better performance than linear sHRFs in the analysis when frequent IEDs were recorded in the data. We conclude that the deconvolved sHRFs might be more adequate than a canonical HRF in some analysis of IEDs with EEG-fNIRS. Clearly more work is required before such methods can be useful to clinical practice.

5.7 Acknowledgments

This work was supported by the Canadian Institutes of Health Research (CIHR) grant MOP-133643, NSERC discovery grant RGPIN-2014-06089 and by the Imaginc group at École Polytechnique de Montréal.

5.8 Appendix

5.8.1 Specific HRF estimation

5.8.1.1 Nonlinear deconvolution model

Several nonlinear least square minimization algorithms (Madsen et al., 2004) can be applied to solve the HRF time-course h from the nonlinear model. In this study, we linearize the nonlinear model followed by the Gauss-Newton iteration method (Montgomery et al., 2006) for the sake of simplicity.

Using matrix notation, we first define:

$$\boldsymbol{\theta} = \left[h_{-K_1}\ h_{-K_1+1} \dots h_{K_2}\ \omega_0\ \omega_1\ \omega_2 \dots\ \omega_I\ \lambda\right]^T,$$

$$\boldsymbol{Y} = \left[y_{K_2+1}\ y_{K_2+2} \dots y_{N-K_1}\right]^T, \boldsymbol{u} = \left[u_{K_2+1}\ u_{K_2+2} \dots u_{N-K_1}\right]^T,$$

where N is the sample number in the recording. We can re-write equation (3) concisely as $\boldsymbol{Y} = \boldsymbol{F}(\boldsymbol{\theta}, \boldsymbol{u})$. The iteration process begins when an initial point $\boldsymbol{\theta_0}$ is given. At the point $\boldsymbol{\theta_0}$, we expand $\boldsymbol{Y}$ using Taylor series, and only keep terms with a first-order partial derivative:

$$\boldsymbol{Y} = \boldsymbol{F}(\boldsymbol{\theta_0}, \boldsymbol{u}) + \sum_{v=1}^{K_1+K_2+I+3} [J(\boldsymbol{\theta}, \boldsymbol{u})_v]_{\boldsymbol{\theta}=\boldsymbol{\theta_0}} (\theta_v - \theta_{v,0}) + \boldsymbol{\varepsilon}_T \qquad (5.4)$$

where $J(\boldsymbol{\theta}, \boldsymbol{u})_v$ denotes the v^{th} element of the Jacobian matrix: $J(\boldsymbol{\theta}, \boldsymbol{u})_v = \frac{\partial \boldsymbol{F}(\boldsymbol{\theta}, \boldsymbol{u})}{\partial \theta_v}$. $\boldsymbol{\varepsilon}_T$ is the error term of the approximation. Note the difference between $\boldsymbol{\varepsilon}_T$ in equation (A.1) and the noise term ε in equation (2). If we define $\boldsymbol{Z} = \boldsymbol{Y} - \boldsymbol{F}(\boldsymbol{\theta_0}, \boldsymbol{u})$, $\boldsymbol{\beta} = \boldsymbol{\theta} - \boldsymbol{\theta_0}$, $\boldsymbol{X} = [J(\boldsymbol{\theta}, \boldsymbol{u})]_{\boldsymbol{\theta}=\boldsymbol{\theta_0}}$, equation 5.4 takes a GLM form $\boldsymbol{Z} = \boldsymbol{X\beta} + \boldsymbol{\varepsilon}_T$, from which $\boldsymbol{\beta}$ can be solved using the ordinary least square (OLS): $\widehat{\boldsymbol{\beta}} = (\boldsymbol{X}^T\boldsymbol{X})^{-1}\boldsymbol{X}^T\boldsymbol{Z}$. A new point $\widehat{\boldsymbol{\theta}}_{\boldsymbol{1}}$ is then produced by $\widehat{\boldsymbol{\theta}}_{\boldsymbol{1}} = \widehat{\boldsymbol{\beta}} + \boldsymbol{\theta_0}$, and is used as the starting point of the next iteration.

The iteration process is terminated when at least one of the following three ending criteria is met: a) all the parameters in $\boldsymbol{\theta}$ converge, i.e. $\left|\frac{\widehat{\theta}_{i+1,l}-\widehat{\theta}_{i,l}}{\widehat{\theta}_{i,l}}\right| < \delta$, where i is the iteration index and l = 1, 2, …, K_1+K_2+ I +3, δ is a small positive number; b) a reduction in the residual sum of squares of equation (3) is not obtained with the new estimate of $\boldsymbol{\theta}$, $\widehat{\boldsymbol{\theta}}_{i+1}$, than with the starting estimate $\widehat{\boldsymbol{\theta}}_i$, i.e. $S\left(\widehat{\boldsymbol{\theta}}_{\boldsymbol{i+1}}\right) > \varphi * S\left(\widehat{\boldsymbol{\theta}}_{\boldsymbol{i}}\right)$ where $S\left(\widehat{\boldsymbol{\theta}}\right) = \left(\boldsymbol{Y} - \boldsymbol{F}\left(\widehat{\boldsymbol{\theta}}, \boldsymbol{u}\right)\right)^T \left(\boldsymbol{Y} - \boldsymbol{F}\left(\widehat{\boldsymbol{\theta}}, \boldsymbol{u}\right)\right)$, φ is a scalar around 1; c) the user-specified maximum number of iterations Q is reached. The first K_1+K_2+1 elements of the final estimate of $\boldsymbol{\theta}$, $\widehat{\boldsymbol{\theta}}_Q$, are considered as the time-course of our estimated nonlinear sHRF.

In this paper, we set δ=10^{-6}, φ=1.05, Q = 20, and the initial λ_0=-0.001. The other elements in the initial point $\boldsymbol{\theta_0}$ are specified by using the estimates from the linear version of the deconvolution model introduced in section 5.8.1.2.

5.8.1.2 Linear deconvolution model

When the nonlinear coefficient λ = 0, the model turns out to be a linear deconvolution model that is similar to the model introduced in fMRI literature (Lu et al., 2006):

$$y(t) = \int_{-\infty}^{\infty} h(\sigma)u(t-\sigma)d\sigma + \sum_{i=0}^{I} t^i\omega(i) + \varepsilon \tag{5.5}$$

The discretized form of equation (A.2) is:

$$y_t = \sum_{k=-K_1}^{K_2} u_{t-k}h_k + \sum_{i=0}^{I} t^i\omega_i + \varepsilon \tag{5.6}$$

Defining $\boldsymbol{Y}$, $\boldsymbol{u}$ as in Appendix A.1, and a new $\boldsymbol{\theta}_{ln}$ by removing the coefficient λ from $\boldsymbol{\theta}$:

$$\boldsymbol{\theta}_{ln} = \left[h_{-K_1}\ h_{-K_1+1} \ldots h_{K_2}\ \omega_0\ \omega_1\ \omega_2 \ldots\ \omega_I\right]^T,$$

we then obtain a GLM model from (5.6): $\boldsymbol{Y} = \boldsymbol{X}_{ln}\boldsymbol{\theta}_{ln} + \boldsymbol{\varepsilon}$ where $\boldsymbol{\varepsilon}$ =$\left[\varepsilon_{K_2+1}\ \varepsilon_{K_2+2} \ldots \varepsilon_{N-K_1}\right]^T$ and $\boldsymbol{X}_{ln}$ is:

$$\boldsymbol{X}_{ln} = \begin{bmatrix} u_{K_1+K_2+1} & \cdots & u_1 & 1 & K_2+1 & \cdots & (K_2+1)^I \\ u_{K_1+K_2+2} & \cdots & u_2 & 1 & K_2+2 & \cdots & (K_2+2)^I \\ \vdots & \ddots & \vdots & \vdots & \vdots & \ddots & \vdots \\ u_N & \cdots & u_{N-K_1-K_2} & 1 & N-K_1 & \cdots & (N-K_1)^I \end{bmatrix}$$

By OLS, the estimate of $\boldsymbol{\theta}_{ln}$is given by $\widehat{\boldsymbol{\theta}}_{ln} = (\boldsymbol{X}_{ln}^T\boldsymbol{X}_{ln})^{-1}\boldsymbol{X}_{ln}^T\boldsymbol{Y}$. The first K_1+K_2+1 elements of $\widehat{\boldsymbol{\theta}}_{ln}$ are the time-course of our estimated linear sHRF.

5.8.2 Supplementary patient results

5.8.2.1 Patient 1

This 14 year-old patient had drug-resistant epilepsy since age 5 years due to a subtle focal cortical dysplasia in the right inferior frontal gyrus (Figure 5.10A). By visually inspecting the EEG traces, we identified a relatively long data period of over 10 minutes that contained 164 clear right frontal IEDs (Figure 5.10B). The median interval between IEDs was near 3s and 63% of the intervals were within the range of 1s to 5s.

The time-courses of the linear and the nonlinear sHRF were reconstructed for all fNIRS channels. From interpolated hemispheric maps of both linear sHRFs (refer to the video in supplementary data) and nonlinear sHRFs, high HbO concentration increase peaking at around 10s was observed in the right frontal lobe as well as in the central regions (Figure 5.10C). Channels 11, 18 and 67 were chosen based on the selection criterion (Figure 5.10D, 5.10E). The HPAs of nonlinear sHRFs were nearly twice as high as those of linear sHRFs, suggesting a potential nonlinear intervention in the HbO channels in the frontal and the central areas.

Fig. 5.10F shows the left and the right projections of EC-corrected concentration contrasts of hemoglobin concentration changes associated with right frontal IEDs. Each row of the image was generated from a distinct GLM using respectively the SPM8 cHRF, the linear sHRFs and the nonlinear sHRFs. Compared with the conventional cHRF, the use of deconvolved sHRFs (especially the nonlinear sHRFs) clearly increased both the statistical scores and the detected extents of the activations for all chromophores. The HbO increase with peak t-value of 5.7 on nonlinear contrast maps (and also, 4.8 on linear contrast maps) in the right frontal region was the most significant, allowing a correct localization of the epileptic focus site. Results were quite similar for HbT, with the peak t-value of 4.9/4.4 (resp. on nonlinear/linear contrast maps) inside the focus circle. The use of sHRFs also improved the detection of HbR activations by presenting more negative t-scores for the responses close to the right inferior frontal gyrus (peak t-values: -5.2/-4.5 on nonlinear/linear contrast maps), as well as in the left posterior frontal areas (peak t-values: -5.1/-4.4).

5.8.2.2 Patient 3

This 27 year-old woman suffered since age 9 years from predominantly nocturnal gelastic seizures. After failing 9 antiepileptic drug trials, a comprehensive presurgical evaluation was performed which localized the focus at the junction of right orbitofrontal operculum and the anterior insula (Figure 5.11A). During the selected interval of 221s of the scan, 34 right fronto-temporal IEDs were recorded (Figure 5.11B). The IED frequency on this patient was below average of the five patients, with a median interval of 4.6s and 24% of the intervals larger than 10s.

Peak HbO concentration increase was observed at about 5s after an IED mainly from channels sampling from the right frontal lobe (Figure 5.11C), including channel 16 which obtained the largest HPA gain with the nonlinear method (Figure 5.11D, 5.11E). In addition, a large HbO increase was also noticed in right central regions and parietal lobe. However, as the peak of the increase came out at around 28s, this increase was thus not considered as a direct response to IEDs and its corresponding channels were excluded prior to the selection.

Including the sHRFs in the GLM again improved the activation detection, as seen in Figure 5.11F. For example, HbO clusters and HbT clusters on nonlinear contrast maps were located in bilateral frontal lobes with much larger extents and higher peak t-scores (5.4/5.1 for HbO/HbT), compared with those observed on maps generated with cHRF (peak t-score: 4.5 for both HbO and HbT). However, the detected HbO/HbT responses in the right frontal lobe were seen to be actually a bit too anterior to the focus. For HbR, in spite of the absence of any ipsilateral HbR response on any set of contrast maps, we located an HbR decrease (peak t-value: -3.8) in the left inferior frontal gyrus contralateral to focus area on the t-map with nonlinear sHRFs. This observation may still be informative reflecting the location of the epileptic focus.

5.8.2.3 Patient 5

This 25 year-old woman with seizures since age 13 years had an epileptic focus at the right occipito-temporal junction confirmed by multimodal evaluation (Figure 5.12A). On the EEG of the selected recording period, 31 bilateral parieto-occipito-temporal IEDs, 9 right parieto-occipito-temporal IEDs and 16 generalized spike-and-wave discharges were identified (Figure 5.12B). These events were again combined due to their spatial contiguity and bilateral symmetry.

On interpolated maps of nonlinear HbO sHRFs (Figure 5.12C), we observed a high HbO increase near the right occipito-temporal junction, surrounded by noticeable HbO decreases in adjacent areas. Different from the cHRF, the sHRFs extracted from related area were seen to have a late peak time at about 11s as well as a large FWHM of around 10s. As can be seen from Figure 5.12E, the HPAs of the linear sHRFs of the selected channels were a bit lower than the 95% thresholds. In fact, none of the 71 right side channels was able to produce a qualified linear sHRF due to the low confidence level. This might be explained by that the selected recording time period for this patient (133s) was not long enough to provide sufficient number of observation points for the deconvolution model. The sHRFs from channel 19, 14 and 10 were nevertheless chosen to construct the design matrix for the following GLM analysis thanks to their relatively higher HPAs.

On t-maps generated with the cHRF (Figure 5.12F), we were only able to locate a negative HbR concentration change in the right occipital lobe with a minimum t-value of -4.2. By contrast, the use of either the linear sHRFs or the nonlinear sHRFs greatly improved the detection and presented many activated areas for all chromophore types. The location of the most significant changes was seen to be in excellent concordance with the focus region, and thus was recognized as possible response to IEDs. Larger statistical scores were found on t-maps with nonlinear sHRFs for HbO (maximum t-values: +19.3/+17.3 with nonlinear/linear sHRFs) and HbT (+13.3/+12.6). Homologous responses in the contralateral corresponding area were also observed. These contralateral activations seemed to be more scattered with some spread to the left parietal lobe.

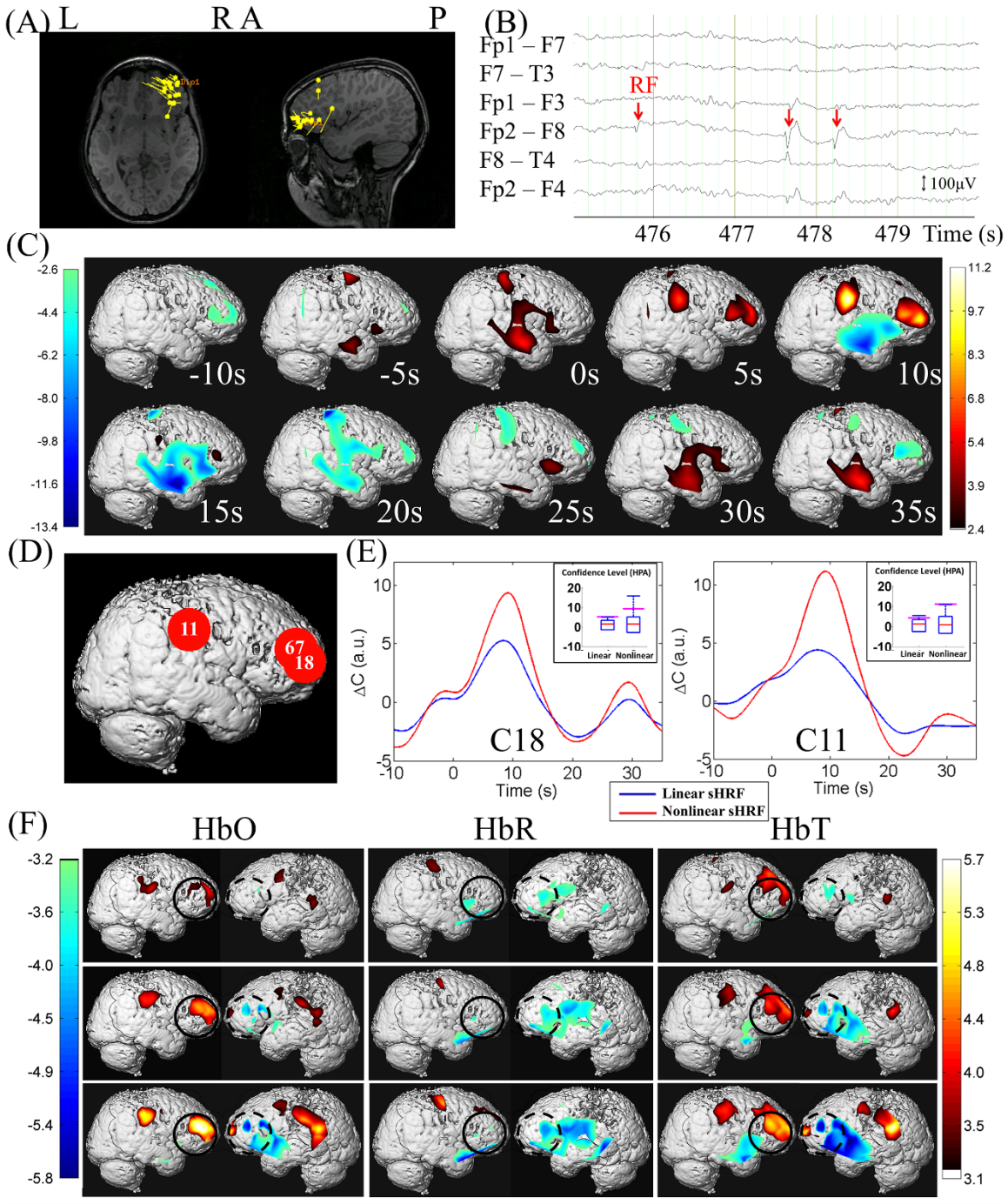

Figure 5.10 Patient 1. (A) MEG dipole localization of IEDs revealing a cluster of sources located in the right inferior frontal gyrus; (B) EEG fragment with marking for right frontal IEDs; (C) Interpolated maps of nonlinear sHRFs, from 10s before an IED to 35s after the IED (right view); (D) The covered brain areas of the three selected ipsilateral channels with highest HPAs; (E) The reconstructed linear sHRF and nonlinear sHRF of channels 18 and 11. The HPAs of nonlinear sHRFs were nearly twice as much as those of linear ones. Confidence levels of each deconvolved sHRF were presented using the surrogate series method; (F) T-statistical maps of HbO, HbR and HbT response to right frontal IEDs, generated from GLMs using respectively the SPM8 canonical HRF (first row), linear sHRFs (second row) and nonlinear sHRFs (third row). T-maps were EC-corrected, $p<0.05$. Solid black circle (30mm radius): projected most plausible focus region; dotted black circle: contralateral region to the focus.

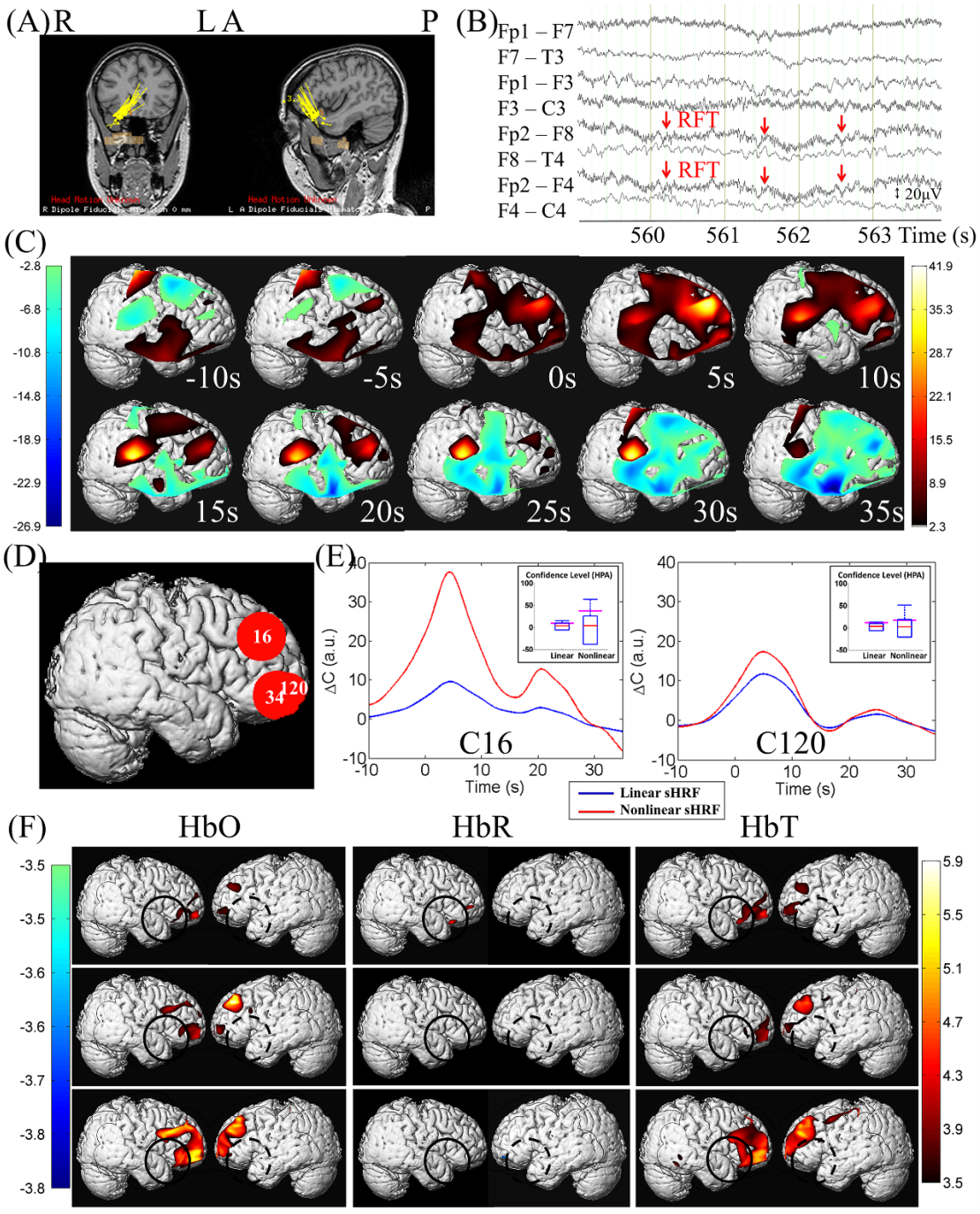

Figure 5.11 Patient 3. (A) MEG dipole localization of IEDs revealing a cluster of sources located in the junction of right orbitofrontal areas and operculum-anterior insula; (B) EEG fragment with marking for right fronto-temporal IEDs; (C) Interpolated maps of nonlinear sHRFs, from 10s before an IED to 35s after the IED (right view); (D) The covered brain areas of the three selected ipsilateral channels with highest HPAs; (E) The reconstructed linear sHRF and nonlinear sHRF of channel 16 and 120. Nonlinearity was seen to be the most significant near channel 16. Confidence levels of each deconvolved sHRF were presented using the surrogate method; (F) T-statistical maps of HbO, HbR and HbT response to right fronto-temporal IEDs, generated from GLMs using respectively the SPM8 canonical HRF (the first row), linear sHRFs (the second row) and nonlinear sHRFs (the third row). T-maps were EC-corrected, $p<0.05$. Solid black circle (30mm radius) indicates the projected most plausible focus region; dotted black circle shows the contralateral region corresponding to focus.

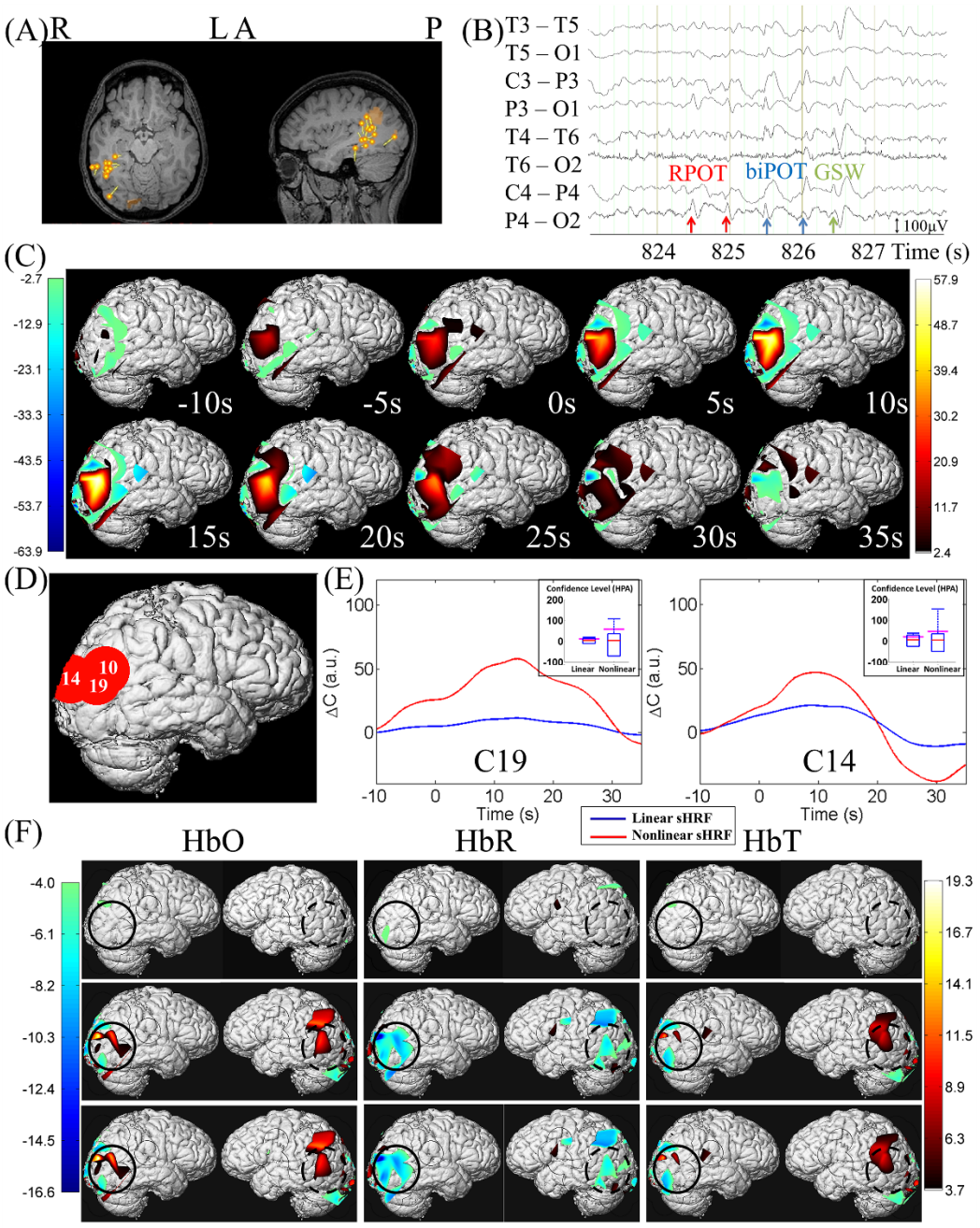

Figure 5.12 Patient 5. (A) MEG dipole localization of IEDs revealing a cluster of sources located at occipito-temporal junction; (B) EEG fragment with marking for right parieto-occipito-temporal (POT) IEDs, bilateral POT IEDs and general spike and waves; (C) Interpolated maps of nonlinear sHRFs, from 10s before an IED to 35s after the IED (right view); (D) The covered brain areas of the three selected ipsilateral channels with highest HPAs; (E) The reconstructed linear sHRF and nonlinear sHRF of channel 19 and 14. Both types of sHRFs were quite different from the cHRF in characteristics such as peaking time and full width at half maximum of the main peak; (F) T-statistical maps of HbO, HbR and HbT response to IEDs combined from right POT IEDs, bilateral POT IEDs and general spike and waves, generated from GLMs using respectively the SPM8 canonical HRF (the first row), linear sHRFs (the second row) and nonlinear sHRFs (the third row). T-maps were EC-corrected, $p<0.05$. Solid black circle (30mm radius) indicates the projected most plausible focus region; dotted black circle shows the contralateral region corresponding to focus.

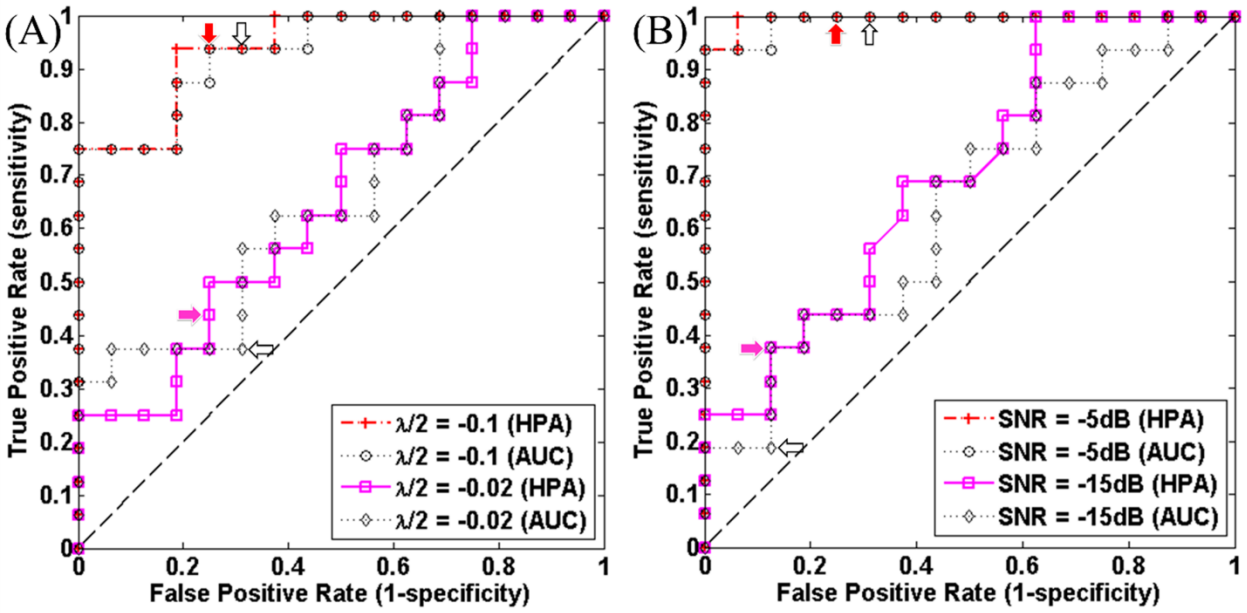

Figure 5.13 Simulation results: detectability of nonlinearity under the criteria of HPA or AUC. (A) ROC curves for HPA or AUC to detect nonlinear signals at two different nonlinear coefficients. SNR was fixed at -2dB. The arrow indicates a threshold of $p = 0.05$ on each ROC curve. (B) ROC curves for HPA or AUC at different SNRs, with $\lambda = -0.2$. HPA was a better indicator than AUC at low SNRs.

Table 5.3 Summary of focus localization results of the five patients.

#	Focus	H	Hemodynamic Response (SPM8 cHRF)	SEN/SPE (cHRF)	Hemodynamic Response (Linear sHRF)	SEN/SPE (linear)	Hemodynamic Response (Nonlinear sHRF)	SEN/SPE (nonlinear)
1	R F (IFG)	HbO	↑↑ R F (MFG): 4.0	1/1	↑↑ R F (MFG+IFG): 4.8	1/1	↑↑ R F (MFG+IFG): 5.7	1/1
		HbR	↓ R F (IFG): -4.2	1/0	↓ R F (IFG): -4.5	1/0	↓ R F (IFG): -5.2	1/0
		HbT	↑↑ R F (MFG): 4.3	1/1	↑↑ R F (MFG): 4.4	1/1	↑↑ R F (MFG): 4.9	1/1
2	L O (MOG)	HbO		0/0	↑↑ L O (MOG): +7.8	1/1	↑↑ L O (MOG): 11.6	1/1
		HbR		0/0	↓ L O (MOG): -5.2	1/0	↓ L O (MOG): -4.5	1/0
		HbT		0/0	↑↑ L O (MOG): +6.7	1/1	↑↑ L O (MOG): 11.3	1/1
3	R OrbitoF R aINS	HbO	↑ R F (IFG): 3.8	1/0	↑ R F (IFG): 3.9	1/0	↑ R F (IFG): 4.8	1/0
		HbR		0/0		0/0		0/0
		HbT	↑ R F (IFG): 4.2	1/0	↑ R F (IFG): 3.6	1/0	↑ R F (IFG): 4.6	1/0
4	R T (ITG)	HbO		0/0	↑ R posT: 4.8	1/0	↑↑ R posT: 7.9	1/1
		HbR		0/0	↓ R T (ITG): -4.6	1/0	↓↓ R T (ITG): -6.8	1/1
		HbT		0/0	↑ R posT: 4.9	1/0	↑↑ R posT: 7.9	1/1
5	R TO	HbO	↓ R O: -4.3	0/0	↑↑ R O, R posT: 17.3	1/1	↑↑ R O, R posT: 19.3	1/1
		HbR	↓ R O: -4.2	0/0	↓↓ R O, R posT: -16.6	1/1	↓↓ R O, R posT: -16.0	1/1
		HbT	↓ R O: -4.1	0/0	↑↑ R O, R posT: 12.6	1/1	↑↑ R O, R posT: 13.3	1/1
	Total (5 patients)	HbO		2/1		5/3		5/4
		HbR		1/0		4/1		4/2
		HbT		2/1		5/3		5/4

Abbreviations: L, left; R, right; F, frontal; T, temporal; P, parietal; O, occipital; IFG, inferior frontal gyrus; MFG, middle frontal gyrus; MOG, middle occipital gyrus; OrbitoF, orbitofrontal; aINS, anterior insula; ITG, inferior temporal gyrus; posT, posterior temporal lobe; SEN, localization sensitivity; SPE, localization specificity.

5.9 References

Bagshaw, A.P., Aghakhani, Y., Bénar, C.-G., Kobayashi, E., Hawco, C., Dubeau, F., Pike, G.B., Gotman, J., 2004. EEG-fMRI of focal epileptic spikes: analysis with multiple haemodynamic functions and comparison with gadolinium-enhanced MR angiograms. Hum. Brain Mapp. 22, 179–192. doi:10.1002/hbm.20024

Bénar, C.G., Gross, D.W., Wang, Y., Petre, V., Pike, B., Dubeau, F., Gotman, J., 2002. The BOLD response to interictal epileptiform discharges. NeuroImage 17, 1182–1192.

Ben Bashat, D., Artzi, M., Ben Ami, H., Aizenstein, O., Blumenthal, D.T., Bokstein, F., Corn, B.W., Ram, Z., Kanner, A.A., Lifschitz-Mercer, B., Solar, I., Kolatt, T., Palmon, M., Edrei, Y., Abramovitch, R., 2012. Hemodynamic response imaging: a potential tool for the assessment of angiogenesis in brain tumors. PloS One 7, e49416. doi:10.1371/journal.pone.0049416

Brigadoi, S., Ceccherini, L., Cutini, S., Scarpa, F., Scatturin, P., Selb, J., Gagnon, L., Boas, D.A., Cooper, R.J., 2014. Motion artifacts in functional near-infrared spectroscopy: a comparison of motion correction techniques applied to real cognitive data. NeuroImage 85 Pt 1, 181–191. doi:10.1016/j.neuroimage.2013.04.082

Cui, X., Bray, S., Bryant, D.M., Glover, G.H., Reiss, A.L., 2011. A quantitative comparison of NIRS and fMRI across multiple cognitive tasks. NeuroImage 54, 2808–2821. doi:10.1016/j.neuroimage.2010.10.069

Ding, X.P., Fu, G., Lee, K., 2014. Neural correlates of own- and other-race face recognition in children: A functional near-infrared spectroscopy study. NeuroImage, Celebrating 20 Years of Functional Near Infrared Spectroscopy (fNIRS) 85, Part 1, 335–344. doi:10.1016/j.neuroimage.2013.07.051

Friston, K.J., Ashburner, J.T., Kiebel, S.J., Nichols, T.E., Penny, W.D., 2007. Statistical Parametric Mapping: The Analysis of Functional Brain Images. Academic Press.

Friston, K.J., Fletcher, P., Josephs, O., Holmes, A., Rugg, M.D., Turner, R., 1998. Event-related fMRI: characterizing differential responses. NeuroImage 7, 30–40. doi:10.1006/nimg.1997.0306

Friston, K.J., Mechelli, A., Turner, R., Price, C.J., 2000. Nonlinear responses in fMRI: The balloon model, Volterra kernels, and other hemodynamics. NeuroImage 12, 466–477.

Gössl, C., Fahrmeir, L., Auer, D.P., 2001. Bayesian Modeling of the Hemodynamic Response Function in BOLD fMRI. NeuroImage 14, 140–148. doi:10.1006/nimg.2001.0795

Goutte, C., Nielsen, F.A., Hansen, L.K., 2000. Modeling the haemodynamic response in fMRI using smooth FIR filters. IEEE Trans. Med. Imaging 19, 1188–1201. doi:10.1109/42.897811

Handwerker, D.A., Ollinger, J.M., D'Esposito, M., 2004. Variation of BOLD hemodynamic responses across subjects and brain regions and their effects on statistical analyses. NeuroImage 21, 1639–1651. doi:10.1016/j.neuroimage.2003.11.029

Hawco, C.S., Bagshaw, A.P., Lu, Y., Dubeau, F., Gotman, J., 2007. BOLD changes occur prior to epileptic spikes seen on scalp EEG. NeuroImage 35, 1450–1458. doi:10.1016/j.neuroimage.2006.12.042

Heckman, G.M., Bouvier, S.E., Carr, V.A., Harley, E.M., Cardinal, K.S., Engel, S.A., 2007. Nonlinearities In Rapid Event-Related fMRI Explained by Stimulus Scaling. NeuroImage 34, 651–660. doi:10.1016/j.neuroimage.2006.09.038

Huppert, T.J., Diamond, S.G., Franceschini, M.A., Boas, D.A., 2009. HomER: a review of time-series analysis methods for near-infrared spectroscopy of the brain. Appl. Opt. 48, D280–298.

Jacobs, J., Hawco, C., Kobayashi, E., Boor, R., LeVan, P., Stephani, U., Siniatchkin, M., Gotman, J., 2008. Variability of the hemodynamic response as a function of age and frequency of epileptic discharge in children with epilepsy. NeuroImage 40, 601–614. doi:10.1016/j.neuroimage.2007.11.056

Jacobs, J., Kobayashi, E., Boor, R., Muhle, H., Stephan, W., Hawco, C., Dubeau, F., Jansen, O., Stephani, U., Gotman, J., Siniatchkin, M., 2007. Hemodynamic responses to interictal epileptiform discharges in children with symptomatic epilepsy. Epilepsia 48, 2068–2078. doi:10.1111/j.1528-1167.2007.01192.x

Jacobs, J., LeVan, P., Moeller, F., Boor, R., Stephani, U., Gotman, J., Siniatchkin, M., 2009. Hemodynamic changes preceding the interictal EEG spike in patients with focal epilepsy investigated using simultaneous EEG-fMRI. NeuroImage 45, 1220–1231. doi:10.1016/j.neuroimage.2009.01.014

Jang, K.E., Tak, S., Jung, J., Jang, J., Jeong, Y., Ye, J.C., 2009. Wavelet minimum description length detrending for near-infrared spectroscopy. J. Biomed. Opt. 14, 034004. doi:10.1117/1.3127204

Jöbsis, F.F., 1977. Noninvasive, infrared monitoring of cerebral and myocardial oxygen sufficiency and circulatory parameters. Science 198, 1264–1267.

Josephs, O., Turner, R., Friston, K., 1997. Event-related f MRI. Hum. Brain Mapp. 5, 243–248. doi:10.1002/(SICI)1097-0193(1997)5:4<243::AID-HBM7>3.0.CO;2-3

Lemieux, L., Laufs, H., Carmichael, D., Paul, J.S., Walker, M.C., Duncan, J.S., 2008. Noncanonical spike-related BOLD responses in focal epilepsy. Hum. Brain Mapp. 29, 329–345. doi:10.1002/hbm.20389

Li, H., Tak, S., Ye, J.C., 2012. Lipschitz-Killing curvature based expected Euler characteristics for p-value correction in fNIRS. J. Neurosci. Methods 204, 61–67. doi:10.1016/j.jneumeth.2011.10.016

Lindquist, M.A., Meng Loh, J., Atlas, L.Y., Wager, T.D., 2009. Modeling the hemodynamic response function in fMRI: efficiency, bias and mis-modeling. NeuroImage 45, S187–198. doi:10.1016/j.neuroimage.2008.10.065

Lu, Y., Bagshaw, A.P., Grova, C., Kobayashi, E., Dubeau, F., Gotman, J., 2006. Using voxel-specific hemodynamic response function in EEG-fMRI data analysis. NeuroImage 32, 238–247. doi:10.1016/j.neuroimage.2005.11.040

Machado, A., Lina, J.M., Tremblay, J., Lassonde, M., Nguyen, D.K., Lesage, F., Grova, C., 2011. Detection of hemodynamic responses to epileptic activity using simultaneous Electro-EncephaloGraphy (EEG)/Near Infra Red Spectroscopy (NIRS) acquisitions. NeuroImage 56, 114–125. doi:10.1016/j.neuroimage.2010.12.026

Madsen, K., Bruun, H., Tingleff, O., 2004. Methods for non-linear least squares problems, 2nd ed.

Maiwald, T., Mammen, E., Nandi, S., Timmer, J., 2008. Surrogate Data – A Qualitative and Quantitative Analysis, in: Mathematical Methods in Signal Processing and Digital Image Analysis. Springer Science & Business Media, pp. 41–74.

Mäkiranta, M., Ruohonen, J., Suominen, K., Niinimäki, J., Sonkajärvi, E., Kiviniemi, V., Seppänen, T., Alahuhta, S., Jäntti, V., Tervonen, O., 2005. BOLD signal increase preceeds EEG spike activity--a dynamic penicillin induced focal epilepsy in deep anesthesia. NeuroImage 27, 715–724. doi:10.1016/j.neuroimage.2005.05.025

Marrelec, G., Benali, H., Ciuciu, P., Pélégrini-Issac, M., Poline, J.-B., 2003. Robust Bayesian estimation of the hemodynamic response function in event-related BOLD fMRI using basic physiological information. Hum. Brain Mapp. 19, 1–17. doi:10.1002/hbm.10100

Masterton, R.A.J., Harvey, A.S., Archer, J.S., Lillywhite, L.M., Abbott, D.F., Scheffer, I.E., Jackson, G.D., 2010. Focal epileptiform spikes do not show a canonical BOLD response in patients with benign rolandic epilepsy (BECTS). NeuroImage 51, 252–260. doi:10.1016/j.neuroimage.2010.01.109

Minati, L., Visani, E., Dowell, N.G., Medford, N., Critchley, H.D., 2011. Variability comparison of simultaneous brain near-infrared spectroscopy (NIRS) and functional MRI (fMRI) during visual stimulation. J. Med. Eng. Technol. 35, 370–376. doi:10.3109/03091902.2011.595533

Moeller, F., Siebner, H.R., Wolff, S., Muhle, H., Boor, R., Granert, O., Jansen, O., Stephani, U., Siniatchkin, M., 2008. Changes in activity of striato-thalamo-cortical network precede generalized spike wave discharges. NeuroImage 39, 1839–1849. doi:10.1016/j.neuroimage.2007.10.058

Montgomery, D.C., Peck, E.A., Vining, G.G., 2006. Introduction to Linear Regression Analysis, Fourth. ed. John Wiley & Sons.

Nguyen, D.K., Tremblay, J., Pouliot, P., Vannasing, P., Florea, O., Carmant, L., Lepore, F., Sawan, M., Lesage, F., Lassonde, M., 2013. Noninvasive continuous functional near-infrared spectroscopy combined with electroencephalography recording of frontal lobe seizures. Epilepsia 54, 331–340. doi:10.1111/epi.12011

Nguyen, D.K., Tremblay, J., Pouliot, P., Vannasing, P., Florea, O., Carmant, L., Lepore, F., Sawan, M., Lesage, F., Lassonde, M., 2012. Non-invasive continuous EEG-fNIRS recording of temporal lobe seizures. Epilepsy Res. 99, 112–126. doi:10.1016/j.eplepsyres.2011.10.035

Obrig, H., 2014. NIRS in clinical neurology - a “promising” tool? NeuroImage 85 Pt 1, 535–546. doi:10.1016/j.neuroimage.2013.03.045

Osharina, V., Ponchel, E., Aarabi, A., Grebe, R., Wallois, F., 2010. Local haemodynamic changes preceding interictal spikes: a simultaneous electrocorticography (ECoG) and near-infrared spectroscopy (NIRS) analysis in rats. NeuroImage 50, 600–607. doi:10.1016/j.neuroimage.2010.01.009

Pedregosa, F., Eickenberg, M., Ciuciu, P., Thirion, B., Gramfort, A., 2014. Data-driven HRF estimation for encoding and decoding models. NeuroImage. doi:10.1016/j.neuroimage.2014.09.060

Peng, K., Nguyen, D.K., Tayah, T., Vannasing, P., Tremblay, J., Sawan, M., Lassonde, M., Lesage, F., Pouliot, P., 2014. fNIRS-EEG study of focal interictal epileptiform discharges. Epilepsy Res. 108, 491–505. doi:10.1016/j.eplepsyres.2013.12.011

Pittau, F., Levan, P., Moeller, F., Gholipour, T., Haegelen, C., Zelmann, R., Dubeau, F., Gotman, J., 2011. Changes preceding interictal epileptic EEG abnormalities: comparison between EEG/fMRI and intracerebral EEG. Epilepsia 52, 1120–1129. doi:10.1111/j.1528-1167.2011.03072.x

Plichta, M.M., Heinzel, S., Ehlis, A.-C., Pauli, P., Fallgatter, A.J., 2007. Model-based analysis of rapid event-related functional near-infrared spectroscopy (NIRS) data: A parametric validation study. NeuroImage 35, 625–634.

Pouliot, P., Tran, T.P.Y., Birca, V., Vannasing, P., Tremblay, J., Lassonde, M., Nguyen, D.K., 2014. Hemodynamic changes during posterior epilepsies: an EEG-fNIRS study. Epilepsy Res. 108, 883–890. doi:10.1016/j.eplepsyres.2014.03.007

Pouliot, P., Tremblay, J., Robert, M., Vannasing, P., Lepore, F., Lassonde, M., Sawan, M., Nguyen, D.K., Lesage, F., 2012. Nonlinear hemodynamic responses in human epilepsy: a multimodal analysis with fNIRS-EEG and fMRI-EEG. J. Neurosci. Methods 204, 326–340. doi:10.1016/j.jneumeth.2011.11.016

Proulx, S., Safi-Harb, M., Levan, P., An, D., Watanabe, S., Gotman, J., 2014. Increased sensitivity of fast BOLD fMRI with a subject-specific hemodynamic response function and application to epilepsy. NeuroImage 93 Pt 1, 59–73. doi:10.1016/j.neuroimage.2014.02.018

Rajapakse, J.C., Kruggel, F., Maisog, J.M., von Cramon, D.Y., 1998. Modeling hemodynamic response for analysis of functional MRI time-series. Hum. Brain Mapp. 6, 283–300.

Rathakrishnan, R., Moeller, F., Levan, P., Dubeau, F., Gotman, J., 2010. BOLD signal changes preceding negative responses in EEG-fMRI in patients with focal epilepsy. Epilepsia 51, 1837–1845. doi:10.1111/j.1528-1167.2010.02643.x

Richter, W., Richter, M., 2003. The shape of the fMRI BOLD response in children and adults changes systematically with age. NeuroImage 20, 1122–1131. doi:10.1016/S1053-8119(03)00347-1

Schaeffer, J.D., Yennu, A.S., Gandy, K.C., Tian, F., Liu, H., Park, H., 2014. An fNIRS investigation of associative recognition in the prefrontal cortex with a rapid event-related design. J. Neurosci. Methods 235, 308–315. doi:10.1016/j.jneumeth.2014.07.011

Storti, S.F., Formaggio, E., Bertoldo, A., Manganotti, P., Fiaschi, A., Toffolo, G.M., 2013. Modelling hemodynamic response function in epilepsy. Clin. Neurophysiol. 124, 2108–2118. doi:10.1016/j.clinph.2013.05.024

Strangman, G.E., Li, Z., Zhang, Q., 2013. Depth Sensitivity and Source-Detector Separations for Near Infrared Spectroscopy Based on the Colin27 Brain Template. PLoS ONE 8, e66319. doi:10.1371/journal.pone.0066319

Timmer, J., 2000. What can Be inferred from surrogate data testing? Phys. Rev. Lett. 85, 2647.

Toronov, V.Y., Zhang, X., Webb, A.G., 2007. A spatial and temporal comparison of hemodynamic signals measured using optical and functional magnetic resonance imaging during activation in the human primary visual cortex. NeuroImage 34, 1136–1148. doi:10.1016/j.neuroimage.2006.08.048

van Houdt, P.J., de Munck, J.C., Zijlmans, M., Huiskamp, G., Leijten, F.S.S., Boon, P.A.J.M., Ossenblok, P.P.W., 2010. Comparison of analytical strategies for EEG-correlated fMRI data in patients with epilepsy. Magn. Reson. Imaging, Proceedings of the International School on Magnetic Resonance and Brain Function Proceedings of the International School on Magnetic Resonance and Brain Function 28, 1078–1086. doi:10.1016/j.mri.2010.03.022

Vanzetta, I., Flynn, C., Ivanov, A.I., Bernard, C., Bénar, C.G., 2010. Investigation of linear coupling between single-event blood flow responses and interictal discharges in a model of experimental epilepsy. J. Neurophysiol. 103, 3139–3152. doi:10.1152/jn.01048.2009

Veldsman, M., Cumming, T., Brodtmann, A., 2015. Beyond BOLD: Optimizing functional imaging in stroke populations. Hum. Brain Mapp. 36, 1620–1636. doi:10.1002/hbm.22711

Ward, B.D., 2006. Deconvolution analysis of fMRI time series data.

Watanabe, E., Nagahori, Y., Mayanagi, Y., 2002. Focus diagnosis of epilepsy using near-infrared spectroscopy. Epilepsia 43, 50–55.

Watanabe, S., An, D., Safi-Harb, M., Dubeau, F., Gotman, J., 2014. Hemodynamic Response Function (HRF) in Epilepsy Patients with Hippocampal Sclerosis and Focal Cortical Dysplasia. Brain Topogr. 27, 613–619. doi:10.1007/s10548-014-0362-x

Woolrich, M.W., Jenkinson, M., Brady, J.M., Smith, S.M., 2004. Fully Bayesian spatio-temporal modeling of FMRI data. IEEE Trans. Med. Imaging 23, 213–231. doi:10.1109/TMI.2003.823065

Ye, J.C., Tak, S., Jang, K.E., Jung, J., Jang, J., 2009. NIRS-SPM: Statistical parametric mapping for near-infrared spectroscopy. NeuroImage 44, 428–447. doi:10.1016/j.neuroimage.2008.08.036

Zhang, N., Zhu, X.-H., Chen, W., 2008. Investigating the source of BOLD nonlinearity in human visual cortex in response to paired visual stimuli. NeuroImage 43, 204–212. doi:10.1016/j.neuroimage.2008.06.033

Zhang, T., Li, F., Gonzalez, M.Z., Maresh, E.L., Coan, J.A., 2014. A semi-parametric nonlinear model for event-related fMRI. NeuroImage 97, 178–187. doi:10.1016/j.neuroimage.2014.04.017

Zhao, M., Suh, M., Ma, H., Perry, C., Geneslaw, A., Schwartz, T.H., 2007. Focal increases in perfusion and decreases in hemoglobin oxygenation precede seizure onset in spontaneous human epilepsy. Epilepsia 48, 2059–2067. doi:10.1111/j.1528-1167.2007.01229.x

CHAPTER 6 GENERAL DISCUSSION

This thesis reports recent results and progresses in using a multichannel EEG-fNIRS system to study the cerebral hemodynamic response in human epilepsy. Two scientific papers are presented in chapter 4 and 5, focusing on the detection and the modeling of the hemodynamic response to IEDs. This chapter reviews the objectives that are initially proposed in chapter 1, validates the corresponding hypotheses, and discusses the limitations of current EEG-fNIRS technique in its application of epilepsy research.

6.1 Objective 1

The first objective of this thesis is to provide preliminary estimates of the sensitivity and the specificity of using EEG-fNIRS in detecting the hemoglobin concentration response to IEDs and in localizing the epileptic focus region. The article presented in chapter 4 addresses this objective, with a standard GLM-based analysis on a relatively large patient database (40 patients in total). EEG-fNIRS was sensitive in detecting the HbR/HbO/HbT response to IEDs in 62%/38%/38% of the 29 patients with neocortical epilepsies. The focus localization accuracy varied from 21% to 28% depending on the chromophore type for those 29 patients. In MTLE cases, although projections of the IEDs were detectable by scalp EEG, fNIRS generally had difficulities in detecting the associated hemodynamic changes.

Nevertheless, this study on one hand supports the idea that the hemoglobin concentration change associated with IEDs can be observed with EEG-fNIRS. With a large head coverage, we are able to locate remote cortical regions that are also activated by focal IEDs (especially the contralateral area corresponding to the epileptic focus, which is similar to the observation of seizures, e.g. by Nguyen et al. (2013, 2012)), despite no evidence on scalp EEG. This provides additional evidence to the current literature (Gotman, 2008; Holmes and Tucker, 2013; Rose et al., 2013; Stefan and Lopes da Silva, 2013) suggesting that the neurovascular response elicited by IEDs (although weaker than seizures) may also propagate through epileptic networks. More work is clearly needed to better understand the pathophysiology of such propagations.

However, the modest sensitivity and specificity reported in this study also imply that the standard GLM-based analysis assuming a SPM8 canonical HRF may not be optimal in fNIRS data processing to detect hemoglobin concentration changes with IEDs. One of the explanations is that

the shape of the hemoglobin response to IEDs is distinct from the SPM8 canonical HRF which is characterized by the BOLD response to external stimulations on healthy subjects. The response to IEDs are shown in the literature that it can vary across different patients (Jacobs et al., 2007; Lemieux et al., 2008; Pellegrino et al., 2016), precede the EEG evidence of epileptic discharge (Jacobs et al., 2009; Pittau et al., 2011; Rathakrishnan et al., 2010), contain significant nonlinear components (Pouliot et al., 2012), and sometimes even present an inversed shape (deactivation) (Gotman, 2008; Kobayashi et al., 2006b). This study again implies the normal neurovascular coupling mechanism might be altered in the generation of IEDs. Therefore, in order to achieve higher detection sensitivity and specificity for fNIRS, further methodological improvements are needed, including more realistic and more flexible modeling for the hemodynamic response to IEDs.

6.2 Objective 2

The article presented in chapter 5 made an attempt to address the model misspecification problem by proposing a simple deconvolution method that is able to model the patient-specific variations in the shape of the hemodynamic response to IEDs. For the selected five patients, their estimated specific HRFs (for HbO) were seen to have distinct shapes, in terms of different peaking time (5-15s), peak dispersion (FWHM from 8 to 20s), undershoot amplitudes, etc. Similar pattern of HbO response to IEDs was also observed in a recent fNIRS study by Pellegrino et al. (2016), where they maximized cortical sensitivity of fNIRS with a personalized optode montage. Moreover, for the first time, our study was able to quantitatively characterize the nonlinear contribution in the hemodynamic changes associated with rapidly recurrent IEDs. We confirmed that the nonlinear effect was always inhibitive to the linear component, but was of comparable order of magnitude. Modeling these patient-specific patterns of the hemodynamic response in the GLM-based analysis greatly improved the power of EEG-fNIRS in detecting brain areas activated by IEDs, and also benefited the accuracy of focus localization.

In summary, all these results suggested that the variability of hemodynamic response to IEDs across brain regions and across patients is significant. Such variability can have a crucial impact on the outcome of EEG-fNIRS in the observation of IEDs, and definitely should not be neglected.

A main weakness of this study was in its experimental design, as it involved very limited number of patients (five), and its patient selection criterion was not randomized and blinded. On top of that,

only a sample period of the EEG-fNIRS data (the "clean" period) was used for each patient. The same "clean" period was used both in the modeling process (as the "training" set) and in the GLM analysis (as the "detection" set). This is because the deconvolution method is a pure data-driven technique, and is highly sensitive to the SNR of fNIRS signals (especially the nonlinear deconvolution algorithm, see Figure 5.5). With the instrumental and analytical improvements for fNIRS artifact removal, the models proposed in this study should be further validated with a randomized, blinded protocol and a larger patient number. For example, adding a group of patients with rare IEDs as a comparison set to the current five patients with frequent IEDs may be beneficial to validate the deconvolution models on patient data with weaker nonlinear effect.

It should be noted that we reported higher sensitivity and higher overall accuracy of focus localization for HbR rather than for HbO or HbT in the first study, but better results for HbO than for HbR in this study. This can be partially because the HRF used in the first study was presumed to have the SPM8 cHRF shape which was initially modeled for the BOLD response. As BOLD signals have been shown to be more correlated with NIRS recording of HbR rather than of HbO or HbT in temporal pattern (Gagnon et al., 2012b; Huppert et al., 2006; Toronov et al., 2007), it is thus not implausible that better activation detection was obtained for HbR through the standard GLM analysis. In this work, the sHRF was reconstructed with a mostly data-driven deconvolution technique (linear or nonlinear) that required few assumptions (causality, time invariance, impulse form, perturbative) on the shape of the HRF (Lu et al., 2006). In this study, we decided to use the sHRF for HbO for the GLM analysis of all chromophores, thanks to the higher SNR in the fNIRS-measured HbO changes relative to HbR changes. Hence, unsurprisingly, the sensitivity and the specificity using HbO response was more distinctive than HbR response in this study.

Despite that the selected "clean" periods did not contain large movements, a PCA was still performed in the pre-processing of fNIRS data because we initially preferred to maintain an identical pre-processing setup to that in the first study, and therefore ensuring that the improvement seen in activation detection in this study was the result of the inclusion of specific HRFs in the GLM. In fact, through tests, we discovered that excluding the PCA from the pre-processing pipeline for the "clean" periods usually would not have a major impact, e.g. Figure 6.1 shows the t-statistical maps obtained from the fNIRS data of patient 2 and patient 4 without the application the PCA, for HbO, HbR and HbT using the same cHRF, linear sHRF and nonlinear sHRF as described in section 5.4.2. We noticed that the contrast maps for patient 2 (Figure 6.1A) stay almost

unchanged from Figure 5.7E. For patient 4, a small increase of the statistical scores for the HbT cluster contralateral to the focus site was seen (Figure 6.1B, compared with Figure 5.8E), which might lead to incorrect focus localization using HbT. However, in Figure 6.1A and 6.1B, the use of sHRFs (especially the nonlinear one) still presents higher statistical scores and larger spatial extents for the detected activations. Therefore, we are confident that including or excluding the PCA will not alter the conclusion of this study which supports the use of the sHRFs in the GLM in the analysis of IED data.

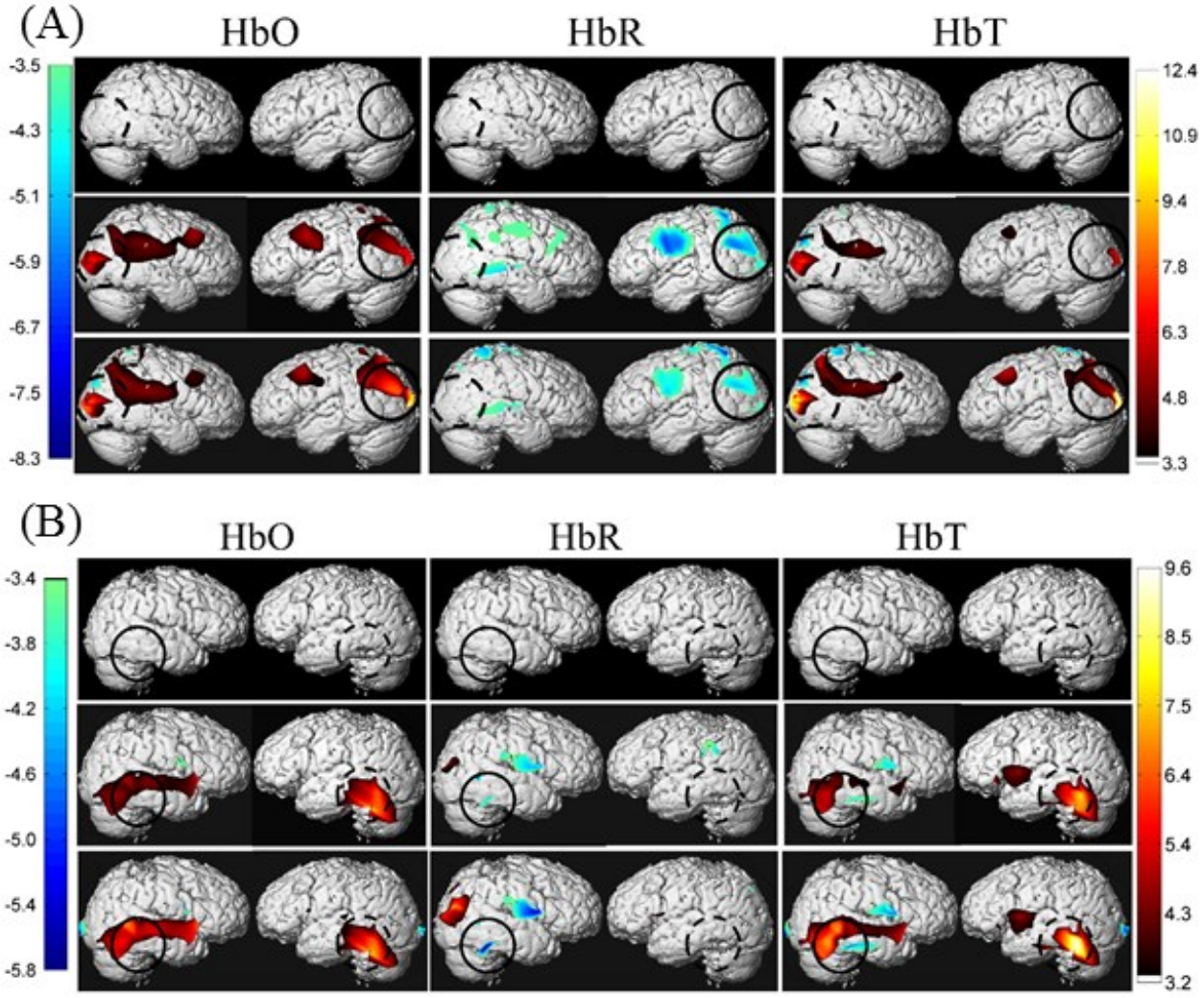

Figure 6.1 Test result without PCA for (A) Patient 2, (B) Patient 4: T-statistical maps of HbO, HbR and HbT response to IEDs, generated from GLMs using respectively the SPM8 canonical HRF (the first row), linear sHRFs (the second row) and nonlinear sHRFs (the third row). T-maps were

EC-corrected, $p<0.05$. Solid black circle (30mm radius) indicates the projected most plausible focus region; dotted black circle shows the contralateral region corresponding to focus.

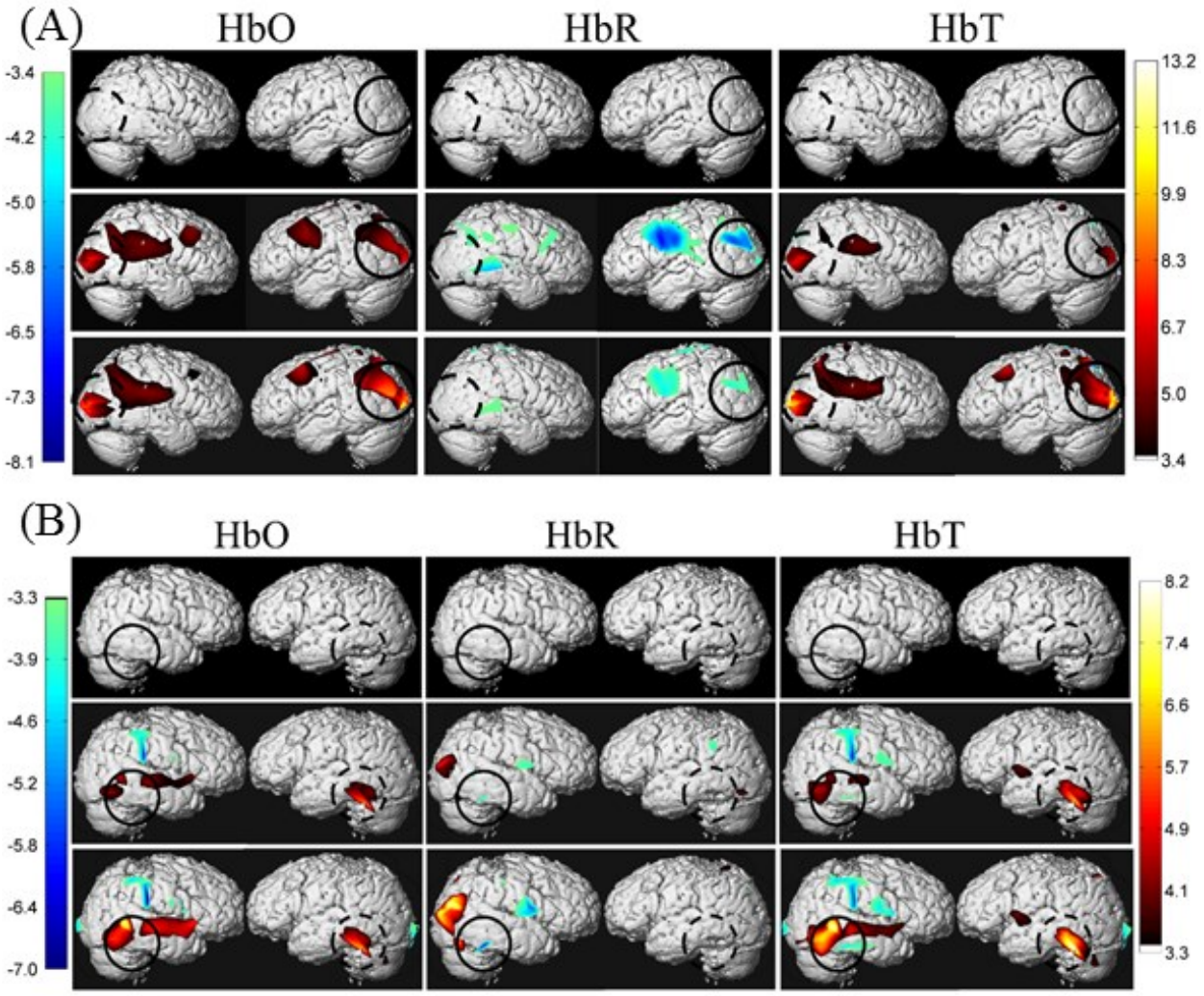

Figure 6.2 Test result, T-statistical maps. Expected hemodynamic response was derived using only one channel with the highest HPA for (A) Patient 2, (B) Patient 4.

To decide the localization accuracy of EEG-fNIRS, our approach was to compare the location of the most plausible focus region of a patient with the location of the most significant activation cluster detected by fNIRS. The most significant activation cluster was recognized by two criteria, either by looking for the cluster with the largest spatial extent, or by identifying the cluster containing the highest statistical score. Through practice, we discovered that those two criteria were able to present a same cluster in most of the cases. However, in the first study, we favored the spatial extent of a cluster over its maximum statistical score (see section 4.3.4), mostly due that

the statistical score in the first study reflected the correlation of the detected fNIRS time courses only with the expected response calculated using the canonical HRF. Therefore, by putting larger weight on the spatial extent, we intended to mitigate the effect of the difference in the assumed SPM8 canonical HRF and the real HRF to IEDs of the patient. This preference for the cluster spatial extent might result in biased overlap with the compared focus region for some patients (and therefore a small bias in the final specificity estimates), e.g. sometimes two clusters could happen to merge into one large cluster through low statistical scores. In this study however, we were able to recognize the most significant activation cluster more based on the maximum statistical value, a bit similar to a previous EEG-fMRI study by Pittau et al. (2012a). The proposed HRF models accounted for the patient-specific variations when calculating the expected hemodynamic response for the GLM. Therefore, the statistical score in this study might more correctly reflect the degree of correlation between the fNIRS time courses and the real hemodynamic response to IEDs of a particular patient.

To construct the expected hemodynamic changes to IEDs with specific HRFs, three channels which were ipsilateral to the spiking field and which generated sHRFs with the highest HPAs were selected, regardless of their locations on the hemisphere (see section 5.5.1). Due to the lack of similar studies in the literature, we did not know a priori how many channels should be used in the GLM analysis. Tests have been conducted on multiple patients with different number of channels involved (one, two and three). We did not observe much difference between the maps generated with different number of channels, in terms of the statistical scores and spatial extent of detected activations, see e.g. Figure 6.2 with Figure 5.7E, 5.8E. Hence, we decided that it would be reasonable to present the case of three channels in the manuscript. This number of channels for the analysis might help mitigate the possibility of false positive channels and thus might improve the robustness of our method. However, no extensive study of this was made, and is left for future work.

6.3 Limitations of fNIRS in current study of epilepsy

This thesis has again confirmed the potential of fNIRS, combined with scalp EEG, in the context of human epilepsy, by presenting promising results in studying the hemoglobin concentration changes associated with IEDs and in localizing the epileptic focus site with the observed

hemodynamics related to IEDs. However, much more work is necessary as fNIRS still has several limitations that prevent it from being a mature technique in clinical settings.

A first issue of fNIRS is that it only provides measures of cortical hemodynamics, and thus relies on the neurovascular coupling to infer neural activity. However, the relation between the measured hemodynamic change and the underlying neural activity in epilepsy is not fully understood, which may bring extreme confusions in the interpretation of fNIRS results. For example, what is the correct shape of the HRF to IEDs in local activated areas and in remote propagated regions? How are factors such as the type of epilepsy, the site of IEDs, the frequency of IEDs, the age of the patient or other conditions affect the shape of the HRF? The two studies included in this thesis demonstrated that the correct specification of the HRF model is essential to produce favorable results. The second study made a first attempt to account for the patient-specific variability in the HRF with a simple approach. However, these studies did not provide a standard solution.

Another disadvantage of fNIRS is its limited penetration depth, which is also shared by scalp EEG. The SD separation of 3-5cm in our work ensured sensitivity of fNIRS signals only within the top 2-3mm of the cortex (Irani et al., 2007). This might explain why our approach encountered difficulties in detecting the hemodynamic response to IEDs in MTLE cases. Furthermore, the low sensitivity of fNIRS to the brain tissue also means that the recorded data contain a large contribution from extracerebral tissue, e.g. the scalp, which may interfere with data interpretation. For a normal adult subject, Monte Carlo simulation shows that only 8% of the signal is from the brain tissue for an SD channel of 3cm (Selb et al., 2014), and even less for shorter channels (Strangman et al., 2013). To increase the penetration depth and the brain sensitivity of fNIRS, some studies pointed out that the distance of SD channels should be increased, e.g. to be longer than 5cm (Germon et al., 1999). However, increasing SD distance may not only further lower the spatial resolution of fNIRS, but also decrease the SNR if the increased channel length exceeds the limit on the separation where reliable signals can be detected. Therefore, Strangman et al. (2013) summarized that tradeoffs have to be made among brain sensitivity, SNR and spatial resolution when using current fNIRS systems. Recent studies discovered that using a very short SD separation (e.g. <1cm as suggested by Brigadoi and Cooper (2015); Goodwin et al. (2014)) along with a normal channel may help filter out some of the physiological noise arising from superficial tissues in the normal channel (Gagnon et al., 2013, 2012a, 2011; Saager et al., 2011; Zhang et al., 2009). Unfortunately, installing a short channel for each normal channel will probably lead to reduced

head coverage (considering that we usually have an instrumental limit on the total number of available channels), which is disadvantageous in epilepsy studies especially when the aim is at the localization of the focus region or the identification of epileptic networks. An interesting approach was applied in Franceschini et al. (2003) in their study of sensorimotor stimulation, where the authors used the signal timecourse from a single "inactivated" brain region far from the main recording site to correct the signals from all the other locations. However, this method needs to be further validated.

The spatial resolution of fNIRS is usually quoted to be of the order of a few centimeters (Quaresima et al., 2012), which is considered to be poor compared to its peers. e.g. fMRI (Cui et al., 2011). In our work, keeping the SD distance to be 3-5cm leads to an estimate of our spatial resolution to be 1-3cm depending on specific SD arrangement. Therefore, the activation reconstruction at most of the pixels on the 2D projection map relied completely on the inhomogeneous interpolation of the statistics from adjacent, sparsely distributed channels, and thus might not accurately reflect the strength or the extent of the activation at specific pixels. The spatial resolution of fNIRS can be greatly improved to of the order of ~5mm (Eggebrecht et al., 2012) by providing overlapping measurements of the tissue, a methodology called diffuse optical tomography (DOT) (Boas et al., 2004a, 2004b), which allows 3D image reconstruction by solving the inverse problem (and thus also help distinguish extracerebral contamination from brain signals). This approach requires a dense array of NIRS optodes as well as complex and time-consuming data analysis process, e.g. in the inversion of the sensitivity matrix. These limitations of DOT normally result in a very limited sampling coverage (Hassanpour et al., 2014; White and Culver, 2010; Zeff et al., 2007). Therefore, this technique has not yet been applied to epilepsy research.

Finally, fNIRS data acquisition can be disturbed by movement artifacts especially during the recording of seizures. Several methods have been proposed to address this problem, either with additional equipments (Virtanen et al., 2011; Yücel et al., 2014a) or with signal denoising techniques (Scholkmann et al., 2010; Vinette et al., 2015; Yücel et al., 2014b). However, there is still no standard method for the correction of motion artifacts in fNIRS signals (Brigadoi et al., 2014).

CHAPTER 7 CONCLUSION AND RECOMMANDATION

In this thesis, multichannel EEG-fNIRS was employed to study the hemodynamic response to IEDs in human epilepsy. With a standard GLM-based analysis, significant hemoglobin concentration changes could be seen near the epileptic focus region on some patients, especially on patients with neocortical epilepsies. The sufficiently large head coverage also allowed the observation of remote activations elicited by IEDs in some cases. Although the overall sensitivity in detecting activations and the accuracy in localizing the epileptic focus region were modest in the standard analysis, it was also shown that they could both be improved with careful modelling of the patient-specific variations in the shape of the HRF, based on the results obtained from five selected patients.

Compared with other functional neuroimaging techniques, fNIRS offers the potential for long-term, non-invasive monitoring and high temporal resolution hemodynamic imaging, with low cost but high safety and portability. However, most previous studies using EEG-fNIRS only focused on the observation of seizures which are known to be quite unpredictable and are difficult to be captured. Despite that no standard solution was provided, this thesis to some extent proposed an alternative option for doctors and epileptologists using EEG-fNIRS, that they might not necessarily need to wait for the occurrence of natural seizures which is a normally tedious process for both the doctors and the patients, but can instead study the hemodynamics associated with IEDs to acquire information regarding the location of the epileptic focus site, the epileptic networks, etc.

However, the results from this study also suggested that further efforts are still needed to validate the clinical utility of EEG-fNIRS in epilepsy research and treatment. The following challenges need to be addressed: a deeper understanding of hemodynamics associated with IEDs; the development of a comfortable recording system with large spatial coverage combined with long term monitoring for days or even weeks, and portable use; and the improvements of analytical methods including appropriate modelling and artifact reduction. Randomized and blinded protocols with a larger patient number are also mandatory. Should it lives up to its expectations, combined EEG-fNIRS could in time be employed routinely in the epilepsy monitoring unit as a useful tool for long-term patient monitoring and for presurgical evaluations.

BIBLIOGRAPHY

Adelson, P.D., Nemoto, E., Scheuer, M., Painter, M., Morgan, J., Yonas, H., 1999. Noninvasive Continuous Monitoring of Cerebral Oxygenation Periictally Using Near-Infrared Spectroscopy: A Preliminary Report. Epilepsia 40, 1484–1489. doi:10.1111/j.1528-1157.1999.tb02030.x

Ahammad, N., Fathima, T., Joseph, P., 2014. Detection of Epileptic Seizure Event and Onset Using EEG. BioMed Res. Int. 2014, e450573. doi:10.1155/2014/450573

Ahnlide, J.-A., Rosén, I., Lindén-Mickelsson Tech, P., Källén, K., 2007. Does SISCOM contribute to favorable seizure outcome after epilepsy surgery? Epilepsia 48, 579–588. doi:10.1111/j.1528-1167.2007.00998.x

Albert, G.W., Ibrahim, G.M., Otsubo, H., Ochi, A., Go, C.Y., Snead, O.C., Drake, J.M., Rutka, J.T., 2014. Magnetoencephalography-guided resection of epileptogenic foci in children. J. Neurosurg. Pediatr. 14, 532–537. doi:10.3171/2014.8.PEDS13640

Alomar, S., Jones, J., Maldonado, A., Gonzalez-Martinez, J., 2016. The Stereo-Electroencephalography Methodology. Neurosurg. Clin. N. Am. 27, 83–95. doi:10.1016/j.nec.2015.08.003

An, D., Dubeau, F., Gotman, J., 2015. BOLD responses related to focal spikes and widespread bilateral synchronous discharges generated in the frontal lobe. Epilepsia 56, 366–374. doi:10.1111/epi.12909

An, D., Fahoum, F., Hall, J., Olivier, A., Gotman, J., Dubeau, F., 2013. Electroencephalography/functional magnetic resonance imaging responses help predict surgical outcome in focal epilepsy. Epilepsia 54, 2184–2194. doi:10.1111/epi.12434

Arca Diaz, G., Cesaron, E., Alfonso, I., Dunoyer, C., Yaylali, I., 2006. Near infrared spectroscopy in the management of status epilepticus in a young infant. Eur. J. Paediatr. Neurol. 10, 19–21. doi:10.1016/j.ejpn.2005.11.001

Arthurs, O.J., Boniface, S., 2002. How well do we understand the neural origins of the fMRI BOLD signal? Trends Neurosci. 25, 27–31.

Aydin, Ü., Vorwerk, J., Dümpelmann, M., Küpper, P., Kugel, H., Heers, M., Wellmer, J., Kellinghaus, C., Haueisen, J., Rampp, S., Stefan, H., Wolters, C.H., 2015. Combined EEG/MEG Can Outperform Single Modality EEG or MEG Source Reconstruction in Presurgical Epilepsy Diagnosis. PLoS ONE 10. doi:10.1371/journal.pone.0118753

Aydin, Ü., Vorwerk, J., Küpper, P., Heers, M., Kugel, H., Galka, A., Hamid, L., Wellmer, J., Kellinghaus, C., Rampp, S., Wolters, C.H., 2014. Combining EEG and MEG for the Reconstruction of Epileptic Activity Using a Calibrated Realistic Volume Conductor Model. PLOS ONE 9, e93154. doi:10.1371/journal.pone.0093154

Bagshaw, A.P., Aghakhani, Y., Bénar, C.-G., Kobayashi, E., Hawco, C., Dubeau, F., Pike, G.B., Gotman, J., 2004. EEG-fMRI of focal epileptic spikes: analysis with multiple haemodynamic functions and comparison with gadolinium-enhanced MR angiograms. Hum. Brain Mapp. 22, 179–192. doi:10.1002/hbm.20024

Bailey, D.L., Townsend, D.W., Valk, P.E., Maisey, M.N. (Eds.), 2005. Positron Emission Tomography. Springer-Verlag, London.

Baumgartner, C., Pataraia, E., Lindinger, G., Deecke, L., 2000. Magnetoencephalography in focal epilepsy. Epilepsia 41 Suppl 3, S39-47.

Bechtereva, N.P., Abdullaev, Y.G., 2000. Depth electrodes in clinical neurophysiology: neuronal activity and human cognitive function. Int. J. Psychophysiol. Off. J. Int. Organ. Psychophysiol. 37, 11–29.

Ben Bashat, D., Artzi, M., Ben Ami, H., Aizenstein, O., Blumenthal, D.T., Bokstein, F., Corn, B.W., Ram, Z., Kanner, A.A., Lifschitz-Mercer, B., Solar, I., Kolatt, T., Palmon, M., Edrei, Y., Abramovitch, R., 2012. Hemodynamic response imaging: a potential tool for the assessment of angiogenesis in brain tumors. PloS One 7, e49416. doi:10.1371/journal.pone.0049416

Bénar, C.G., Gross, D.W., Wang, Y., Petre, V., Pike, B., Dubeau, F., Gotman, J., 2002. The BOLD response to interictal epileptiform discharges. NeuroImage 17, 1182–1192.

Benjamini, Y., Hochberg, Y., 1995. Controlling the false discovery rate: a practical and powerful approach to multiple testing. J. R. Stat. Soc. Ser. B Methodol. 57, 289–300.

Bergey, G.K., 2013. Neurostimulation in the treatment of epilepsy. Exp. Neurol., Special Issue: Epilepsy 244, 87–95. doi:10.1016/j.expneurol.2013.04.004

Berman, M.G., Jonides, J., Nee, D.E., 2006. Studying mind and brain with fMRI. Soc. Cogn. Affect. Neurosci. 1, 158–161. doi:10.1093/scan/nsl019

Bien CG, Szinay M, Wagner J, Clusmann H, Becker AJ, Urbach H, 2009. CHaracteristics and surgical outcomes of patients with refractory magnetic resonance imaging–negative epilepsies. Arch. Neurol. 66, 1491–1499. doi:10.1001/archneurol.2009.283

Binnie, C.D., Stefan, H., 1999. Modern electroencephalography: its role in epilepsy management. Clin. Neurophysiol. Off. J. Int. Fed. Clin. Neurophysiol. 110, 1671–1697.

Blount, J.P., Cormier, J., Kim, H., Kankirawatana, P., Riley, K.O., Knowlton, R.C., 2008. Advances in intracranial monitoring. Neurosurg. Focus 25, E18. doi:10.3171/FOC/2008/25/9/E18

Blume, W.T., Lüders, H.O., Mizrahi, E., Tassinari, C., Van Emde Boas, W., Engel, J., 2001. Glossary of Descriptive Terminology for Ictal Semiology: Report of the ILAE Task Force on Classification and Terminology. Epilepsia 42, 1212–1218. doi:10.1046/j.1528-1157.2001.22001.x

Boas, D.A., Chen, K., Grebert, D., Franceschini, M.A., 2004a. Improving the diffuse optical imaging spatial resolution of the cerebral hemodynamic response to brain activation in humans. Opt. Lett. 29, 1506. doi:10.1364/OL.29.001506

Boas, D.A., Dale, A.M., Franceschini, M.A., 2004b. Diffuse optical imaging of brain activation: approaches to optimizing image sensitivity, resolution, and accuracy. NeuroImage 23 Suppl 1, S275-288. doi:10.1016/j.neuroimage.2004.07.011

Boas, D.A., Gaudette, T., Strangman, G., Cheng, X., Marota, J.J., Mandeville, J.B., 2001. The accuracy of near infrared spectroscopy and imaging during focal changes in cerebral hemodynamics. NeuroImage 13, 76–90. doi:10.1006/nimg.2000.0674

Boas, D.A., Strangman, G., Culver, J.P., Hoge, R.D., Jasdzewski, G., Poldrack, R.A., Rosen, B.R., Mandeville, J.B., 2003. Can the cerebral metabolic rate of oxygen be estimated with near-infrared spectroscopy? Phys. Med. Biol. 48, 2405–2418.

Bonnéry, C., Leclerc, P.-O., Desjardins, M., Hoge, R., Bherer, L., Pouliot, P., Lesage, F., 2012. Changes in diffusion path length with old age in diffuse optical tomography. J. Biomed. Opt. 17, 56002. doi:10.1117/1.JBO.17.5.056002

Brigadoi, S., Ceccherini, L., Cutini, S., Scarpa, F., Scatturin, P., Selb, J., Gagnon, L., Boas, D.A., Cooper, R.J., 2014. Motion artifacts in functional near-infrared spectroscopy: a comparison of motion correction techniques applied to real cognitive data. NeuroImage 85 Pt 1, 181–191. doi:10.1016/j.neuroimage.2013.04.082

Brigadoi, S., Cooper, R.J., 2015. How short is short? Optimum source-detector distance for short-separation channels in functional near-infrared spectroscopy. Neurophotonics 2, 25005. doi:10.1117/1.NPh.2.2.025005

Brinkmann, B.H., O'Brien, T.J., Mullan, B.P., O'Connor, M.K., Robb, R.A., So, E.L., 2000. Subtraction ictal SPECT coregistered to MRI for seizure focus localization in partial epilepsy. Mayo Clin. Proc. 75, 615–624. doi:10.4065/75.6.615

Buchheim, K., Obrig, H., v. Pannwitz, W., Müller, A., Heekeren, H., Villringer, A., Meierkord, H., 2004. Decrease in haemoglobin oxygenation during absence seizures in adult humans. Neurosci. Lett. 354, 119–122. doi:10.1016/j.neulet.2003.10.001

Buckley, E., 2011. Cerebral hemodynamics in high-risk neonates probed by diffuse optical spectroscopies. Publicly Access. Penn Diss.

Buxton, R.B., 2001. The elusive initial dip. NeuroImage 13, 953–958. doi:10.1006/nimg.2001.0814

Buxton, R.B., Uludağ, K., Dubowitz, D.J., Liu, T.T., 2004. Modeling the hemodynamic response to brain activation. NeuroImage 23, Supplement 1, S220–S233. doi:10.1016/j.neuroimage.2004.07.013

Buxton, R.B., Wong, E.C., Frank, L.R., 1998. Dynamics of blood flow and oxygenation changes during brain activation: the balloon model. Magn. Reson. Med. Off. J. Soc. Magn. Reson. Med. Soc. Magn. Reson. Med. 39, 855–864.

Castro, L.H., Serpa, M.H., Valério, R.M., Jorge, C.L., Ono, C.R., Arantes, P.R., Rosemberg, S., Wen, H.T., 2008. Good surgical outcome in discordant ictal EEG-MRI unilateral mesial temporal sclerosis patients. Epilepsia 49, 1324–1332. doi:10.1111/j.1528-1167.2008.01714.x

Centeno, M., Carmichael, D.W., 2014. Network Connectivity in Epilepsy: Resting State fMRI and EEG–fMRI Contributions. Front. Neurol. 5. doi:10.3389/fneur.2014.00093

Chang, B.S., Lowenstein, D.H., 2003. Epilepsy. N. Engl. J. Med. 349, 1257–1266. doi:10.1056/NEJMra022308

Chatterjee, S., Phillips, J.P., Kyriacou, P.A., 2015. Differential pathlength factor estimation for brain-like tissue from a single-layer Monte Carlo model. Conf. Proc. Annu. Int. Conf. IEEE Eng. Med. Biol. Soc. IEEE Eng. Med. Biol. Soc. Annu. Conf. 2015, 3279–3282. doi:10.1109/EMBC.2015.7319092

Chaudhary, U.J., Duncan, J.S., Lemieux, L., 2013. Mapping hemodynamic correlates of seizures using fMRI: A review. Hum. Brain Mapp. 34, 447–466. doi:10.1002/hbm.21448

Chumbley, J., Worsley, K., Flandin, G., Friston, K., 2010. Topological FDR for neuroimaging. NeuroImage 49, 3057–3064. doi:10.1016/j.neuroimage.2009.10.090

Coan, A.C., Chaudhary, U.J., Grouiller, F., Campos, B.M., Perani, S., De Ciantis, A., Vulliemoz, S., Diehl, B., Beltramini, G.C., Carmichael, D.W., Thornton, R.C., Covolan, R.J., Cendes, F., Lemieux, L., 2015. EEG-fMRI in the presurgical evaluation of temporal lobe epilepsy. J. Neurol. Neurosurg. Psychiatry. doi:10.1136/jnnp-2015-310401

Cohen, D., 1968. Magnetoencephalography: evidence of magnetic fields produced by alpha-rhythm currents. Science 161, 784–786.

Cohen, M.S., 1997. Parametric analysis of fMRI data using linear systems methods. NeuroImage 6, 93–103. doi:10.1006/nimg.1997.0278

Cohen, M.S., Bookheimer, S.Y., 1994. Localization of brain function using magnetic resonance imaging. Trends Neurosci. 17, 268–277.

Cooper, R., Winter, A.., Crow, H.., Walter, W.G., 1965. Comparison of subcortical, cortical and scalp activity using chronically indwelling electrodes in man. Electroencephalogr. Clin. Neurophysiol. 18, 217–228. doi:10.1016/0013-4694(65)90088-X

Cooper, R.J., Hebden, J.C., O'Reilly, H., Mitra, S., Michell, A.W., Everdell, N.L., Gibson, A.P., Austin, T., 2011. Transient haemodynamic events in neurologically compromised infants: a simultaneous EEG and diffuse optical imaging study. NeuroImage 55, 1610–1616. doi:10.1016/j.neuroimage.2011.01.022

Cui, X., Bray, S., Bryant, D.M., Glover, G.H., Reiss, A.L., 2011. A quantitative comparison of NIRS and fMRI across multiple cognitive tasks. NeuroImage 54, 2808–2821. doi:10.1016/j.neuroimage.2010.10.069

Cunningham, C.J.B., Zaamout, M.E., Goodyear, B., Federico, P., 2008. Simultaneous EEG-fMRI in human epilepsy. Can. J. Neurol. Sci. J. Can. Sci. Neurol. 35, 420–435.

De Ciantis, A., Lemieux, L., 2013. Localisation of epileptic foci using novel imaging modalities. Curr. Opin. Neurol. 26, 368–373. doi:10.1097/WCO.0b013e328363372c

Delpy, D.T., Cope, M., 1997. Quantification in tissue near-infrared spectroscopy. Philos. Trans. R. Soc. B Biol. Sci. 352, 649–659. doi:10.1098/rstb.1997.0046

Delpy, D.T., Cope, M., van der Zee, P., Arridge, S., Wray, S., Wyatt, J., 1988. Estimation of optical pathlength through tissue from direct time of flight measurement. Phys. Med. Biol. 33, 1433–1442.

Desjardins, M., Gagnon, L., Gauthier, C., Hoge, R.D., Dehaes, M., Desjardins-Crépeau, L., Bherer, L., Lesage, F., 2009. Application of a multicompartment dynamical model to multimodal optical imaging for investigating individual cerebrovascular properties. pp. 717109-717109–14. doi:10.1117/12.808317

Desjardins, M., Pouliot, P., Lesage, F., 2012. Principles and Applications of Diffuse Optical Imaging for the Brain. Curr. Med. Imaging Rev. 8, 157–173. doi:10.2174/157340512803759901

Devinsky, O., Sato, S., Kufta, C.V., Ito, B., Rose, D.F., Theodore, W.H., Porter, R.J., 1989. Electroencephalographic studies of simple partial seizures with subdural electrode recordings. Neurology 39, 527–533.

Devous, M.D., Thisted, R.A., Morgan, G.F., Leroy, R.F., Rowe, C.C., 1998. SPECT brain imaging in epilepsy: a meta-analysis. J. Nucl. Med. Off. Publ. Soc. Nucl. Med. 39, 285–293.

Di Bonaventura, C., Vaudano, A.E., Carnì, M., Pantano, P., Nucciarelli, V., Garreffa, G., Maraviglia, B., Prencipe, M., Bozzao, L., Manfredi, M., Giallonardo, A.T., 2006. EEG/fMRI study of ictal and interictal epileptic activity: methodological issues and future perspectives in clinical practice. Epilepsia 47 Suppl 5, 52–58. doi:10.1111/j.1528-1167.2006.00878.x

Ding, X.P., Fu, G., Lee, K., 2014. Neural correlates of own- and other-race face recognition in children: A functional near-infrared spectroscopy study. NeuroImage 85, Part 1, 335–344. doi:10.1016/j.neuroimage.2013.07.051

Donaire, A., Falcón, C., Carreno, M., Bargallo, N., Rumià, J., Setoain, J., Maestro, I., Boget, T., Pintor, L., Agudo, R., Falip, M., Fernández, S., 2009. Sequential analysis of fMRI images: A new approach to study human epileptic networks. Epilepsia 50, 2526–2537. doi:10.1111/j.1528-1167.2009.02152.x

Doppelbauer, A., Zeitlhofer, J., Zifko, U., Baumgartner, C., Mayr, N., Deecke, L., 1993. Occurrence of epileptiform activity in the routine EEG of epileptic patients. Acta Neurol. Scand. 87, 345–352.

Drzezga, A., Arnold, S., Minoshima, S., Noachtar, S., Szecsi, J., Winkler, P., Römer, W., Tatsch, K., Weber, W., Bartenstein, P., 1999. 18F-FDG PET studies in patients with extratemporal and temporal epilepsy: evaluation of an observer-independent analysis. J. Nucl. Med. Off. Publ. Soc. Nucl. Med. 40, 737–746.

Duncan, A., Meek, J.H., Clemence, M., Elwell, C.E., Fallon, P., Tyszczuk, L., Cope, M., Delpy, D.T., 1996. Measurement of Cranial Optical Path Length as a Function of Age Using Phase Resolved Near Infrared Spectroscopy. Pediatr. Res. 39, 889–894. doi:10.1203/00006450-199605000-00025

Duncan, J.S., Winston, G.P., Koepp, M.J., Ourselin, S., 2016. Brain imaging in the assessment for epilepsy surgery. Lancet Neurol. 15, 420–433. doi:10.1016/S1474-4422(15)00383-X

Durduran, T., Choe, R., Baker, W.B., Yodh, A.G., 2010. Diffuse optics for tissue monitoring and tomography. Rep. Prog. Phys. 73, 76701. doi:10.1088/0034-4885/73/7/076701

Eadie, M.J., 2012. Shortcomings in the current treatment of epilepsy. Expert Rev. Neurother. 12, 1419–1427. doi:10.1586/ern.12.129

Eggebrecht, A.T., White, B.R., Ferradal, S.L., Chen, C., Zhan, Y., Snyder, A.Z., Dehghani, H., Culver, J.P., 2012. A quantitative spatial comparison of high-density diffuse optical tomography and fMRI cortical mapping. NeuroImage 61, 1120–1128. doi:10.1016/j.neuroimage.2012.01.124

Eliashiv, D.S., Elsas, S.M., Squires, K., Fried, I., Engel, J., 2002. Ictal magnetic source imaging as a localizing tool in partial epilepsy. Neurology 59, 1600–1610.

Engel, J., 1988. Brain Metabolism and Pathophysiology of Human Epilepsy, in: M.D, M.A.D. (Ed.), Mechanisms of Epileptogenesis. Springer US, pp. 1–15.

Engel, J., Pedley, T.A., 2008. Epilepsy: A Comprehensive Textbook, 2nd ed. Lippincott-Williams & Wilkins, Philadelphia, Pa.; London.

Englot, D.J., Nagarajan, S.S., Imber, B.S., Raygor, K.P., Honma, S.M., Mizuiri, D., Mantle, M., Knowlton, R.C., Kirsch, H.E., Chang, E.F., 2015. Epileptogenic zone localization using magnetoencephalography predicts seizure freedom in epilepsy surgery. Epilepsia 56, 949–958. doi:10.1111/epi.13002

Ernst, T., Hennig, J., 1994. Observation of a fast response in functional MR. Magn. Reson. Med. 32, 146–149.

Fahoum, F., Lopes, R., Pittau, F., Dubeau, F., Gotman, J., 2012. Widespread epileptic networks in focal epilepsies: EEG-fMRI study. Epilepsia 53, 1618–1627. doi:10.1111/j.1528-1167.2012.03533.x

Fahoum, F., Zelmann, R., Tyvaert, L., Dubeau, F., Gotman, J., 2013. Epileptic Discharges Affect the Default Mode Network – fMRI and Intracerebral EEG Evidence. PLOS ONE 8, e68038. doi:10.1371/journal.pone.0068038

Faro, S.H., Mohamed, F.B., 2006. Functional MRI: Basic Principles and Clinical Applications, 1 edition. ed. Springer New York.

Felton, E.A., Cervenka, M.C., 2015. Dietary therapy is the best option for refractory nonsurgical epilepsy. Epilepsia 56, 1325–1329. doi:10.1111/epi.13075

Fisher, R.S., Boas, W. van E., Blume, W., Elger, C., Genton, P., Lee, P., Engel, J., 2005. Epileptic Seizures and Epilepsy: Definitions Proposed by the International League Against Epilepsy (ILAE) and the International Bureau for Epilepsy (IBE). Epilepsia 46, 470–472. doi:10.1111/j.0013-9580.2005.66104.x

Fougère, C. la, Rominger, A., Förster, S., Geisler, J., Bartenstein, P., 2009. PET and SPECT in epilepsy: A critical review. Epilepsy Behav. 15, 50–55. doi:10.1016/j.yebeh.2009.02.025

Franceschini, M.A., Fantini, S., Thompson, J.H., Culver, J.P., Boas, D.A., 2003. Hemodynamic evoked response of the sensorimotor cortex measured noninvasively with near-infrared optical imaging. Psychophysiology 40, 548–560.

Friston, K.J., Ashburner, J.T., Kiebel, S.J., Nichols, T.E., Penny, W.D., 2007. Statistical Parametric Mapping: The Analysis of Functional Brain Images. Academic Press, Waltham, MA.

Friston, K.J., Fletcher, P., Josephs, O., Holmes, A., Rugg, M.D., Turner, R., 1998. Event-related fMRI: characterizing differential responses. NeuroImage 7, 30–40. doi:10.1006/nimg.1997.0306

Friston, K.J., Jezzard, P., Turner, R., 1994. Analysis of functional MRI time-series. Hum. Brain Mapp. 1, 153–171. doi:10.1002/hbm.460010207

Friston, K.J., Mechelli, A., Turner, R., Price, C.J., 2000. Nonlinear responses in fMRI: The balloon model, Volterra kernels, and other hemodynamics. NeuroImage 12, 466–477.

Fujiwara, H., Greiner, H.M., Hemasilpin, N., Lee, K.H., Holland-Bouley, K., Arthur, T., Morita, D., Jain, S.V., Mangano, F.T., Degrauw, T., Rose, D.F., 2012. Ictal MEG onset source

localization compared to intracranial EEG and outcome: improved epilepsy presurgical evaluation in pediatrics. Epilepsy Res. 99, 214–224. doi:10.1016/j.eplepsyres.2011.11.007

Gagnon, L., Cooper, R.J., Yücel, M.A., Perdue, K.L., Greve, D.N., Boas, D.A., 2012a. Short separation channel location impacts the performance of short channel regression in NIRS. NeuroImage 59, 2518–2528. doi:10.1016/j.neuroimage.2011.08.095

Gagnon, L., Perdue, K., Greve, D.N., Goldenholz, D., Kaskhedikar, G., Boas, D.A., 2011. Improved recovery of the hemodynamic response in diffuse optical imaging using short optode separations and state-space modeling. NeuroImage 56, 1362–1371. doi:10.1016/j.neuroimage.2011.03.001

Gagnon, L., Yücel, M.A., Boas, D.A., Cooper, R.J., 2013. Further improvement in reducing superficial contamination in NIRS using double short separation measurements. NeuroImage. doi:10.1016/j.neuroimage.2013.01.073

Gagnon, L., Yücel, M.A., Dehaes, M., Cooper, R.J., Perdue, K.L., Selb, J., Huppert, T.J., Hoge, R.D., Boas, D.A., 2012b. Quantification of the cortical contribution to the NIRS signal over the motor cortex using concurrent NIRS-fMRI measurements. NeuroImage 59, 3933–3940. doi:10.1016/j.neuroimage.2011.10.054

Geneslaw, A.S., Zhao, M., Ma, H., Schwartz, T.H., 2011. Tissue hypoxia correlates with intensity of interictal spikes. J. Cereb. Blood Flow Metab. 31, 1394–402. doi:http://dx.doi.org/10.1038/jcbfm.2011.16

Germon, T.J., Evans, P.D., Barnett, N.J., Wall, P., Manara, A.R., Nelson, R.J., 1999. Cerebral near infrared spectroscopy: emitter-detector separation must be increased. Br. J. Anaesth. 82, 831–837.

Ghougassian, D.F., D'Souza, W., Cook, M.J., O'Brien, T.J., 2004. Evaluating the Utility of Inpatient Video-EEG Monitoring. Epilepsia 45, 928–932. doi:10.1111/j.0013-9580.2004.51003.x

Gibson, A.P., Hebden, J.C., Arridge, S.R., 2005. Recent advances in diffuse optical imaging. Phys. Med. Biol. 50, R1-43.

Girouard, H., Iadecola, C., 2006. Neurovascular coupling in the normal brain and in hypertension, stroke, and Alzheimer disease. J. Appl. Physiol. Bethesda Md 1985 100, 328–335. doi:10.1152/japplphysiol.00966.2005

Glover, G.H., 1999. Deconvolution of impulse response in event-related BOLD fMRI. NeuroImage 9, 416–29. doi:10.1006/nimg.1998.0419

Goebel, R., 2007. Localization of Brain Activity using Functional Magnetic Resonance Imaging, in: MD, C.S. (Ed.), Clinical Functional MRI, Medical Radiology. Springer Berlin Heidelberg, pp. 9–51.

Goffin, K., Dedeurwaerdere, S., Van Laere, K., Van Paesschen, W., 2008. Neuronuclear assessment of patients with epilepsy. Semin. Nucl. Med. 38, 227–239. doi:10.1053/j.semnuclmed.2008.02.004

Gok, B., Jallo, G., Hayeri, R., Wahl, R., Aygun, N., 2013. The evaluation of FDG-PET imaging for epileptogenic focus localization in patients with MRI positive and MRI negative temporal lobe epilepsy. Neuroradiology 55, 541–550. doi:10.1007/s00234-012-1121-x

Gold, L., Lauritzen, M., 2002. Neuronal deactivation explains decreased cerebellar blood flow in response to focal cerebral ischemia or suppressed neocortical function. Proc. Natl. Acad. Sci. U. S. A. 99, 7699–7704. doi:10.1073/pnas.112012499

Gonzalez-Martinez, J., Lachhwani, D., 2014. Stereoelectroencephalography in children with cortical dysplasia: technique and results. Childs Nerv. Syst. ChNS Off. J. Int. Soc. Pediatr. Neurosurg. 30, 1853–1857. doi:10.1007/s00381-014-2499-z

Goodwin, J.R., Gaudet, C.R., Berger, A.J., 2014. Short-channel functional near-infrared spectroscopy regressions improve when source-detector separation is reduced. Neurophotonics 1. doi:10.1117/1.NPh.1.1.015002

Gössl, C., Fahrmeir, L., Auer, D.P., 2001. Bayesian Modeling of the Hemodynamic Response Function in BOLD fMRI. NeuroImage 14, 140–148. doi:10.1006/nimg.2001.0795

Gotman, J., 2011. A few thoughts on "What is a seizure?" Epilepsy Behav. 22, Supplement 1, S2–S3. doi:10.1016/j.yebeh.2011.08.025

Gotman, J., 2008. Epileptic networks studied with EEG-fMRI. Epilepsia 49 Suppl 3, 42–51. doi:10.1111/j.1528-1167.2008.01509.x

Gotman, J., 1991. Relationships between interictal spiking and seizures: human and experimental evidence. Can. J. Neurol. Sci. J. Can. Sci. Neurol. 18, 573–576.

Gotman, J., Kobayashi, E., Bagshaw, A.P., Bénar, C.-G., Dubeau, F., 2006. Combining EEG and fMRI: a multimodal tool for epilepsy research. J. Magn. Reson. Imaging JMRI 23, 906–920. doi:10.1002/jmri.20577

Goutte, C., Nielsen, F.A., Hansen, L.K., 2000. Modeling the haemodynamic response in fMRI using smooth FIR filters. IEEE Trans. Med. Imaging 19, 1188–1201. doi:10.1109/42.897811

Grigg-Damberger, M.M., Foldvary-Schaefer, N., 2012. Sleep-Related Epilepsy and Electroencephalography. Sleep Med. Clin. 7, xiii–xiv. doi:10.1016/j.jsmc.2012.02.001

Groch, M.W., Erwin, W.D., 2000. SPECT in the year 2000: basic principles. J. Nucl. Med. Technol. 28, 233–244.

Grouiller, F., Thornton, R.C., Groening, K., Spinelli, L., Duncan, J.S., Schaller, K., Siniatchkin, M., Lemieux, L., Seeck, M., Michel, C.M., Vulliemoz, S., 2011. With or without spikes: localization of focal epileptic activity by simultaneous electroencephalography and functional magnetic resonance imaging. Brain 134, 2867–2886. doi:10.1093/brain/awr156

Haeussinger, F.B., Heinzel, S., Hahn, T., Schecklmann, M., Ehlis, A.-C., Fallgatter, A.J., 2011. Simulation of Near-Infrared Light Absorption Considering Individual Head and Prefrontal Cortex Anatomy: Implications for Optical Neuroimaging. PLoS ONE 6, e26377. doi:10.1371/journal.pone.0026377

Haginoya, K., Munakata, M., Kato, R., Yokoyama, H., Ishizuka, M., Iinuma, K., 2002. Ictal cerebral haemodynamics of childhood epilepsy measured with near-infrared spectrophotometry. Brain J. Neurol. 125, 1960–1971.

Haginoya, K., Uematsu, M., Munakata, M., Kakisaka, Y., Kikuchi, A., Nakayama, T., Hino-Fukuyo, N., Tsuburaya, R., Kitamura, T., Sato-Shirai, I., Abe, Y., Matsumoto, Y., Wakusawa, K., Kobayashi, T., Ishitobi, M., Togashi, N., Iwasaki, M., Nakasato, N., Iinuma,

K., 2013. The usefulness of subtraction ictal SPECT and ictal near-infrared spectroscopic topography in patients with West syndrome. Brain Dev. 35, 887–893. doi:10.1016/j.braindev.2013.08.011

Hajnal, J.V., Myers, R., Oatridge, A., Schwieso, J.E., Young, I.R., Bydder, G.M., 1994. Artifacts due to stimulus correlated motion in functional imaging of the brain. Magn. Reson. Med. 31, 283–291.

Hämäläinen, M., Hari, R., Ilmoniemi, R.J., Knuutila, J., Lounasmaa, O.V., 1993. Magnetoencephalography\char22{}theory, instrumentation, and applications to noninvasive studies of the working human brain. Rev. Mod. Phys. 65, 413–497. doi:10.1103/RevModPhys.65.413

Handwerker, D.A., Ollinger, J.M., D'Esposito, M., 2004. Variation of BOLD hemodynamic responses across subjects and brain regions and their effects on statistical analyses. NeuroImage 21, 1639–1651. doi:10.1016/j.neuroimage.2003.11.029

Hassanpour, M.S., White, B.R., Eggebrecht, A.T., Ferradal, S.L., Snyder, A.Z., Culver, J.P., 2014. Statistical analysis of high density diffuse optical tomography. NeuroImage, Celebrating 20 Years of Functional Near Infrared Spectroscopy (fNIRS) 85, Part 1, 104–116. doi:10.1016/j.neuroimage.2013.05.105

Hawco, C.S., Bagshaw, A.P., Lu, Y., Dubeau, F., Gotman, J., 2007. BOLD changes occur prior to epileptic spikes seen on scalp EEG. NeuroImage 35, 1450–1458. doi:10.1016/j.neuroimage.2006.12.042

Heckman, G.M., Bouvier, S.E., Carr, V.A., Harley, E.M., Cardinal, K.S., Engel, S.A., 2007. Nonlinearities In Rapid Event-Related fMRI Explained by Stimulus Scaling. NeuroImage 34, 651–660. doi:10.1016/j.neuroimage.2006.09.038

Heeger, D.J., Ress, D., 2002. What does fMRI tell us about neuronal activity? Nat. Rev. Neurosci. 3, 142–151. doi:10.1038/nrn730

Hill, N.J., Gupta, D., Brunner, P., Gunduz, A., Adamo, M.A., Ritaccio, A., Schalk, G., 2012. Recording human electrocorticographic (ECoG) signals for neuroscientific research and real-time functional cortical mapping. J. Vis. Exp. JoVE. doi:10.3791/3993

Hoge, R.D., Franceschini, M.A., Covolan, R.J.M., Huppert, T., Mandeville, J.B., Boas, D.A., 2005. Simultaneous recording of task-induced changes in blood oxygenation, volume, and flow using diffuse optical imaging and arterial spin-labeling MRI. NeuroImage 25, 701–707. doi:10.1016/j.neuroimage.2004.12.032

Holmes, M.D., Tucker, D.M., 2013. Identifying the Epileptic Network. Front. Neurol. 4. doi:10.3389/fneur.2013.00084

Hu, X., Le, T.H., Uğurbil, K., 1997. Evaluation of the early response in fMRI in individual subjects using short stimulus duration. Magn. Reson. Med. 37, 877–884.

Hu, X., Yacoub, E., 2012. The story of the initial dip in fMRI. NeuroImage 62, 1103–1108. doi:10.1016/j.neuroimage.2012.03.005

Huberfeld, G., Habert, M.-O., Clemenceau, S., Maksud, P., Baulac, M., Adam, C., 2006. Ictal Brain Hyperperfusion Contralateral to Seizure Onset: The SPECT Mirror Image. Epilepsia 47, 123–133. doi:http://dx.doi.org/10.1111/j.1528-1167.2006.00378.x

Huneau, C., Benali, H., Chabriat, H., 2015. Investigating Human Neurovascular Coupling Using Functional Neuroimaging: A Critical Review of Dynamic Models. Neuroenergetics Nutr. Brain Health 467. doi:10.3389/fnins.2015.00467

Huppert, T.J., Diamond, S.G., Franceschini, M.A., Boas, D.A., 2009. HomER: a review of time-series analysis methods for near-infrared spectroscopy of the brain. Appl. Opt. 48, D280-298.

Huppert, T.J., Hoge, R.D., Diamond, S.G., Franceschini, M.A., Boas, D.A., 2006. A temporal comparison of BOLD, ASL, and NIRS hemodynamic responses to motor stimuli in adult humans. NeuroImage 29, 368–382. doi:10.1016/j.neuroimage.2005.08.065

Irani, F., Platek, S.M., Bunce, S., Ruocco, A.C., Chute, D., 2007. Functional near infrared spectroscopy (fNIRS): an emerging neuroimaging technology with important applications for the study of brain disorders. Clin. Neuropsychol. 21, 9–37. doi:10.1080/13854040600910018

Jacobs, J., Hawco, C., Kobayashi, E., Boor, R., LeVan, P., Stephani, U., Siniatchkin, M., Gotman, J., 2008. Variability of the hemodynamic response as a function of age and frequency of epileptic discharge in children with epilepsy. NeuroImage 40, 601–614. doi:10.1016/j.neuroimage.2007.11.056

Jacobs, J., Kobayashi, E., Boor, R., Muhle, H., Stephan, W., Hawco, C., Dubeau, F., Jansen, O., Stephani, U., Gotman, J., Siniatchkin, M., 2007. Hemodynamic responses to interictal epileptiform discharges in children with symptomatic epilepsy. Epilepsia 48, 2068–2078. doi:10.1111/j.1528-1167.2007.01192.x

Jacobs, J., LeVan, P., Moeller, F., Boor, R., Stephani, U., Gotman, J., Siniatchkin, M., 2009. Hemodynamic changes preceding the interictal EEG spike in patients with focal epilepsy investigated using simultaneous EEG-fMRI. NeuroImage 45, 1220–1231. doi:10.1016/j.neuroimage.2009.01.014

Jang, K.E., Tak, S., Jung, J., Jang, J., Jeong, Y., Ye, J.C., 2009. Wavelet minimum description length detrending for near-infrared spectroscopy. J. Biomed. Opt. 14, 34004. doi:10.1117/1.3127204

Jeppesen, J., Beniczky, S., Johansen, P., Sidenius, P., Fuglsang-Frederiksen, A., 2015. Exploring the capability of wireless near infrared spectroscopy as a portable seizure detection device for epilepsy patients. Seizure 26, 43–48. doi:10.1016/j.seizure.2015.01.015

Jöbsis, F.F., 1977. Noninvasive, infrared monitoring of cerebral and myocardial oxygen sufficiency and circulatory parameters. Science 198, 1264–1267.

Jobst, B.C., Cascino, G.D., 2015. Resective epilepsy surgery for drug-resistant focal epilepsy: a review. JAMA 313, 285–293. doi:10.1001/jama.2014.17426

Josephs, O., Turner, R., Friston, K., 1997. Event-related f MRI. Hum. Brain Mapp. 5, 243–248. doi:10.1002/(SICI)1097-0193(1997)5:4<243::AID-HBM7>3.0.CO;2-3

Kim, S., Mountz, J.M., Kim, S., Mountz, J.M., 2011. SPECT Imaging of Epilepsy: An Overview and Comparison with F-18 FDG PET, SPECT Imaging of Epilepsy: An Overview and Comparison with F-18 FDG PET. Int. J. Mol. Imaging Int. J. Mol. Imaging 2011, 2011, e813028. doi:10.1155/2011/813028, 10.1155/2011/813028

Knowlton, R.C., 2008. Can Magnetoencephalography Aid Epilepsy Surgery? Epilepsy Curr. 8, 1–5. doi:10.1111/j.1535-7511.2007.00215.x

Kobayashi, E., Bagshaw, A.P., Benar, C.-G., Aghakhani, Y., Andermann, F., Dubeau, F., Gotman, J., 2006a. Temporal and Extratemporal BOLD Responses to Temporal Lobe Interictal Spikes. Epilepsia 47, 343–354. doi:http://dx.doi.org/10.1111/j.1528-1167.2006.00427.x

Kobayashi, E., Bagshaw, A.P., Grova, C., Dubeau, F., Gotman, J., 2006b. Negative BOLD responses to epileptic spikes. Hum. Brain Mapp. 27, 488–497. doi:10.1002/hbm.20193

Kocsis, L., Herman, P., Eke, A., 2006. The modified Beer-Lambert law revisited. Phys. Med. Biol. 51, N91-98. doi:10.1088/0031-9155/51/5/N02

Koh, P.H., Glaser, D.E., Flandin, G., Kiebel, S., Butterworth, B., Maki, A., Delpy, D.T., Elwell, C.E., 2007. Functional optical signal analysis: a software tool for near-infrared spectroscopy data processing incorporating statistical parametric mapping. J. Biomed. Opt. 12, 64010. doi:10.1117/1.2804092

Kratimenos, G.P., Thomas, D.G., Shorvon, S.D., Fish, D.R., 1993. Stereotactic insertion of intracerebral electrodes in the investigation of epilepsy. Br. J. Neurosurg. 7, 45–52.

Krishnan, B., Vlachos, I., Wang, Z.I., Mosher, J., Najm, I., Burgess, R., Iasemidis, L., Alexopoulos, A.V., 2015. Epileptic focus localization based on resting state interictal MEG recordings is feasible irrespective of the presence or absence of spikes. Clin. Neurophysiol. Off. J. Int. Fed. Clin. Neurophysiol. 126, 667–674. doi:10.1016/j.clinph.2014.07.014

Kudr, M., Krsek, P., Marusic, P., Tomasek, M., Trnka, J., Michalova, K., Jaruskova, M., Sanda, J., Kyncl, M., Zamecnik, J., Rybar, J., Jahodova, A., Mohapl, M., Komarek, V., Tichy, M., 2013. SISCOM and FDG-PET in patients with non-lesional extratemporal epilepsy: correlation with intracranial EEG, histology, and seizure outcome. Epileptic Disord. Int. Epilepsy J. Videotape 15, 3–13. doi:10.1684/epd.2013.0560

Kuruvilla, A., Flink, R., 2003. Intraoperative electrocorticography in epilepsy surgery: useful or not? Seizure - Eur. J. Epilepsy 12, 577–584. doi:10.1016/S1059-1311(03)00095-5

Kwon, C.-S., Neal, J., Telléz-Zenteno, J., Metcalfe, A., Fitzgerald, K., Hernandez-Ronquillo, L., Hader, W., Wiebe, S., Jetté, N., CASES Investigators, 2016. Resective focal epilepsy surgery - Has selection of candidates changed? A systematic review. Epilepsy Res. 122, 37–43. doi:10.1016/j.eplepsyres.2016.02.007

Lachaux, J.P., Rudrauf, D., Kahane, P., 2003. Intracranial EEG and human brain mapping. J. Physiol. Paris 97, 613–628. doi:10.1016/j.jphysparis.2004.01.018

Lareau, E., Lesage, F., Pouliot, P., Nguyen, D., Le Lan, J., Sawan, M., 2011. Multichannel wearable system dedicated for simultaneous electroencephalography/near-infrared spectroscopy real-time data acquisitions. J. Biomed. Opt. 16, 096014–096014. doi:10.1117/1.3625575

Lascano, A.M., Perneger, T., Vulliemoz, S., Spinelli, L., Garibotto, V., Korff, C.M., Vargas, M.I., Michel, C.M., Seeck, M., 2016. Yield of MRI, high-density electric source imaging (HD-ESI), SPECT and PET in epilepsy surgery candidates. Clin. Neurophysiol. 127, 150–155. doi:10.1016/j.clinph.2015.03.025

Lau, M., Yam, D., Burneo, J.G., 2008. A systematic review on MEG and its use in the presurgical evaluation of localization-related epilepsy. Epilepsy Res. 79, 97–104. doi:10.1016/j.eplepsyres.2008.01.004

Lee, D.S., Lee, S.K., Lee, M.C., 2001. Functional neuroimaging in epilepsy: FDG PET and ictal SPECT. J. Korean Med. Sci. 16, 689–696.

Lee, J.Y., Joo, E.Y., Park, H.S., Song, P., Young Byun, S., Seo, D.W., Hong, S.B., 2011. Repeated ictal SPECT in partial epilepsy patients: SISCOM analysis. Epilepsia 52, 2249–2256. doi:10.1111/j.1528-1167.2011.03257.x

Lee, S.K., Lee, S.H., Kim, S.K., Lee, D.S., Kim, H., 2000. The clinical usefulness of ictal SPECT in temporal lobe epilepsy: the lateralization of seizure focus and correlation with EEG. Epilepsia 41, 955–962.

Leite, M., Leal, A., Figueiredo, P., 2013. Transfer Function between EEG and BOLD Signals of Epileptic Activity. Front. Neurol. 4. doi:10.3389/fneur.2013.00001

Lemieux, L., Laufs, H., Carmichael, D., Paul, J.S., Walker, M.C., Duncan, J.S., 2008. Noncanonical spike-related BOLD responses in focal epilepsy. Hum. Brain Mapp. 29, 329–345. doi:10.1002/hbm.20389

Lemieux, L., Salek-Haddadi, A., Josephs, O., Allen, P., Toms, N., Scott, C., Krakow, K., Turner, R., Fish, D.R., 2001. Event-related fMRI with simultaneous and continuous EEG: description of the method and initial case report. NeuroImage 14, 780–787. doi:10.1006/nimg.2001.0853

LeVan, P., Tyvaert, L., Moeller, F., Gotman, J., 2010. Independent component analysis reveals dynamic ictal BOLD responses in EEG-fMRI data from focal epilepsy patients. NeuroImage 49, 366–378. doi:10.1016/j.neuroimage.2009.07.064

Li, H., Tak, S., Ye, J.C., 2012. Lipschitz-Killing curvature based expected Euler characteristics for p-value correction in fNIRS. J. Neurosci. Methods 204, 61–67. doi:10.1016/j.jneumeth.2011.10.016

Liao, L.-D., Tsytsarev, V., Delgado-Martínez, I., Li, M.-L., Erzurumlu, R., Vipin, A., Orellana, J., Lin, Y.-R., Lai, H.-Y., Chen, Y.-Y., Thakor, N.V., 2013. Neurovascular coupling: in vivo optical techniques for functional brain imaging. Biomed. Eng. Online 12, 38. doi:10.1186/1475-925X-12-38

Lieb, J.P., Walsh, G.O., Babb, T.L., Walter, R.D., Crandall, P.H., 1976. A comparison of EEG seizure patterns recorded with surface and depth electrodes in patients with temporal lobe epilepsy. Epilepsia 17, 137–160.

Lindauer, U., Royl, G., Leithner, C., Kühl, M., Gold, L., Gethmann, J., Kohl-Bareis, M., Villringer, A., Dirnagl, U., 2001. No evidence for early decrease in blood oxygenation in rat whisker cortex in response to functional activation. NeuroImage 13, 988–1001. doi:10.1006/nimg.2000.0709

Lindquist, M.A., Meng Loh, J., Atlas, L.Y., Wager, T.D., 2009. Modeling the hemodynamic response function in fMRI: efficiency, bias and mis-modeling. NeuroImage 45, S187-198. doi:10.1016/j.neuroimage.2008.10.065

Liporace, J., Tatum, W., Morris, G.L., French, J., 1998. Clinical utility of sleep-deprived versus computer-assisted ambulatory 16-channel EEG in epilepsy patients: a multi-center study. Epilepsy Res. 32, 357–362.

Livieratos, L., 2012. Basic Principles of SPECT and PET Imaging, in: Fogelman, I., Gnanasegaran, G., Wall, H. van der (Eds.), Radionuclide and Hybrid Bone Imaging. Springer Berlin Heidelberg, pp. 345–359.

Lloyd-Fox, S., Blasi, A., Elwell, C.E., 2010. Illuminating the developing brain: The past, present and future of functional near infrared spectroscopy. Neurosci. Biobehav. Rev. 34, 269–284. doi:10.1016/j.neubiorev.2009.07.008

Lu, Y., Bagshaw, A.P., Grova, C., Kobayashi, E., Dubeau, F., Gotman, J., 2006. Using voxel-specific hemodynamic response function in EEG-fMRI data analysis. NeuroImage 32, 238–247. doi:10.1016/j.neuroimage.2005.11.040

Lüders, H.O., Najm, I., Nair, D., Widdess-Walsh, P., Bingman, W., 2006. The epileptogenic zone: general principles. Epileptic Disord. Int. Epilepsy J. Videotape 8 Suppl 2, S1-9.

Luo, C., An, D., Yao, D., Gotman, J., 2014. Patient-specific connectivity pattern of epileptic network in frontal lobe epilepsy. NeuroImage Clin. 4, 668–675. doi:10.1016/j.nicl.2014.04.006

Machado, A., Lina, J.M., Tremblay, J., Lassonde, M., Nguyen, D.K., Lesage, F., Grova, C., 2011. Detection of hemodynamic responses to epileptic activity using simultaneous Electro-EncephaloGraphy (EEG)/Near Infra Red Spectroscopy (NIRS) acquisitions. NeuroImage 56, 114–125. doi:10.1016/j.neuroimage.2010.12.026

Machado, A., Marcotte, O., Lina, J.M., Kobayashi, E., Grova, C., 2014. Optimal optode montage on electroencephalography/functional near-infrared spectroscopy caps dedicated to study epileptic discharges. J. Biomed. Opt. 19, 26010. doi:10.1117/1.JBO.19.2.026010

Madsen, K., Bruun, H., Tingleff, O., 2004. Methods for non-linear least squares problems, 2nd ed.

Maiwald, T., Mammen, E., Nandi, S., Timmer, J., 2008. Surrogate Data – A Qualitative and Quantitative Analysis, in: Mathematical Methods in Signal Processing and Digital Image Analysis. Springer Science & Business Media, pp. 41–74.

Mäkiranta, M., Ruohonen, J., Suominen, K., Niinimäki, J., Sonkajärvi, E., Kiviniemi, V., Seppänen, T., Alahuhta, S., Jäntti, V., Tervonen, O., 2005. BOLD signal increase preceeds EEG spike activity--a dynamic penicillin induced focal epilepsy in deep anesthesia. NeuroImage 27, 715–724. doi:10.1016/j.neuroimage.2005.05.025

Malonek, D., Grinvald, A., 1996. Interactions between electrical activity and cortical microcirculation revealed by imaging spectroscopy: implications for functional brain mapping. Science 272, 551–554.

Marrelec, G., Benali, H., Ciuciu, P., Pélégrini-Issac, M., Poline, J.-B., 2003. Robust Bayesian estimation of the hemodynamic response function in event-related BOLD fMRI using basic physiological information. Hum. Brain Mapp. 19, 1–17. doi:10.1002/hbm.10100

Masterton, R.A.J., Harvey, A.S., Archer, J.S., Lillywhite, L.M., Abbott, D.F., Scheffer, I.E., Jackson, G.D., 2010. Focal epileptiform spikes do not show a canonical BOLD response in

patients with benign rolandic epilepsy (BECTS). NeuroImage 51, 252–260. doi:10.1016/j.neuroimage.2010.01.109

Megiddo, I., Colson, A., Chisholm, D., Dua, T., Nandi, A., Laxminarayan, R., 2016. Health and economic benefits of public financing of epilepsy treatment in India: An agent-based simulation model. Epilepsia. doi:10.1111/epi.13294

Menon, R.S., Ogawa, S., Hu, X., Strupp, J.P., Anderson, P., Uğurbil, K., 1995. BOLD based functional MRI at 4 Tesla includes a capillary bed contribution: echo-planar imaging correlates with previous optical imaging using intrinsic signals. Magn. Reson. Med. 33, 453–459.

Michel, C.M., Lantz, G., Spinelli, L., De Peralta, R.G., Landis, T., Seeck, M., 2004. 128-channel EEG source imaging in epilepsy: clinical yield and localization precision. J. Clin. Neurophysiol. Off. Publ. Am. Electroencephalogr. Soc. 21, 71–83.

Miller, K.J., denNijs, M., Shenoy, P., Miller, J.W., Rao, R.P.N., Ojemann, J.G., 2007. Real-time functional brain mapping using electrocorticography. NeuroImage 37, 504–507. doi:10.1016/j.neuroimage.2007.05.029

Minasyan, G.R., Chatten, J.B., Chatten, M.J., Harner, R.N., 2010. Patient-Specific Early Seizure Detection from Scalp EEG. J. Clin. Neurophysiol. Off. Publ. Am. Electroencephalogr. Soc. 27, 163–178. doi:10.1097/WNP.0b013e3181e0a9b6

Minati, L., Visani, E., Dowell, N.G., Medford, N., Critchley, H.D., 2011. Variability comparison of simultaneous brain near-infrared spectroscopy (NIRS) and functional MRI (fMRI) during visual stimulation. J. Med. Eng. Technol. 35, 370–376. doi:10.3109/03091902.2011.595533

Moeller, F., LeVan, P., Muhle, H., Stephani, U., Dubeau, F., Siniatchkin, M., Gotman, J., 2010. Absence seizures: individual patterns revealed by EEG-fMRI. Epilepsia 51, 2000–2010. doi:10.1111/j.1528-1167.2010.02698.x

Moeller, F., Siebner, H.R., Wolff, S., Muhle, H., Boor, R., Granert, O., Jansen, O., Stephani, U., Siniatchkin, M., 2008. Changes in activity of striato-thalamo-cortical network precede generalized spike wave discharges. NeuroImage 39, 1839–1849. doi:10.1016/j.neuroimage.2007.10.058

Moeller, F., Stephani, U., Siniatchkin, M., 2013. Simultaneous EEG and fMRI recordings (EEG-fMRI) in children with epilepsy. Epilepsia 54, 971–982. doi:10.1111/epi.12197

Moeller, F., Tyvaert, L., Nguyen, D.K., LeVan, P., Bouthillier, A., Kobayashi, E., Tampieri, D., Dubeau, F., Gotman, J., 2009. EEG-fMRI: adding to standard evaluations of patients with nonlesional frontal lobe epilepsy. Neurology 73, 2023–2030. doi:10.1212/WNL.0b013e3181c55d17

Montgomery, D.C., Peck, E.A., Vining, G.G., 2006. Introduction to Linear Regression Analysis, Fourth. ed. John Wiley & Sons.

Monti, M.M., 2011. Statistical Analysis of fMRI Time-Series: A Critical Review of the GLM Approach. Front. Hum. Neurosci. 5. doi:10.3389/fnhum.2011.00028

Mporas, I., Tsirka, V., Zacharaki, E.I., Koutroumanidis, M., Richardson, M., Megalooikonomou, V., 2015. Seizure detection using EEG and ECG signals for computer-based monitoring,

analysis and management of epileptic patients. Expert Syst. Appl. 42, 3227–3233. doi:10.1016/j.eswa.2014.12.009

Munakata, M., Haginoya, K., Ishitobi, M., Sakamoto, O., Sato, I., Kitamura, T., Hirose, M., Yokoyama, H., Iinuma, K., 2004. Dynamic cortical activity during spasms in three patients with West syndrome: a multichannel near-infrared spectroscopic topography study. Epilepsia 45, 1248–1257. doi:10.1111/j.0013-9580.2004.t01-1-04004.x

Nadler, J.V., Spencer, D.D., 2014. What is a seizure focus? Adv. Exp. Med. Biol. 813, 55–62. doi:10.1007/978-94-017-8914-1_4

Newey, C.R., Wong, C., Wang, Z.I., Chen, X., Wu, G., Alexopoulos, A.V., 2013. Optimizing SPECT SISCOM analysis to localize seizure-onset zone by using varying z scores. Epilepsia 54, 793–800. doi:10.1111/epi.12139

Newton, M.R., Berkovic, S.F., Austin, M.C., Rowe, C.C., McKay, W.J., Bladin, P.F., 1995. SPECT in the localisation of extratemporal and temporal seizure foci. J. Neurol. Neurosurg. Psychiatry 59, 26–30.

Nguyen, D.K., Tremblay, J., Pouliot, P., Vannasing, P., Florea, O., Carmant, L., Lepore, F., Sawan, M., Lesage, F., Lassonde, M., 2013. Noninvasive continuous functional near-infrared spectroscopy combined with electroencephalography recording of frontal lobe seizures. Epilepsia 54, 331–340. doi:10.1111/epi.12011

Nguyen, D.K., Tremblay, J., Pouliot, P., Vannasing, P., Florea, O., Carmant, L., Lepore, F., Sawan, M., Lesage, F., Lassonde, M., 2012. Non-invasive continuous EEG-fNIRS recording of temporal lobe seizures. Epilepsy Res. 99, 112–126. doi:10.1016/j.eplepsyres.2011.10.035

Nguyen, J., 2010. Diffuse Optical Spectroscopic Imaging (DOSI) [WWW Document]. Opt. Diagn. Melanoma. URL http://bme240.eng.uci.edu/students/10s/nguyenjq/index_files/DOSI.htm

O'Brien, T.J., So, E.L., Cascino, G.D., Hauser, M.F., Marsh, W.R., Meyer, F.B., Sharbrough, F.W., Mullan, B.P., 2004. Subtraction SPECT coregistered to MRI in focal malformations of cortical development: localization of the epileptogenic zone in epilepsy surgery candidates. Epilepsia 45, 367–376. doi:10.1111/j.0013-9580.2004.54703.x

O'Brien, T.J., So, E.L., Mullan, B.P., Hauser, M.F., Brinkmann, B.H., Bohnen, N.I., Hanson, D., Cascino, G.D., Jack, C.R., Sharbrough, F.W., 1998. Subtraction ictal SPECT co-registered to MRI improves clinical usefulness of SPECT in localizing the surgical seizure focus. Neurology 50, 445–454.

Obrig, H., 2014. NIRS in clinical neurology - a "promising" tool? NeuroImage 85 Pt 1, 535–546. doi:10.1016/j.neuroimage.2013.03.045

Oertzen, J. von, Urbach, H., Jungbluth, S., Kurthen, M., Reuber, M., Fernández, G., Elger, C.E., 2002. Standard magnetic resonance imaging is inadequate for patients with refractory focal epilepsy. J. Neurol. Neurosurg. Psychiatry 73, 643–647. doi:10.1136/jnnp.73.6.643

Okada, E., Firbank, M., Schweiger, M., Arridge, S.R., Cope, M., Delpy, D.T., 1997. Theoretical and experimental investigation of near-infrared light propagation in a model of the adult head. Appl. Opt. 36, 21–31.

Osharina, V., Ponchel, E., Aarabi, A., Grebe, R., Wallois, F., 2010. Local haemodynamic changes preceding interictal spikes: a simultaneous electrocorticography (ECoG) and near-infrared

spectroscopy (NIRS) analysis in rats. NeuroImage 50, 600–607. doi:10.1016/j.neuroimage.2010.01.009

Paesschen, W.V., Dupont, P., Driel, G.V., Billoen, H.V., Maes, A., 2003. SPECT perfusion changes during complex partial seizures in patients with hippocampal sclerosis. Brain 126, 1103–1111. doi:10.1093/brain/awg108

Palmini, A., 2006. The concept of the epileptogenic zone: a modern look at Penfield and Jasper's views on the role of interictal spikes. Epileptic. Disord. 8, 10–15.

Panayiotopoulos, C.P., 2005. Symptomatic and Probably Symptomatic Focal Epilepsies.

Panzica, F., Varotto, G., Rotondi, F., Spreafico, R., Franceschetti, S., 2013. Identification of the epileptogenic zone from stereo-EEG signals: a connectivity-graph theory approach. Epilepsy 4, 175. doi:10.3389/fneur.2013.00175

Papanicolaou, A.C., Pataraia, E., Billingsley-Marshall, R., Castillo, E.M., Wheless, J.W., Swank, P., Breier, J.I., Sarkari, S., Simos, P.G., 2005. Toward the substitution of invasive electroencephalography in epilepsy surgery. J. Clin. Neurophysiol. Off. Publ. Am. Electroencephalogr. Soc. 22, 231–237.

Paulson, O.B., Hasselbalch, S.G., Rostrup, E., Knudsen, G.M., Pelligrino, D., 2010. Cerebral blood flow response to functional activation. J. Cereb. Blood Flow Metab. Off. J. Int. Soc. Cereb. Blood Flow Metab. 30, 2–14. doi:10.1038/jcbfm.2009.188

Pedregosa, F., Eickenberg, M., Ciuciu, P., Thirion, B., Gramfort, A., 2014. Data-driven HRF estimation for encoding and decoding models. NeuroImage. doi:10.1016/j.neuroimage.2014.09.060

Pellegrino, G., Machado, A., von Ellenrieder, N., Watanabe, S., Hall, J.A., Lina, J.-M., Kobayashi, E., Grova, C., 2016. Hemodynamic Response to Interictal Epileptiform Discharges Addressed by Personalized EEG-fNIRS Recordings. Front. Neurosci. 10, 102. doi:10.3389/fnins.2016.00102

Penfield, W., Jasper, H., 1954. Epileptic Mechanisms (cortical circulation), in: Epilepsy and the Functional Anatomy of the Human Brain. Little, Brown and Company Ed., Boston, pp. 246–264.

Peng, K., Nguyen, D.K., Tayah, T., Vannasing, P., Tremblay, J., Sawan, M., Lassonde, M., Lesage, F., Pouliot, P., 2014. fNIRS-EEG study of focal interictal epileptiform discharges. Epilepsy Res. 108, 491–505. doi:10.1016/j.eplepsyres.2013.12.011

Pittau, F., Dubeau, F., Gotman, J., 2012a. Contribution of EEG/fMRI to the definition of the epileptic focus. Neurology 78, 1479–1487. doi:10.1212/WNL.0b013e3182553bf7

Pittau, F., Grova, C., Moeller, F., Dubeau, F., Gotman, J., 2012b. Patterns of altered functional connectivity in mesial temporal lobe epilepsy. Epilepsia 53, 1013–1023. doi:10.1111/j.1528-1167.2012.03464.x

Pittau, F., Levan, P., Moeller, F., Gholipour, T., Haegelen, C., Zelmann, R., Dubeau, F., Gotman, J., 2011. Changes preceding interictal epileptic EEG abnormalities: comparison between EEG/fMRI and intracerebral EEG. Epilepsia 52, 1120–1129. doi:10.1111/j.1528-1167.2011.03072.x

Plichta, M.M., Heinzel, S., Ehlis, A.-C., Pauli, P., Fallgatter, A.J., 2007. Model-based analysis of rapid event-related functional near-infrared spectroscopy (NIRS) data: A parametric validation study. NeuroImage 35, 625–634. doi:10.1016/j.neuroimage.2006.11.028

Plummer, C., Harvey, A.S., Cook, M., 2008. EEG source localization in focal epilepsy: Where are we now? Epilepsia 49, 201–218. doi:10.1111/j.1528-1167.2007.01381.x

Pouliot, P., Tran, T.P.Y., Birca, V., Vannasing, P., Tremblay, J., Lassonde, M., Nguyen, D.K., 2014. Hemodynamic changes during posterior epilepsies: an EEG-fNIRS study. Epilepsy Res. 108, 883–890. doi:10.1016/j.eplepsyres.2014.03.007

Pouliot, P., Tremblay, J., Robert, M., Vannasing, P., Lepore, F., Lassonde, M., Sawan, M., Nguyen, D.K., Lesage, F., 2012. Nonlinear hemodynamic responses in human epilepsy: a multimodal analysis with fNIRS-EEG and fMRI-EEG. J. Neurosci. Methods 204, 326–340. doi:10.1016/j.jneumeth.2011.11.016

Prahl, S., 1998. Tabulated Molar Extinction Coefficient for Hemoglobin in Water [WWW Document]. URL http://omlc.org/spectra/hemoglobin/summary.html (accessed 4.10.16).

Proulx, S., Safi-Harb, M., Levan, P., An, D., Watanabe, S., Gotman, J., 2014. Increased sensitivity of fast BOLD fMRI with a subject-specific hemodynamic response function and application to epilepsy. NeuroImage 93 Pt 1, 59–73. doi:10.1016/j.neuroimage.2014.02.018

Quaresima, V., Bisconti, S., Ferrari, M., 2012. A brief review on the use of functional near-infrared spectroscopy (fNIRS) for language imaging studies in human newborns and adults. Brain Lang. 121, 79–89. doi:10.1016/j.bandl.2011.03.009

Rajapakse, J.C., Kruggel, F., Maisog, J.M., von Cramon, D.Y., 1998. Modeling hemodynamic response for analysis of functional MRI time-series. Hum. Brain Mapp. 6, 283–300.

Ramgopal, S., Thome-Souza, S., Jackson, M., Kadish, N.E., Sánchez Fernández, I., Klehm, J., Bosl, W., Reinsberger, C., Schachter, S., Loddenkemper, T., 2014. Seizure detection, seizure prediction, and closed-loop warning systems in epilepsy. Epilepsy Behav. 37, 291–307. doi:10.1016/j.yebeh.2014.06.023

Ramli, N., Rahmat, K., Lim, K.S., Tan, C.T., 2015. Neuroimaging in refractory epilepsy. Current practice and evolving trends. Eur. J. Radiol. 84, 1791–1800. doi:10.1016/j.ejrad.2015.03.024

Rathakrishnan, R., Moeller, F., Levan, P., Dubeau, F., Gotman, J., 2010. BOLD signal changes preceding negative responses in EEG-fMRI in patients with focal epilepsy. Epilepsia 51, 1837–1845. doi:10.1111/j.1528-1167.2010.02643.x

Rathore, C., Dickson, J.C., Teotónio, R., Ell, P., Duncan, J.S., 2014. The utility of 18F-fluorodeoxyglucose PET (FDG PET) in epilepsy surgery. Epilepsy Res. 108, 1306–1314. doi:10.1016/j.eplepsyres.2014.06.012

Ray, A., Bowyer, S.M., 2010. Clinical applications of magnetoencephalography in epilepsy. Ann. Indian Acad. Neurol. 13, 14–22. doi:10.4103/0972-2327.61271

Richter, W., Richter, M., 2003. The shape of the fMRI BOLD response in children and adults changes systematically with age. NeuroImage 20, 1122–1131. doi:10.1016/S1053-8119(03)00347-1

Rizki, E.E., Uga, M., Dan, I., Dan, H., Tsuzuki, D., Yokota, H., Oguro, K., Watanabe, E., 2015. Determination of epileptic focus side in mesial temporal lobe epilepsy using long-term noninvasive fNIRS/EEG monitoring for presurgical evaluation. Neurophotonics 2, 025003–025003. doi:10.1117/1.NPh.2.2.025003

Roche-Labarbe, N., Zaaimi, B., Berquin, P., Nehlig, A., Grebe, R., Wallois, F., 2008. NIRS-measured oxy- and deoxyhemoglobin changes associated with EEG spike-and-wave discharges in children. Epilepsia 49, 1871–1880. doi:10.1111/j.1528-1167.2008.01711.x

Rose, D.F., Fujiwara, H., Holland-Bouley, K., Greiner, H.M., Arthur, T., Mangano, F.T., 2013. Focal Peak Activities in Spread of Interictal-Ictal Discharges in Epilepsy with Beamformer MEG: Evidence for an Epileptic Network? Front. Neurol. 4, 56. doi:10.3389/fneur.2013.00056

Rosenow, F., Lüders, H., 2001. Presurgical evaluation of epilepsy. Brain 124, 1683–1700. doi:10.1093/brain/124.9.1683

Rotondi, F., Franceschetti, S., Avanzini, G., Panzica, F., 2016. Altered EEG resting-state effective connectivity in drug-naïve childhood absence epilepsy. Clin. Neurophysiol. 127, 1130–1137. doi:10.1016/j.clinph.2015.09.003

Rutily, B., Chevallier, L., 2006. Why is it so difficult to solve the radiative transfer equation? EAS Publ. Ser. 18, 1–23. doi:10.1051/eas:2006002

Rysz, A., Bidziński, J., Gołebiewski, M., Kroh, H., Bonicki, W., 1998. The value of structural neuroimaging in the selection of patients for epileptic surgery. Neurol. Neurochir. Pol. 32 Suppl 2, 217–225.

Ryvlin, P., Rheims, S., 2016. Predicting epilepsy surgery outcome. Curr. Opin. Neurol. 29, 182–188. doi:10.1097/WCO.0000000000000306

Saager, R.B., Telleri, N.L., Berger, A.J., 2011. Two-detector Corrected Near Infrared Spectroscopy (C-NIRS) detects hemodynamic activation responses more robustly than single-detector NIRS. NeuroImage 55, 1679–1685.

Sager, S., Asa, S., Uslu, L., Halac, M., 2011. Unilateral thalamic hypometabolism on FDG brain PET in patient with temporal lobe epilepsy. Indian J. Nucl. Med. IJNM Off. J. Soc. Nucl. Med. India 26, 94–95. doi:10.4103/0972-3919.90260

Saito, S., Yoshikawa, D., Nishihara, F., Morita, T., Kitani, Y., Amaya, T., Fujita, T., 1995. The cerebral hemodynamic response to electrically induced seizures in man. Brain Res. 673, 93–100.

Salek-Haddadi, A., Diehl, B., Hamandi, K., Merschhemke, M., Liston, A., Friston, K., Duncan, J.S., Fish, D.R., Lemieux, L., 2006. Hemodynamic correlates of epileptiform discharges: an EEG-fMRI study of 63 patients with focal epilepsy. Brain Res. 1088, 148–166. doi:10.1016/j.brainres.2006.02.098

Salinsky, M., Kanter, R., Dasheiff, R.M., 1987. Effectiveness of multiple EEGs in supporting the diagnosis of epilepsy: an operational curve. Epilepsia 28, 331–334.

Sargolzaei, S., Cabrerizo, M., Goryawala, M., Eddin, A.S., Adjouadi, M., 2015. Scalp EEG brain functional connectivity networks in pediatric epilepsy. Comput. Biol. Med. 56, 158–166. doi:10.1016/j.compbiomed.2014.10.018

Sarikaya, I., 2015. PET studies in epilepsy. Am. J. Nucl. Med. Mol. Imaging 5, 416–430.

Sato, Y., Fukuda, M., Oishi, M., Shirasawa, A., Fujii, Y., 2013. Ictal near-infrared spectroscopy and electrocorticography study of supplementary motor area seizures. J. Biomed. Opt. 18, 76022. doi:10.1117/1.JBO.18.7.076022

Savic, I., Altshuler, L., Baxter, L., Engel, J., 1997. Pattern of interictal hypometabolism in PET scans with fludeoxyglucose F 18 reflects prior seizure types in patients with mesial temporal lobe seizures. Arch. Neurol. 54, 129–136.

Sawan, M., Salam, M.T., Le Lan, J., Kassab, A., Gelinas, S., Vannasing, P., Lesage, F., Lassonde, M., Nguyen, D.K., 2013. Wireless recording systems: from noninvasive EEG-NIRS to invasive EEG devices. IEEE Trans. Biomed. Circuits Syst. 7, 186–195. doi:10.1109/TBCAS.2013.2255595

Schaeffer, J.D., Yennu, A.S., Gandy, K.C., Tian, F., Liu, H., Park, H., 2014. An fNIRS investigation of associative recognition in the prefrontal cortex with a rapid event-related design. J. Neurosci. Methods 235, 308–315. doi:10.1016/j.jneumeth.2014.07.011

Scholkmann, F., Spichtig, S., Muehlemann, T., Wolf, M., 2010. How to detect and reduce movement artifacts in near-infrared imaging using moving standard deviation and spline interpolation. Physiol. Meas. 31, 649–662. doi:10.1088/0967-3334/31/5/004

Schroeter, M.L., Bücheler, M.M., Müller, K., Uludağ, K., Obrig, H., Lohmann, G., Tittgemeyer, M., Villringer, A., von Cramon, D.Y., 2004. Towards a standard analysis for functional near-infrared imaging. NeuroImage 21, 283–290.

Schwartz, T.H., 2007. Neurovascular Coupling and Epilepsy: Hemodynamic Markers for Localizing and Predicting Seizure Onset. Epilepsy Curr. 7, 91–94. doi:10.1111/j.1535-7511.2007.00183.x

Selb, J., Boas, D.A., Chan, S.-T., Evans, K.C., Buckley, E.M., Carp, S.A., 2014. Sensitivity of near-infrared spectroscopy and diffuse correlation spectroscopy to brain hemodynamics: simulations and experimental findings during hypercapnia. Neurophotonics 1. doi:10.1117/1.NPh.1.1.015005

Seyal, M., 2014. Frontal hemodynamic changes precede EEG onset of temporal lobe seizures. Clin. Neurophysiol. 125, 442–448. doi:10.1016/j.clinph.2013.09.003

Sheehy, N., 1984. Electroencephalography: Basic Principles, Clinical Applications and Related Fields. J. Neurol. Neurosurg. Psychiatry 47, 654.

Shigeto, H., Morioka, T., Hisada, K., Nishio, S., Ishibashi, H., Kira, D.-I., Tobimatsu, S., Kato, M., 2002. Feasibility and limitations of magnetoencephalographic detection of epileptic discharges: Simultaneous recording of magnetic fields and electrocorticography. Neurol. Res. 24, 531–536. doi:10.1179/016164102101200492

Shuhaiber, H., Bolton, S., Alfonso, I., Dunoyer, C., Yaylali, I., 2004. Cerebral regional oxygen fluctuations and decline during clinically silent focal electroencephalographic seizures in a neonate. J. Child Neurol. 19, 539–540.

Sierra-Marcos, A., Maestro, I., Falcón, C., Donaire, A., Setoain, J., Aparicio, J., Rumià, J., Pintor, L., Boget, T., Carreño, M., Bargalló, N., 2013. Ictal EEG-fMRI in localization of

epileptogenic area in patients with refractory neocortical focal epilepsy. Epilepsia 54, 1688–1698. doi:10.1111/epi.12329

Singh, H., Cooper, R.J., Wai Lee, C., Dempsey, L., Edwards, A., Brigadoi, S., Airantzis, D., Everdell, N., Michell, A., Holder, D., Hebden, J.C., Austin, T., 2014. Mapping cortical haemodynamics during neonatal seizures using diffuse optical tomography: a case study. NeuroImage Clin. 5, 256–265. doi:10.1016/j.nicl.2014.06.012

Slone, E., Westwood, E., Dhaliwal, H., Federico, P., Dunn, J.F., 2012. Near-infrared spectroscopy shows preictal haemodynamic changes in temporal lobe epilepsy. Epileptic. Disord. 14, 371–378. doi:10.1684/epd.2012.0535

Smith, S., 2005. EEG in the diagnosis, classification, and management of patients with epilepsy. J. Neurol. Neurosurg. Psychiatry 76, ii2-ii7. doi:10.1136/jnnp.2005.069245

So, E.L., 2000. Integration of EEG, MRI, and SPECT in localizing the seizure focus for epilepsy surgery. Epilepsia 41 Suppl 3, S48-54.

Sokol, D.K., Markand, O.N., Daly, E.C., Luerssen, T.G., Malkoff, M.D., 2000. Near infrared spectroscopy (NIRS) distinguishes seizure types. Seizure 9, 323–327. doi:10.1053/seiz.2000.0406

Sokoloff, M.D., Plegue, M.A., Chervin, R.D., Barks, J.D.E., Shellhaas, R.A., 2015. Phenobarbital and neonatal seizures affect cerebral oxygen metabolism: a near-infrared spectroscopy study. Pediatr. Res. 78, 91–96. doi:10.1038/pr.2015.64

Spanaki, M.V., Spencer, S.S., Corsi, M., MacMullan, J., Seibyl, J., Zubal, I.G., 1999. Sensitivity and specificity of quantitative difference SPECT analysis in seizure localization. J. Nucl. Med. Off. Publ. Soc. Nucl. Med. 40, 730–736.

Spencer, S.S., 1994. The relative contributions of MRI, SPECT, and PET imaging in epilepsy. Epilepsia 35 Suppl 6, S72-89.

Spencer, S.S., Williamson, P.D., Bridgers, S.L., Mattson, R.H., Cicchetti, D.V., Spencer, D.D., 1985. Reliability and accuracy of localization by scalp ictal EEG. Neurology 35, 1567–1575.

Sperlágh, B., Vizi, S.E., 1996. Neuronal synthesis, storage and release of ATP. Semin. Neurosci. 8, 175–186. doi:10.1006/smns.1996.0023

Staley, K.J., Dudek, F.E., 2006. Interictal Spikes and Epileptogenesis. Epilepsy Curr. 6, 199–202. doi:10.1111/j.1535-7511.2006.00145.x

Stefan, H., 2010. Coregistered EEG/MEG for source localization in epilepsy. Epilepsia 51, 66–67. doi:10.1111/j.1528-1167.2009.02450.x

Stefan, H., Hummel, C., Scheler, G., Genow, A., Druschky, K., Tilz, C., Kaltenhäuser, M., Hopfengärtner, R., Buchfelder, M., Romstöck, J., 2003. Magnetic brain source imaging of focal epileptic activity: a synopsis of 455 cases. Brain J. Neurol. 126, 2396–2405. doi:10.1093/brain/awg239

Stefan, H., Lopes da Silva, F.H., 2013. Epileptic Neuronal Networks: Methods of Identification and Clinical Relevance. Front. Neurol. 4. doi:10.3389/fneur.2013.00008

Steinbrink, J., Wabnitz, H., Obrig, H., Villringer, A., Rinneberg, H., 2001. Determining changes in NIR absorption using a layered model of the human head. Phys. Med. Biol. 46, 879–896.

Steinhoff, B.J., Herrendorf, G., Kurth, C., 1996. Ictal near infrared spectroscopy in temporal lobe epilepsy: a pilot study. Seizure 5, 97–101.

Storti, S.F., Formaggio, E., Bertoldo, A., Manganotti, P., Fiaschi, A., Toffolo, G.M., 2013. Modelling hemodynamic response function in epilepsy. Clin. Neurophysiol. 124, 2108–2118. doi:10.1016/j.clinph.2013.05.024

Strangman, G., Franceschini, M.A., Boas, D.A., 2003. Factors affecting the accuracy of near-infrared spectroscopy concentration calculations for focal changes in oxygenation parameters. NeuroImage 18, 865–879.

Strangman, G.E., Li, Z., Zhang, Q., 2013. Depth Sensitivity and Source-Detector Separations for Near Infrared Spectroscopy Based on the Colin27 Brain Template. PLoS ONE 8, e66319. doi:10.1371/journal.pone.0066319

Suh, M., Ma, H., Zhao, M., Sharif, S., Schwartz, T.H., 2006. Neurovascular coupling and oximetry during epileptic events. Mol. Neurobiol. 33, 181–197. doi:10.1385/MN:33:3:181

Surin, A.M., Khiroug, S., Gorbacheva, L.R., Khodorov, B.I., Pinelis, V.G., Khiroug, L., 2012. Comparative analysis of cytosolic and mitochondrial ATP synthesis in embryonic and postnatal hippocampal neuronal cultures. Front. Mol. Neurosci. 5, 102. doi:10.3389/fnmol.2012.00102

Swartz, B.E., 1998. The advantages of digital over analog recording techniques. Electroencephalogr. Clin. Neurophysiol. 106, 113–117. doi:10.1016/S0013-4694(97)00113-2

Tak, S., Ye, J.C., 2014. Statistical analysis of fNIRS data: a comprehensive review. NeuroImage 85 Pt 1, 72–91. doi:10.1016/j.neuroimage.2013.06.016

Tanaka, N., Kamada, K., Takeuchi, F., 2004. Ictal magnetoencephalographic study in a patient with ring 20 syndrome. J. Neurol. Neurosurg. Psychiatry 75, 488–490.

Tao, J.X., Baldwin, M., Hawes-Ebersole, S., Ebersole, J.S., 2007. Cortical substrates of scalp EEG epileptiform discharges. J. Clin. Neurophysiol. Off. Publ. Am. Electroencephalogr. Soc. 24, 96–100. doi:10.1097/WNP.0b013e31803ecdaf

Téllez-Zenteno, J.F., Hernández Ronquillo, L., Moien-Afshari, F., Wiebe, S., 2010. Surgical outcomes in lesional and non-lesional epilepsy: a systematic review and meta-analysis. Epilepsy Res. 89, 310–318. doi:10.1016/j.eplepsyres.2010.02.007

Tellez-Zenteno, J.F., Pondal-Sordo, M., Matijevic, S., Wiebe, S., 2004. National and regional prevalence of self-reported epilepsy in Canada. Epilepsia 45, 1623–1629. doi:10.1111/j.0013-9580.2004.24904.x

Thivard, L., Adam, C., Hasboun, D., Clémenceau, S., Dezamis, E., Lehéricy, S., Dormont, D., Chiras, J., Baulac, M., Dupont, S., 2006. Interictal diffusion MRI in partial epilepsies explored with intracerebral electrodes. Brain J. Neurol. 129, 375–385. doi:10.1093/brain/awh709

Thornton, R., Laufs, H., Rodionov, R., Cannadathu, S., Carmichael, D.W., Vulliemoz, S., Salek-Haddadi, A., McEvoy, A.W., Smith, S.M., Lhatoo, S., Elwes, R.D.C., Guye, M., Walker,

M.C., Lemieux, L., Duncan, J.S., 2010a. EEG correlated functional MRI and postoperative outcome in focal epilepsy. J. Neurol. Neurosurg. Psychiatry 81, 922–927. doi:10.1136/jnnp.2009.196253

Thornton, R., Rodionov, R., Laufs, H., Vulliemoz, S., Vaudano, A., Carmichael, D., Cannadathu, S., Guye, M., McEvoy, A., Lhatoo, S., Bartolomei, F., Chauvel, P., Diehl, B., De Martino, F., Elwes, R.D.C., Walker, M.C., Duncan, J.S., Lemieux, L., 2010b. Imaging haemodynamic changes related to seizures: comparison of EEG-based general linear model, independent component analysis of fMRI and intracranial EEG. NeuroImage 53, 196–205. doi:10.1016/j.neuroimage.2010.05.064

Timmer, J., 2000. What can Be inferred from surrogate data testing? Phys. Rev. Lett. 85, 2647.

Tomasi, D., Ernst, T., Caparelli, E.C., Chang, L., 2006. Common deactivation patterns during working memory and visual attention tasks: An intra-subject fMRI study at 4 Tesla. Hum. Brain Mapp. 27, 694–705. doi:10.1002/hbm.20211

Toronov, V.Y., Zhang, X., Webb, A.G., 2007. A spatial and temporal comparison of hemodynamic signals measured using optical and functional magnetic resonance imaging during activation in the human primary visual cortex. NeuroImage 34, 1136–1148. doi:10.1016/j.neuroimage.2006.08.048

Tovar-Spinoza, Z.S., Ochi, A., Rutka, J.T., Go, C., Otsubo, H., 2008. The role of magnetoencephalography in epilepsy surgery. Neurosurg. Focus 25, E16. doi:10.3171/FOC/2008/25/9/E16

Uludag, K., 2010. To dip or not to dip: reconciling optical imaging and fMRI data. Proc. Natl. Acad. Sci. U. S. A. 107, E23; author reply E24. doi:10.1073/pnas.0914194107

Uludağ, K., Müller-Bierl, B., Uğurbil, K., 2009. An integrative model for neuronal activity-induced signal changes for gradient and spin echo functional imaging. NeuroImage 48, 150–165. doi:10.1016/j.neuroimage.2009.05.051

van Graan, L.A., Lemieux, L., Chaudhary, U.J., 2015. Methods and utility of EEG-fMRI in epilepsy. Quant. Imaging Med. Surg. 5, 300–312. doi:10.3978/j.issn.2223-4292.2015.02.04

van Houdt, P.J., de Munck, J.C., Leijten, F.S.S., Huiskamp, G.J.M., Colon, A.J., Boon, P.A.J.M., Ossenblok, P.P.W., 2013. EEG-fMRI correlation patterns in the presurgical evaluation of focal epilepsy: a comparison with electrocorticographic data and surgical outcome measures. NeuroImage 75, 238–248. doi:10.1016/j.neuroimage.2013.02.033

van Houdt, P.J., de Munck, J.C., Zijlmans, M., Huiskamp, G., Leijten, F.S.S., Boon, P.A.J.M., Ossenblok, P.P.W., 2010. Comparison of analytical strategies for EEG-correlated fMRI data in patients with epilepsy. Magn. Reson. Imaging 28, 1078–1086. doi:10.1016/j.mri.2010.03.022

van Mierlo, P., Papadopoulou, M., Carrette, E., Boon, P., Vandenberghe, S., Vonck, K., Marinazzo, D., 2014. Functional brain connectivity from EEG in epilepsy: Seizure prediction and epileptogenic focus localization. Prog. Neurobiol. 121, 19–35. doi:10.1016/j.pneurobio.2014.06.004

Van Paesschen, W., 2004. Ictal SPECT. Epilepsia 45 Suppl 4, 35–40. doi:10.1111/j.0013-9580.2004.04008.x

Vanzetta, I., Flynn, C., Ivanov, A.I., Bernard, C., Bénar, C.G., 2010. Investigation of linear coupling between single-event blood flow responses and interictal discharges in a model of experimental epilepsy. J. Neurophysiol. 103, 3139–3152. doi:10.1152/jn.01048.2009

Veldsman, M., Cumming, T., Brodtmann, A., 2015. Beyond BOLD: Optimizing functional imaging in stroke populations. Hum. Brain Mapp. 36, 1620–1636. doi:10.1002/hbm.22711

Villringer, A., Planck, J., Stodieck, S., Bötzel, K., Schleinkofer, L., Dirnagl, U., 1994. Noninvasive assessment of cerebral hemodynamics and tissue oxygenation during activation of brain cell function in human adults using near infrared spectroscopy. Adv. Exp. Med. Biol. 345, 559–565.

Vinette, S.A., Dunn, J.F., Slone, E., Federico, P., 2015. Artifact reduction in long-term monitoring of cerebral hemodynamics using near-infrared spectroscopy. Neurophotonics 2, 25004. doi:10.1117/1.NPh.2.2.025004

Virtanen, J., Noponen, T., Kotilahti, K., Virtanen, J., Ilmoniemi, R.J., 2011. Accelerometer-based method for correcting signal baseline changes caused by motion artifacts in medical near-infrared spectroscopy. J. Biomed. Opt. 16, 87005. doi:10.1117/1.3606576

Voges, N., Blanchard, S., Wendling, F., David, O., Benali, H., Papadopoulo, T., Clerc, M., Bénar, C., 2012. Modeling of the neurovascular coupling in epileptic discharges. Brain Topogr. 25, 136–156. doi:10.1007/s10548-011-0190-1

von Oertzen, T.J., Mormann, F., Urbach, H., Reichmann, K., Koenig, R., Clusmann, H., Biersack, H.J., Elger, C.E., 2011. Prospective use of subtraction ictal SPECT coregistered to MRI (SISCOM) in presurgical evaluation of epilepsy. Epilepsia 52, 2239–2248. doi:10.1111/j.1528-1167.2011.03219.x

Vulliemoz, S., Carmichael, D.W., Rosenkranz, K., Diehl, B., Rodionov, R., Walker, M.C., McEvoy, A.W., Lemieux, L., 2011. Simultaneous intracranial EEG and fMRI of interictal epileptic discharges in humans. NeuroImage 54, 182–190. doi:10.1016/j.neuroimage.2010.08.004

Vulliemoz, S., Thornton, R., Rodionov, R., Carmichael, D.W., Guye, M., Lhatoo, S., McEvoy, A.W., Spinelli, L., Michel, C.M., Duncan, J.S., Lemieux, L., 2009. The spatio-temporal mapping of epileptic networks: Combination of EEG–fMRI and EEG source imaging. NeuroImage 46, 834–843. doi:10.1016/j.neuroimage.2009.01.070

Wallois, F., Patil, A., Héberlé, C., Grebe, R., 2010. EEG-NIRS in epilepsy in children and neonates. Neurophysiol. Clin. Neurophysiol. 40, 281–292. doi:10.1016/j.neucli.2010.08.004

Wallois, F., Patil, A., Kongolo, G., Goudjil, S., Grebe, R., 2009. Haemodynamic changes during seizure-like activity in a neonate: a simultaneous AC EEG-SPIR and high-resolution DC EEG recording. Clin. Neurophysiol. 39, 217–227. doi:10.1016/j.neucli.2009.08.001

Wang, L.V., Wu, H., 2007. Biomedical Optics: Principles and Imaging. John Wiley & Sons.

Ward, B.D., 2006. Deconvolution analysis of fMRI time series data.

Watanabe, E., Maki, A., Kawaguchi, F., Yamashita, Y., Koizumi, H., Mayanagi, Y., 2000. Noninvasive cerebral blood volume measurement during seizures using multichannel near infrared spectroscopic topography. J. Biomed. Opt. 5, 287–290. doi:10.1117/1.429998

Watanabe, E., Nagahori, Y., Mayanagi, Y., 2002. Focus diagnosis of epilepsy using near-infrared spectroscopy. Epilepsia 43, 50–55.

Watanabe, S., An, D., Safi-Harb, M., Dubeau, F., Gotman, J., 2014. Hemodynamic Response Function (HRF) in Epilepsy Patients with Hippocampal Sclerosis and Focal Cortical Dysplasia. Brain Topogr. 27, 613–619. doi:10.1007/s10548-014-0362-x

Weil, S., Noachtar, S., Arnold, S., Yousry, T.A., Winkler, P.A., Tatsch, K., 2001. Ictal ECD-SPECT differentiates between temporal and extratemporal epilepsy: confirmation by excellent postoperative seizure control. Nucl. Med. Commun. 22, 233–237.

Wendling, F., Bartolomei, F., Senhadji, L., 2009. Spatial analysis of intracerebral electroencephalographic signals in the time and frequency domain: identification of epileptogenic networks in partial epilepsy. Philos. Transact. A Math. Phys. Eng. Sci. 367, 297–316. doi:10.1098/rsta.2008.0220

White, B.R., Culver, J.P., 2010. Quantitative evaluation of high-density diffuse optical tomography: in vivo resolution and mapping performance. J. Biomed. Opt. 15, 26006-26006–14. doi:10.1117/1.3368999

Wiebe, S., Bellhouse, D.R., Fallahay, C., Eliasziw, M., 1999. Burden of epilepsy: the Ontario Health Survey. Can. J. Neurol. Sci. J. Can. Sci. Neurol. 26, 263–270.

Willmann, O., Wennberg, R., May, T., Woermann, F.G., Pohlmann-Eden, B., 2007. The contribution of 18F-FDG PET in preoperative epilepsy surgery evaluation for patients with temporal lobe epilepsy: A meta-analysis. Seizure 16, 509–520. doi:10.1016/j.seizure.2007.04.001

Won, H.J., Chang, K.H., Cheon, J.E., Kim, H.D., Lee, D.S., Han, M.H., Kim, I.O., Lee, S.K., Chung, C.K., 1999. Comparison of MR imaging with PET and ictal SPECT in 118 patients with intractable epilepsy. AJNR Am. J. Neuroradiol. 20, 593–599.

Woolrich, M.W., Jenkinson, M., Brady, J.M., Smith, S.M., 2004. Fully Bayesian spatio-temporal modeling of FMRI data. IEEE Trans. Med. Imaging 23, 213–231. doi:10.1109/TMI.2003.823065

World Health Organization, 2016. Fact Sheet - Epilepsy.

Worsley, K.J., Friston, K.J., 1995. Analysis of fMRI time-series revisited--again. NeuroImage 2, 173–181. doi:10.1006/nimg.1995.1023

Worsley, K.J., Liao, C.H., Aston, J., Petre, V., Duncan, G.H., Morales, F., Evans, A.C., 2002. A general statistical analysis for fMRI data. NeuroImage 15, 1–15. doi:10.1006/nimg.2001.0933

Wu, J.Y., Sutherling, W.W., Koh, S., Salamon, N., Jonas, R., Yudovin, S., Sankar, R., Shields, W.D., Mathern, G.W., 2006. Magnetic source imaging localizes epileptogenic zone in children with tuberous sclerosis complex. Neurology 66, 1270–1272. doi:10.1212/01.wnl.0000208412.59491.9b

Yacoub, E., Hu, X., 2001. Detection of the early decrease in fMRI signal in the motor area. Magn. Reson. Med. 45, 184–190.

Yang, T., Hakimian, S., Schwartz, T.H., 2014. Intraoperative ElectroCorticoGraphy (ECog): indications, techniques, and utility in epilepsy surgery. Epileptic Disord. Int. Epilepsy J. Videotape 16, 271–279. doi:10.1684/epd.2014.0675

Ye, J.C., Tak, S., Jang, K.E., Jung, J., Jang, J., 2009. NIRS-SPM: Statistical parametric mapping for near-infrared spectroscopy. NeuroImage 44, 428–447. doi:10.1016/j.neuroimage.2008.08.036

Yücel, M.A., Selb, J., Boas, D.A., Cash, S.S., Cooper, R.J., 2014a. Reducing motion artifacts for long-term clinical NIRS monitoring using collodion-fixed prism-based optical fibers. NeuroImage, Celebrating 20 Years of Functional Near Infrared Spectroscopy (fNIRS) 85, Part 1, 192–201. doi:10.1016/j.neuroimage.2013.06.054

Yücel, M.A., Selb, J., Cooper, R.J., Boas, D.A., 2014b. Targeted principle component analysis: A new motion artifact correction approach for near-infrared spectroscopy. J. Innov. Opt. Health Sci. 7, 1350066. doi:10.1142/S1793545813500661

Zeff, B.W., White, B.R., Dehghani, H., Schlaggar, B.L., Culver, J.P., 2007. Retinotopic mapping of adult human visual cortex with high-density diffuse optical tomography. Proc. Natl. Acad. Sci. 104, 12169–12174. doi:10.1073/pnas.0611266104

Zhang, J., Liu, W., Chen, H., Xia, H., Zhou, Z., Mei, S., Liu, Q., Li, Y., 2013. Multimodal neuroimaging in presurgical evaluation of drug-resistant epilepsy. NeuroImage Clin. 4, 35–44. doi:10.1016/j.nicl.2013.10.017

Zhang, N., Zhu, X.-H., Chen, W., 2008. Investigating the source of BOLD nonlinearity in human visual cortex in response to paired visual stimuli. NeuroImage 43, 204–212. doi:10.1016/j.neuroimage.2008.06.033

Zhang, Q., Brown, E.N., Strangman, G.E., 2007. Adaptive filtering for global interference cancellation and real-time recovery of evoked brain activity: A Monte Carlo simulation study. J. Biomed. Opt. 12.

Zhang, Q., Strangman, G.E., Ganis, G., 2009. Adaptive filtering to reduce global interference in non-invasive NIRS measures of brain activation: How well and when does it work? NeuroImage 45, 788–794.

Zhang, T., Li, F., Gonzalez, M.Z., Maresh, E.L., Coan, J.A., 2014. A semi-parametric nonlinear model for event-related fMRI. NeuroImage 97, 178–187. doi:10.1016/j.neuroimage.2014.04.017

Zhao, M., Suh, M., Ma, H., Perry, C., Geneslaw, A., Schwartz, T.H., 2007. Focal increases in perfusion and decreases in hemoglobin oxygenation precede seizure onset in spontaneous human epilepsy. Epilepsia 48, 2059–2067. doi:10.1111/j.1528-1167.2007.01229.x

Zijlmans, M., Jacobs, J., Kahn, Y.U., Zelmann, R., Dubeau, F., Gotman, J., 2011. Ictal and interictal high frequency oscillations in patients with focal epilepsy. Clin. Neurophysiol. Off. J. Int. Fed. Clin. Neurophysiol. 122, 664–671. doi:10.1016/j.clinph.2010.09.021

Zumsteg, D., Wieser, H.G., 2000. Presurgical evaluation: current role of invasive EEG. Epilepsia 41 Suppl 3, S55-60.